FEMTOSECOND CELLULAR TRANSFECTION USING NOVEL LASER BEAM GEOMETRIES

Xanthi Tsampoula

A Thesis Submitted for the Degree of PhD
at the
University of St Andrews

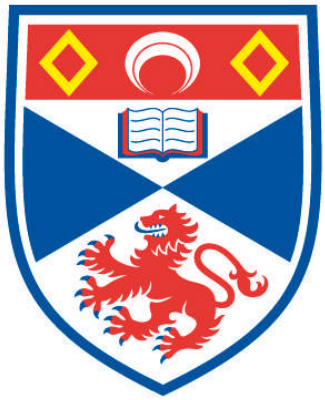

2009

Femtosecond cellular transfection using novel laser beam geometries

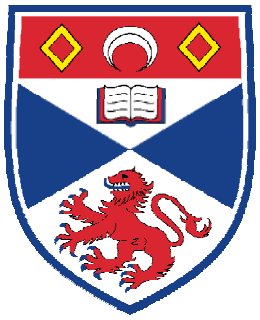

University
of
St Andrews

A thesis submitted to the University of St Andrews

in application for the degree of

Doctor of Philosophy

by

Xanthi Tsampoula

30 June 2009

I, Xanthi Tsampoula, hereby certify that this thesis, which is approximately 45,000 words in length, has been written by me, that it is the record of work carried out by me and that it has not been submitted in any previous application for a higher degree.

I was admitted as a research student in November 2005 and as a candidate the degree of Doctor of Philosophy in June 2006; the higher study for which this a record was carried out in the University of St Andrews between 2005 and 2009.

date . . . . . signature of candidate . . . . . .

I hereby certify that the candidate has fulfilled the conditions of the Resolution and Regulations appropriate for the degree of Doctor of Philosophy in the University St Andrews and that the candidate is qualified to submit this thesis in application for that degree.

date . . . . . signature of supervisor . . . . . .

In submitting this thesis to the University of St Andrews we understand that we are giving permission for it to be made available for use in accordance with the regulations of the University Library for the time being in force, subject to any copyright vested in the work not being affected thereby. We also understand that the title and abstract will be published, and that a copy of the work may be made and supplied to any bona fide library or research worker, that my thesis will be electronically accessible for personal or research use unless exempt by award of an embargo as requested below, and that the library has the right to migrate my thesis into new electronic forms as required to ensure continued access to the thesis. We have obtained any third-party copyright permissions that may be required in order to allow such access and migration, or have requested the

appropriate embargo below.

The following is an agreed request by candidate and supervisor regarding the electronic publication of this thesis:

Access to Printed copy and electronic publication of thesis through the University of St Andrews.

Access to all or part of printed copy but embargo of all or part of electronic publication of thesis for a period of … years (maximum five) on the following ground:

publication would be commercially damaging to the researcher, or to the supervisor, or the University;

publication would preclude future publication;

publication would be in breach of law or ethics

Embargo on all or part of printed copy and electronic copy for the same fixed period of … years (maximum five) on the following ground:

publication would be commercially damaging to the researcher, or to the supervisor, or the University;

publication would preclude future publication;

publication would be in breach of law or ethics

Permanent embargo of all or part of print copy and electronic copies of thesis (permission will be granted only in highly exceptional circumstances).

[Where part of my thesis is embargoed, please specify the part and the reasons. Evidence for a request for an embargo must be included with the submission of the draft copy of

the thesis].

Date . . . . . Signature of candidate……..... Signature of supervisor.....……...

Στην Κατερίνα και τον Βαγγέλη

When you set out on your journey to Ithaca,
pray that the road is long,
full of adventure, full of knowledge.
The Lestrygonians and the Cyclopes,
the angry Poseidon – do not fear them:
You will never find such as these on your path
if your thoughts remain lofty, if a fine
emotion touches your spirit and your body.
The Lestrygonians and the Cyclops,
the fierce Poseidon you will never encounter,
if you do not carry them within your soul,
if your heart does not set them up before you.

From Ithaca, Constantine Cavafy (1863-1933)
Translated by Rae Dalven

Abstract

In this thesis, femtosecond (fs) cellular transfection of Chinese Hamster Ovary (CHO) cells was performed using a tightly focused Gaussian beam. The beam focus was positioned on the cell membrane and three laser doses, each of 40 ms duration, were delivered allowing for the formation of a highly localized pore on the cell membrane. The membrane pore, induced as a result of a multiphoton process known as photoporation, permitted the surrounding DNA to diffuse into the cell cytoplasm. 48 hours after laser irradiation, the viable photoporated cells expressed a red fluorescent protein. The topography of a photoporated cell, targeted with tightly focused fs pulses, was also monitored as a function of the input power using Atomic Force Microscopy. Following this, I generated and implemented a “non-diffracting” quasi-Bessel beam (BB) by means of a conical shaped lens, the axicon, which successfully provided an alternative route for photoporation to the highly divergent Gaussian beam. A comparison was given between the two beam approaches for photoporation. The “non-diffracting” character of the BB resulted in the first successful attempt towards automating optical transfection. This was achieved by using an axicon and a spatial light modulator (SLM) to provide phase modulation on the annular spatial spectrum field of the BB. This approach provided control over the lateral and axial position of the beam with respect to the cell membrane, allowing for point and click photoporation. Successful photoporation of CHO cells was also demonstrated using for the first time an axicon tipped optical fibre. The applicability prospects of this method are significant, ranging from potential endoscopic embodiments of the technique to advanced studies of tissue properties *in vitro* and *in vivo*.

Acknowledgements

Firstly, I would like to sincerely thank my supervisor Kishan Dholakia for the wonderful opportunity he gave me to become part of his team, for his endless support, enthusiasm and encouragement during the good and the challenging times of my PhD these past three and half years, as well as his tireless explanations and discussions on various physics topics. His patience, determination and kindness inspired me to go on when things just wouldn't work (cells wouldn't go red). I very much appreciated all the hours he spent reading through my thesis and I very much thank him for his guidance, mentoring and for teaching me how to be a researcher. Kishan, it has been a pleasure and a privilege working with you.

I would also like to equally thank Frank Gunn-Moore, for all of his encouragement and support, for his guidance with every aspect of the biology and for his time and patience with proof reading my thesis. In addition, many thanks should go to Tom Brown, for his very helpful feedback throughout my PhD, for always finding time to answer my physics questions and for going through my thesis. Special thanks go to Pascal for all his help, guidance with optics, labwork, fire alarms and coffees, also to Vene for been a great lab partner and all her determination, help and support with the Bessel beam project. Many thanks to Dave, Lynn and Peter for they were the first to show me around Kishan's labs, for their enthusiasm, big smiles and nice chats and Dave in particular for teaching me how to look after cells.

Many many thanks go especially to Thomas Cizmar for being so wonderful and willing to help out with everything, even when there was clearly no time to do so, for teaching

me so many things about Bessel beams, for his endless enthusiasm and help in the lab, with SLMs, computers, for providing the theory to our papers. Many thanks also go to Paul Prentice for his endless patience with the AFM project and for tirelessly transferring the zapped cells to Dundee for scans. Many thanks also to the WSquad guys, Iain, Klaus, Alex and Chris for their kind help with the autocorrelation measurements. Special thanks go to Igor Pastirk for his overseas support, enthusiasm and endless patience over the phone and emails for troubleshooting the pulse shaper. I am more than grateful to Rob for all that he has been and done for me throughout my PhD, for teaching me how to make spin and bake colloidal coverslips in the cleanroom, troubleshooting my computers, all the hours he spent hearing me practicing talks and for proof reading my thesis.

Ένα απέραντο ευχαριστώ πηγαίνει στους γονείς μου για όλη τους την αγάπη και υποστήριξη που μου δείξανε σε όλη την διάρκεια του master και του διδακτορικού μου, και που χωρίς εκείνους απλώς δεν θα είχα φτάσει ως εδώ.

Table of contents

.

Abbreviations

AFM	Atomic Force Microscopy
BB	Bessel beam
BBO	β-Barium Borate
Calcein AM	Calcein Acetoxymethylester
CCD	Charged Coupled Camera
CHO	Chinese Hamster Ovary
CW	Continuous Wave
DAPI	4’, 6-diamidino-2-phenylindole
DEAE-Dextran	Diethylaminoethyl-Dextran
DNA	Deoxyribonucleic Acid
Ds-Red	Discodeum Red
fs	Femtosecond
FT	Fourier Transform
FWHM	Full Width at Half Maximum
GFP	Green Fluorescent Protein
GVD	Group Velocity Dispersion
IFT	Inverse Fourier Transform
KDP	Potassium Dihydrogen Phosphate
MIIPS	Multiphoton Intrapulse Interference Phase Scan
ML	Mode-Locked
mRNA	Messenger RNA

NA	Numerical Aperture
ND	Neutral Density
NIR	Near-Infrared
ns	Nanosecond
PB	Propidium Bromide
PBS	Polarizing Beam Splitter
PI	Propidium Iodine
ps	Picosecond
rRNA	Ribosomal RNA
RNA	Ribonucleic Acid
SEM	Scanning Electron Microscope
SHG	Second Harmonic Generation
SLM	Spatial light modulator
SPM	Self Phase Modulation
TL	Transform Limited
TOD	Third Order Dispersion
tRNA	Tranfer RNA
UV	Ultra-Violet
USB	Universal Serial Bus
3D	3 Dimensions

Chapter 1
Introduction

1.1 Preface

The advent of the first laser by Theodore Maiman came in 1960 [1]. This first monochromatic and highly directional light source, defined the beginning of a new era of technological breakthroughs one of which is known to be Photonics. Photonics is the science which detects, counts and processes photons, investigates the properties of light and also how the latter can be utilised for the development and engineering of photonic devices such as lasers, photodetectors and optical fibres. It is closely associated to the fields of optics and electronics, which in conjunction with photonics have underpinned revolutions in all aspects of our lives, starting from home entertainment, to fibre optic telecommunications leading most recently to advances in cancer diagnosis and treatment.

Biophotonics lies in the interface of life and physical sciences. It is a rapidly developing interdisciplinary field that exploits the expertise of scientists from disciplines as diverse as medicine, biology, physics, chemistry, pharmacology, and engineering. The development of state of the art optical microscopes and laser sources, have contributed a great deal to the understanding of the working mechanisms of life in a cellular and subcellular level.

One of the most promising and rapidly developing research areas of Biophotonics is laser

cell nanosurgery and more specifically laser assisted cell transfection which will be the topic of discussion in this thesis. Cellular transfection is the process of transiently or permanently altering the genetic code of a cell by introducing nucleic acids, such as DNA or RNA into a cell or therapeutic agents in the context of drug delivery and therapy. Under normal circumstances, the lipid nature of the cell membrane acts as an impermeable barrier to the passage of most water-soluble molecules. Thus, the selective introduction of therapeutic agents to the interior of dysfunctional or diseased cells is a challenging issue. Approaches for transient membrane disruption include physical injection into individual cells using glass micropipettes, membrane fusion of loaded liposomes [2], ballistic introduction of coated gold nanospheres (gene gun) [3], local permeabilization of cells via the application of pulsed electric fields [4], and local permeabilization of cells via the application of diagnostic ultrasound (sonoporation) [5]. The invasive and toxic character of some of these methods has introduced a great deal of complexity and generated unresolved issues concerning the cell viability and DNA delivery efficiency.

Laser-assisted transfection is considered to be the non-invasive and sterile alternative to these techniques, offering a high degree of selectivity. The laser-assisted approach could also be combined with other optical technologies, such as multiphoton and confocal microscopy, optical tweezers and potentially microfluidics, offering the possibility of complex biophysics experiments within one instrument, the Biophotonics workstation. Laser assisted cellular transfection is a very promising technique that inaugurates a new era in genetics research for the study and understanding of many human neurodegenerative diseases and has the potential to shine light to their treatment.

The increasingly complex nature of human diseases and their detrimental consequences to people's quality of life makes the merging of disciplines an indispensable need. The good collaboration and communication, as well as the productive exchange of ideas and knowledge between scientists of different backgrounds becomes the new challenge that needs to be met if we are aiming to succeed in such an ambitious interdisciplinary action.

1.2 Synopsis of thesis

This thesis consists of seven chapters. As described already, Chapter one provides a short introduction in the interdisciplinary field of Biophotonics and the importance of collective action and cooperation between disciplines. In Chapter two, I give a brief description of the cell structure and the mechanisms of transport of molecules across the lipid membrane bilayer. The importance of introducing fluorescent proteins as opposed to fluorescent stains for performing cellular transfection is also explained. The chapter proceeds with a short description of the basic concepts in genetics such as chromosomes, the genome, and genetic modification of cells and how these concepts relate to cellular transfection. I move on with a short review on well established transfection techniques to date, followed by a detailed discussion on laser-assisted cellular transfection. A clear emphasis is placed on fs cellular transfection and the underlined physical mechanisms of the phenomenon.

Chapters three to seven, detail the experimental work conducted in the laboratory and the analysis on the theoretical physical concepts associated with each experiment.

Specifically, chapter three begins with an introduction on Gaussian beams, followed by a detailed description of the experimental work entailing photoporation and optical transfection of CHO cells using a tightly focused Gaussian beam. During photoporation, the cells, in the presence of plasmid DNA, are exposed to three laser doses resulting in membrane perforation at the irradiation site. Upon successful membrane perforation, the cells take up the plasmid DNA and express the encoded DS-Red fluorescent protein. The topography of the photoporated cells is investigated by means of AFM. Specifically, the size and shape of the laser induced pore is obtained as a function of incident laser power.

Chapter four details fs optical transfection of CHO cells by means of a “non-spreading” BB. The chapter begins with an introduction to BBs and a description of their most important propagation properties. The experimental part of this work describes the generation of a BB using a conical lens (the axicon) that propagates over long distances without significant spreading. The transfection efficiency of CHO cells upon BB irradiation was monitored as a function of the axial position of the cell membrane along the propagation direction of the beam. The findings of both Gaussian and Bessel beam transfection experiments are compared in order to highlight the merits of a “non-diffracting” light beam for transfection studies. The last part of this chapter describes the steps towards automating the optical transfection process by means of a BB and an SLM. A BB was generated using an axicon and its annular spatial spectrum field (far field) was phase modulated using an SLM. This arrangement provided 3D control (lateral and axial) in the positioning of the beam with respect to the cell sample, providing almost full automation of the transfection process.

Chapter five details laser assisted transfection of CHO cells using the novel approach of an optical fibre, the axicon tipped fibre, for cell targeting during photoporation. Contrary to the current free space methodologies for optical transfection, the use of an optical fibre offers a simpler and versatile alternative. The axicon tipped fibre was fabricated by means of chemically etching a standard single mode fibre which resulted in a conical shape core facet. By controlling the apex angle of the core tip during fabrication, the achievable working distance (safety margin) between the fibre tip and the irradiated cells can be controlled. This allows for safe cell photoporation, minimising the risk of accidental fibre contact with the cells that could compromise the cell membrane or lead to irreversible cell damage.

Chapter six is a chapter which provides preliminary results on my ongoing work concerning dispersion measurement and pre-compensation in microscope systems and the axicon tipped optical fibre. Dispersion management in ultra-short pulses is accomplished by means of an SLM based pulse shaper which provides adaptive spectral characterization of ultra-short pulses and automatic pre-compensation by means of MIIPS. Spectrally shaped pulses, of 12 fs duration have been obtained at the objective focus in a Gaussian photoporation setup and pulses as short as 16 fs at the axicon tipped fibre output. This work paves the way for photoporation studies using spectrally shaped, dispersion free ultra-short pulses that may allow for minimally invasive membrane perforation of unprecedented precision and accuracy.

Finally, chapter seven provides a summary of what has been presented and discussed in this thesis, highlighting the most important aspects of my work and how it can influence

future experimental work in the field. The last part of the conclusion chapter summarizes my publication record, conference presentations, distinctions through this work and the publicity this work has brought.

References

[1] T.H. Maiman, "*Stimulated Optical Radiation in Ruby,"* Nature **187**(4736), p. 493, 1960.

[2] P.L. Felgner, et al., "*Lipofection: a highly efficient, lipid-mediated DNA-transfection procedure,"* Proceedings of the national academy of sciences of the United States of America **84**(21), p. 7413, 1987.

[3] M. Voiland and L. McCandless, "*Development of the gene gun at Cornell*" Tutorial notes, Cornell University.

[4] E. Lee, et al., "*Microfluidic electroporation of robust 10-μm vesicles for manipulation of picoliter volumes,"* Journal of Biochemistry **69**(1), p. 117, 2006.

[5] P. Prentice, et al., "*Membrane disruption by optically controlled microbubble cavitation,"* Nature Physics **1**(2), p. 107, 2005.

Chapter 2

The biological and physical processes of cellular transfection

Introduction

In this chapter, I present a brief synopsis of the cell structure with an emphasis on the cell membrane and the mechanisms of transport of molecules across the plasma membrane. A brief discussion on fluorescent dyes and proteins is given with particular emphasis on the significance of successfully introducing nucleic acids encoding for fluorescent proteins within cells as opposed to only fluorescent dyes. A short reference on the cell genome and the mechanisms governing protein expression within a cell is also provided. Following this, an overview of the most widely used transfection techniques such as microinjection, electroporation, lipid and viral mediated chemical transfection is presented followed by a summary of optical transfection using various laser sources and pulse durations. Particular emphasis is given on fs optical transfection and the physical mechanisms that administer the process of photoporation and optical transfection cells are detailed and explained.

2.1 Elements of Biology

2.1.1 Overview of the cell structure

The cell is the basic structural and functional entity of every living system. It is a self-

governed and self-preserved unit, hence is able to perform a variety of functions that allow it to replicate through cell-division, communicate with the surrounding environment and respond to external stimuli.

The eukaryotic cell, the type of cells found in multicellular systems, e.g. higher animals and plants, exhibit three well defined structural blocks: the plasma membrane, the cytoplasm and the nucleus. Figure 1 shows the structure of an eukaryotic cell. The cellular membrane plays a vital role in the cell structure, as it forms the boundary that separates the cell from its surrounding [1].

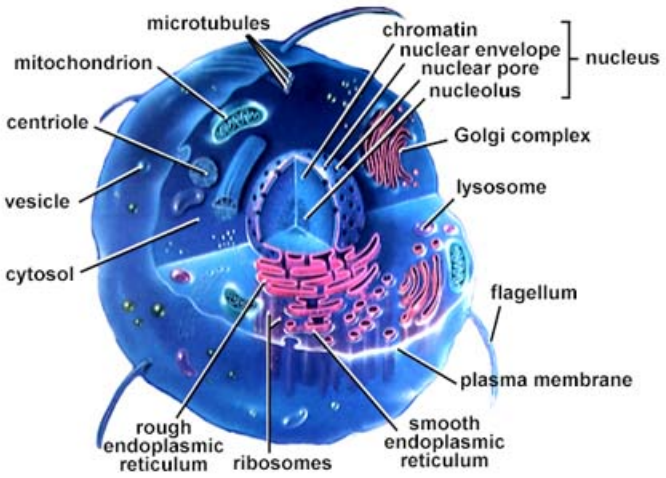

Figure 1: A model of a typical eukaryotic cell showing its constituent main building blocks; the membrane, the cytoplasm and the nucleus. The cytoplasmic organelles are also indicated [2].

The cell membrane consists of a bilayer of lipid molecules, the most important of which are called phospholipids and cholesterol molecules. Each of these lipids has a hydrophilic head and two hydrophobic tails. The phospholipids align themselves so that their tails are facing each other forming a well defined hydrophobic layer and are surrounded by the hydrophilic heads on the inner and outer surfaces of the membrane. In addition to the

lipids, the membrane consists of other important biomolecules that are interspersed in the lipid bilayer, such as membrane proteins [3]. Membrane proteins account for almost 50% of the entire membrane constituents. Figure 2 shows the main constituents of the cellular membrane. Depending on their functions and role in the membrane, proteins may be located on the surface of the membrane in the form of receptor and identification proteins or being embedded in the lipid bilayer.

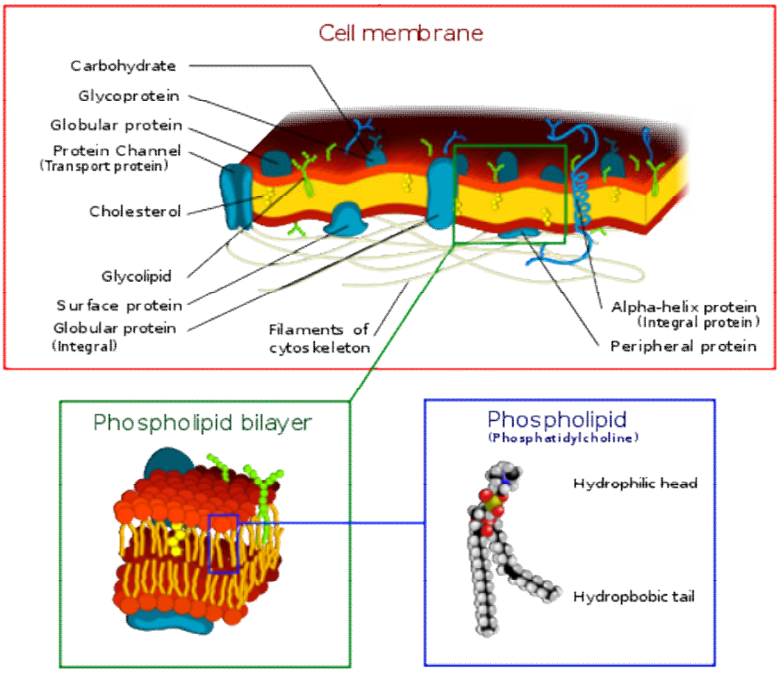

Figure 2: The cell membrane consists of a lipid bilayer in which the lipid molecules, particularly phospholipids, move along the membrane in a fluid fashion with the membrane proteins dispersed within it. Other membrane components are cholesterol molecules and carbohydrates [4].

The latter can serve as channel or transport proteins for the transmembrane transportation of ions and water solutes in and out of the cell. Surface proteins play important role in the cellular activities such as cell signaling, cell-to-cell contact and surface recognition.

The second main structural block of an eukaryotic cell is the cytoplasm. The cytoplasm is a dynamic structure that envelopes all the intra-cellular compartments called organelles. It is a liquid compartment, also called the cytosol that is made of water, salts, ions, proteins and catalysts that promote various reactions. A high degree of organization is present inside the cytoplasm due to the cytoskeleton. The cytoskeleton is the scaffolding of the cell, consisting of arrays of protein filaments that form networks inside the cytoplasm thus controlling the location of the various organelles and creating communication paths between them [1]. The organelles play the role of the organs in an organism and each one of them performs a specialized task inside the cell. Some of the other important organelles are the mitochondria, lysosomes, Golgi apparatus, endoplasmic reticulum, and ribosomes.

The third main structural compartment of the cell is the nucleus [1]. It is the largest cellular organelle with diameter that varies between 11 to 22 μm in mammalian cells. The nucleus has a similar structure to the cell itself in the sense that it possesses a nuclear membrane and a nucleoplasm. The nuclear envelope consists of two porous, outer and inner lipid bilayer membranes that separate the cytoplasm from the nuclear environment. The pores of the nuclear envelope consist of a number of proteins that selectively allow the passage of molecules in and out of the nucleus. The cell's genome is located in the nucleoplasm in the form of multiple DNA molecules that congregate into structures named chromosomes. The cell genome, how cells decode it, and how it can be modified through the transfection process are the focus of a following subsection.

2.1.2 Transport mechanisms of biomolecules across the cellular membrane

The membrane forms a protective, semi permeable layer around the cell that will selectively allow the passage of substances in and out of the cell. Due to the structural order of the lipid bilayer, the inner part of the membrane has a hydrophobic (non polar) nature therefore the membrane will be impermeable to the majority of the water soluble molecules and in general to polar i.e. charged substances. Figure 3 shows the lipid bilayer of the cellular membrane consisting of a hydrophilic (polar) and a hydrophobic region (non polar) with the membrane proteins dispersed within it.

Despite the fact that hydrophilic substances are hindered from spontaneously crossing the cell membrane, there is still a need for the cell to transport certain molecules or ions across its membrane, in the form of waste molecules, nutrients or regulate the concentration of ions inside the cytoplasm. The mechanisms involved in the transmembrane transport of various substances may have a passive or active nature. Some of the smallest, non polar materials such as oxygen, carbon dioxide and some ions are able to spontaneously diffuse from an area of higher concentration to an area of lower concentration, travelling down a concentration gradient. The cell does not need to utilize any energy for this transport.

Other molecules may traverse the cellular membrane by means of facilitated diffusion, which relies on membrane proteins acting as channels that regulate this transport.

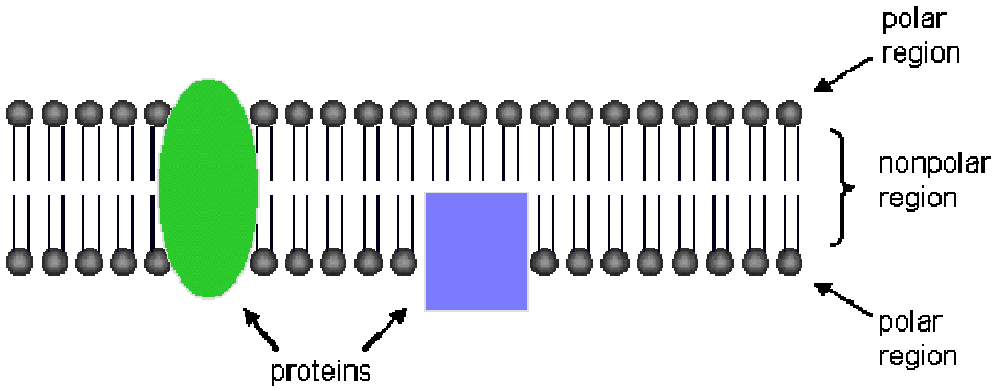

Figure 3: The lipid bilayer of the cellular membrane. The membrane acts as a semipermeable layer which allows selectively the passage of molecules in and out of the cell. Due to the hydrophobic (non polar) nature of the inner membrane layer, polar molecules such as some ions, nucleic acids and in general water soluble substances are prohibited from passing through [5].

This type of transport has a passive nature as the molecules or ions move down a concentration gradient without any energy expenditure. In the case of the transport of substances against a concentration gradient, the movement is enabled by carrier proteins. These proteins may possess moving parts that actively carry and transport biomaterial against its concentration gradient. Such movement is not energetically favored by the cell therefore the consumption of energy is required. Figure 4(a) shows the passive transport of particles by means of facilitated diffusion and 4(b) shows the action of carrier proteins that actively pump material and transport it against a concentration gradient.

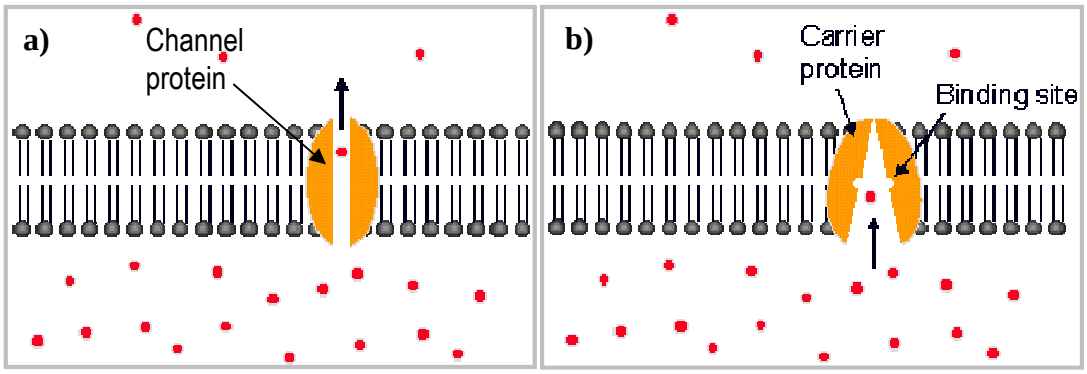

Figure 4: (a) Facilitated diffusion by means of channel proteins. (b) Carrier protein mediated transport of molecules from an area of lower to higher concentration gradient. This is the nature of endocytosis during which pump carrier proteins engulf molecules from the external cellular environment and transport them across the membrane towards the cytoplasm. Exocytosis is the same process but carried out in the opposite direction [5].

2.1.3 Transmembrane transport of substances by means of transfection

In addition to the transport of particles, ions and biomolecules across the lipid membrane which naturally takes place in cells, the selective introduction of exogenous or artificial material into cells is also of great interest. By means of cellular transfection, the selective internalization of dyes and nucleic acids into cells has been made possible. Most of the transfection methods rely on the creation of a pore or a number of pores on the cellular membrane that will form a pathway for these substances to diffuse into the cell interior. Most of these substances are charged, large in size and membrane impermeable, therefore a number of techniques have been employed by scientists in order to force their passage through the lipid membrane. Such techniques may involve carrier vesicles such as liposomes or viruses that encapsulate and transport the dye or gene of interest through the

membrane, electrical pulses that permeabilize the cell membrane, or the use of light to transiently perforate the lipid membrane. Such methodologies will be detailed later on in this chapter.

A variety of biological stains have been used to label transparent structures within the cell's cytoplasm such as proteins, nucleic acids, various cytoplasmic organelles or the cell nucleus. By staining an intracellular structure, the shape, size and its position within the cell can be readily studied. The ability to introduce dyes within cells is also applicable in flow cytometry where stained cells are counted or separated as well as in cell viability assays. Not all biological stains will interact with the cell in the same way therefore different stains will target different cellular compartments. Some of these dyes are membrane permeable and will naturally diffuse through the membrane staining specific organelles such as Calcein AM that is retained by the living cells giving off a characteristic green fluorescence, and is most commonly used for cell viability tests. Other types of biological dyes are membrane impermeable therefore require "assistance" to be internalized by the cell. Propidium Iodine (PI), Propidium Bromide (PB) and DAPI are examples of membrane impermeable dyes that will only be taken up by cells whose membranes have been compromised and will be excluded by living cells. These stains interact with the DNA of the host cell by binding to specific nucleotides within the DNA strand. Once the binding occurs, the stain molecules will exhibit intense fluorescence at a certain wavelength and colour the DNA, i.e. the nucleus of the host cell. Figure 5(a) shows the image of the stained nucleus of the African monkey kidney cells with PI and 5(b) shows human melanoma M4T cells stained with Calcein AM.

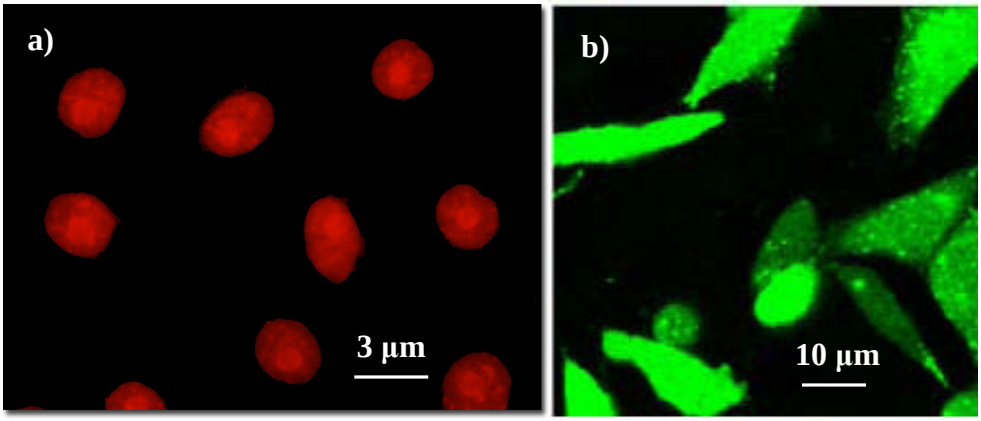

Figure 5: (a) Image of the stained nucleus of African monkey kidney cells using PI [6]. (b) Image of stained human melanoma M4T cells with Calcein AM [7].

In order to view the fluorescent signature of the stained organelle or individually tagged cells, a fluorescence microscope with appropriate fluorescent filters and imaging system is normally required.

There are some stains such as Trypan Blue that are not fluorescent. This stain, which was also used for my preliminary transfection studies as detailed in chapter 3, is membrane impermeable. When Trypan Blue is internalized by the cell, it causes blue staining around the area of entry that is visible without the need of filters and excitation illumination.

The introduction of biological stains into cells by means of chemically, mechanically or optically modifying the cell membrane is an important task that provides the means for identifying and viewing and even classifying cell organelles, individual cell or tissues and that would otherwise appear transparent. However, the ability to safely introduce foreign material into cells without compromising the cell viability offers far more exciting prospects. The introduction of drugs or nucleic acids inside cells could potentially allow us to influence the genetic profile of cells in a way that we could direct

or hinder the expression of specific proteins by promoting or silencing the corresponding genes. This could potentially enable us to study the suitability of therapeutic drugs and their side effects to the host pathogenic cell. A prerequisite for these studies is to extend the range of substances that can successfully be introduced into the cell cytoplasm.

In the context of optical transfection, the introduction of biological stains into cells is normally performed as part of preliminary experiments in order to assess the viability of the irradiated cells and the efficiency of the process at certain irradiance level and laser dose duration. What follows next, is the introduction of nucleic acids into cells that encode for a specific protein of known structure and properties for example a fluorescent protein. Such DNA sequences encoding for fluorescent proteins such as the Green fluorescent protein (GFP), the *Discodeum* red fluorescent protein (DS-Red) are widely used in the literature in the context of cell transfection. Figure 6 shows transfection of CHO cells with GFP (6(a)) and DS-Red (6(b)) fluorescent proteins. In contrast to dyes, the fluorescent protein genes can be introduced into organisms and be stably maintained within their genome throughout the organism's life cycle. The expression of well understood gene reporters in the transfected cell acts as a proof of principle for the selective modification of the cell genome, paving the way for advanced and elaborate investigation of the mechanisms of gene expression, mutations and proteinomics in cells.

The section that follows gives a brief introduction on the nature and structural characteristics of genes and the process of decoding the genome and protein expression which is the essence of cell transfection.

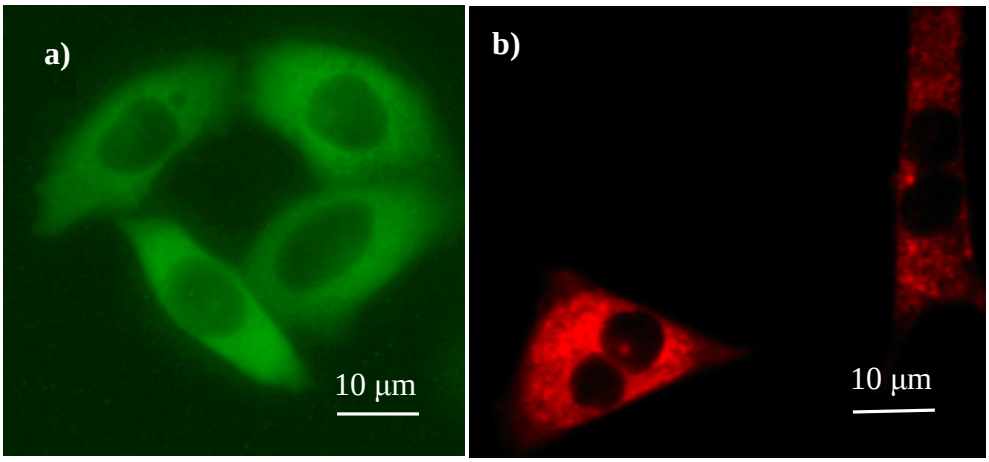

Figure 6: (a) shows the expression of GFP by Chinese hamster ovary (CHO) cells and (b) shows the image of DS-Red expressing CHO cells [8].

2.1.4 Expression of genetic information

Genes are the basic units of hereditary information passed from the parent to the daughter organism, and affects the latter's phenotype and genotype. Genes correspond to specific parts within the DNA strand that encapsulates all the hereditary information carried by an organism. The DNA is a nucleic acid molecule which consists of organic compounds known as nucleotides which are arranged in a chain form and assemble two intertwined helical strands that develop in directions opposite to each other [9-11]. There are four different types of nucleotides, adenine (A), cytosine (C), guanine (G), and thymine (T). Two nucleotides located on opposite and complementary DNA or RNA strands are called base pairs. Each sequence of nucleotides corresponds to a specific gene which is translated by the cell into a specific chain of amino-acid molecules that constitute a protein. This sequence of nucleotides will define the three dimensional shape and function of that protein. Any defect in a nucleotide chain will have a direct impact on the

shape and function of its corresponding protein, causing changes in the hereditary trait of the organism. Genes are encoded within the chromosomes, which consist of compacted DNA and proteins, with the proteins being responsible for arranging, packaging the DNA strands and allowing access to the genomic information, as well as regulating the expression and function of other proteins. Each chromosome contains a very long DNA helical strand on which thousands of genes are located. A human cell typically contains two meters of DNA. More specifically it comprises of 22 pairs of different non-sex chromosomes, and the X and Y chromosomes termed the sex chromosomes, giving a total number of 46 chromosomes. Figure 7 shows the DNA composition of nucleotide pairs and the congregation of DNA strands into chromosomes located in the cell nucleus.

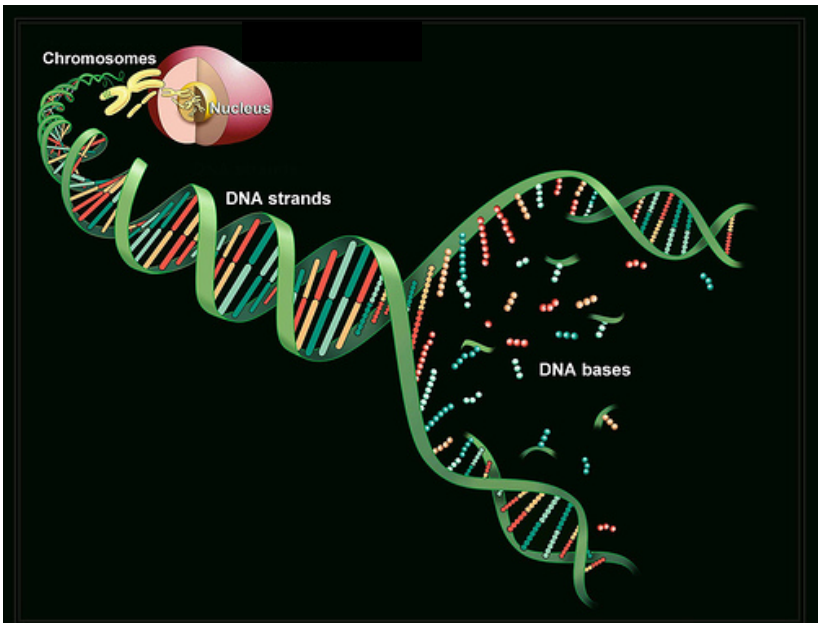

Figure 7: DNA consists of a chain of different sequences of nucleotides that are called genes. The DNA strands are neatly arranged and packaged by specific proteins in the chromosomes which are located in the cell nucleus [12].

But how do cells decode the genome? As previously discussed, the genetic code is

encoded on the DNA molecule within the chromosome, and each gene corresponds to a specific sequence of nucleotides in the DNA strand. When the cell requires a particular protein, the process of transcription and translation begins. This process starts by transcribing the corresponding DNA nucleotide sequence into messenger RNA (mRNA). RNA stands for ribonucleic acid and it is a single-stranded molecule, with a slightly different composition to DNA. There are many types of RNA that play various roles in the process of protein synthesis. Other types of RNA can be described as non-coding RNA's that help mediate the translation process such as transfer RNA (tRNA) or ribosomal RNA (rRNA). As soon as the transcription of DNA into mRNA has been achieved, then the latter is exported into the cytoplasm and transported to the ribosomes, which host protein synthesis (translation). Every three nucleotides of mRNA (a codon), correspond to an amino acid, the individual subunits of the new protein. Each codon is encoded by a small tRNA into the ribosomes where the final part of the translation process occurs. The translation process is mediated by the enzymatic action of the ribosomes which contain a structural form of RNA termed rRNA [1, 10]. Figure 8 shows the process of genome expression in cells. Although there are other intermediate steps in the process that vary amongst organisms, all cells, from bacteria to human cells, decode their genome by following the above basic process which is referred to as the central dogma of molecular biology.

One of the most important questions in genetics is what the mechanisms which govern gene expression are and what therefore regulates the differentiation of cells in a multicellular organism. Initially, scientists assumed that different cell types of the same organism possessed different genomes, therefore exhibiting different properties, such as

shape and function. However, later experiments provided evidence that different cells of a multicellular organism actually contain the same genes, with the genome being preserved during cell differentiation. What governs cell differentiation and therefore the type of a cell in an organism is the process of gene expression.

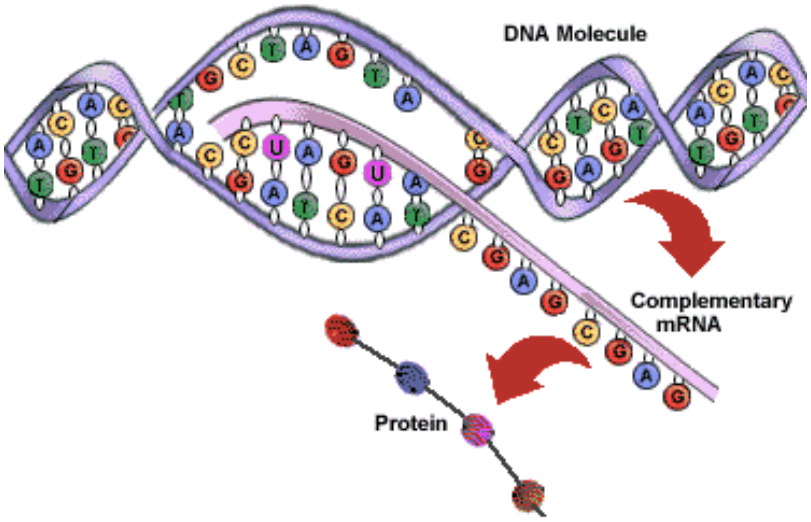

Figure 8: The simplified process of gene expression in cells. The DNA is transcribed into RNA which subsequently enters the cytoplasm and is directed to the ribosomes where the translation of RNA into the encoded protein takes place [13].

Although a cell genome may contain enough information to construct thousands of different RNA sequences, each cell will only express a fraction of these proteins that result in the unique character and function of that particular cell. There are a number of mechanisms that control the translation process and therefore the expression of a particular protein, including mechanisms imposed by the cell itself or from external stimuli.

The understanding of gene function and what happens to the cellular processes when a particular gene is for example, faulty or missing altogether, is of particular importance in

genetics as it could provide valuable information in the attempt to ascertain the origin of human genetic diseases. The role of transfection is vital for this success. The introduction of a modified, mutant gene inside a mammalian cell during transfection can cause slight changes in a portion of the cell genome in order to observe variations in the function of the corresponding protein. This could produce a protein that will dominate over another one's function and hence change the phenotype in the cell of interest, or can even silence an existing gene. The first step of this process is the chemical synthesis of the mutant gene, in other words the engineering of the DNA molecule that contains the desired portion of altered nucleotide sequence. The process of isolating, analyzing and copying a desired part of the DNA strand is nowadays an easy task to accomplish thanks to breakthroughs in genetic engineering in the last 30 years. The engineered gene that encodes for a certain protein is commonly introduced inside a bacterial plasmid DNA that will act as the host vector for the altered gene. The plasmid that carries the modified gene sequence can be readily purified from this bacterial environment. Through transfection, transient permeabilization of the cellular membrane, the plasmid DNA is inserted inside the cytoplasm of the cell. Whether the new gene is incorporated transiently into the nuclear genome or is permanently expressed, we distinguish between the terms transient and stable transfection. During transient transfection, the transfected gene is expressed for a short period of time. The foreign DNA is normally lost during mitosis, and therefore is not passed to the daughter cells. Transient transfection is typically used for studying how certain genetic alterations in a gene sequence can affect the function of the targeted gene and its encoding protein functions. However, if one wishes to maintain long term genetically modified (transgenic) cell cultures, stable transfection must occur. In order to

achieve this, the already transfected cell culture is exposed to another foreign gene which normally offers antibiotic resistance to a certain substance for example a toxin and is subsequently transfected. Some of the previously transfected cells uptake the new gene, and therefore become resistant to the toxin that encodes. If we subsequently add this toxin into the cell culture, then only the cells that have become resistant will survive, whilst the rest of them, the non-transfected ones will die [9]. Subsequently, the gene of interest is maintained during mitosis and passed onto the daughter cells. Apart from naked or plasmid DNA, mRNA can also be transfected into cells [14]. The introduction of mRNA inside cells provides a quicker path towards successful transfection as the task of the exogenous material to be transported through the cytoplasm and the nuclear membrane can be circumvented. However, mRNA is more sensitive to enzymatic attack than naked or plasmid DNA. Figure 9 shows the stable transfection process of a mutant gene into a cell and how that is incorporated into the cell genome.

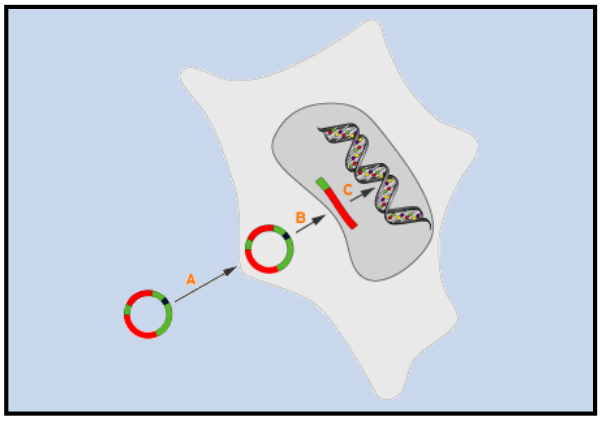

Figure 9: Steps of stable transfection. A: The plasmid DNA is introduced into the cell cytoplasm. B: From there it travels into the nucleus and C: through a complex process is incorporated into the cell's genome [15].

2.2 Laser assisted cell transfection

2.2.1 Transfection methods

Well established transfection methods include physical injection into individual cells using glass micropipettes (microinjection), local permeabilization of cells via the application of pulsed electric fields (electroporation), delivery of therapeutic agents encapsulated in viruses (viral mediated gene delivery) or in lipid-based molecules (non-viral based transfection), ballistic introduction of coated gold nanospheres (gene gun) and local permeabilization of cells via the application of diagnostic ultrasound (sonoporation)[16]. Figure 10 shows some of the most widely used transfection methods.

Cell microinjection remains the most direct technique of studying the dynamics of the intracellular components as well as their interaction with a variety of membrane impermeable substances. This technique involves direct microinjection of the DNA or other substances into the cytoplasm or the nucleus of the recipient cell using a microscopic fine glass micropipette. Cell microinjection generally does not lead to sample contamination despite the fact that the cells might be microinjected inside a non-sterile environment for a long period of time. It provides very high efficiency, approaching 100%, due to its direct and invasive nature. The dosage of the injected substance can be accurately controlled before being introduced and furthermore, more than one probe can simultaneously be injected into one sample. Figure 10(a) shows the membrane perforation of an embryo cell using a micropipette during microinjection. A number of cell lines can be microinjected however there is a lower limit in the size of a

cell and at the same time an upper limit in the number of cells per trial that can be successfully transfected using this approach.

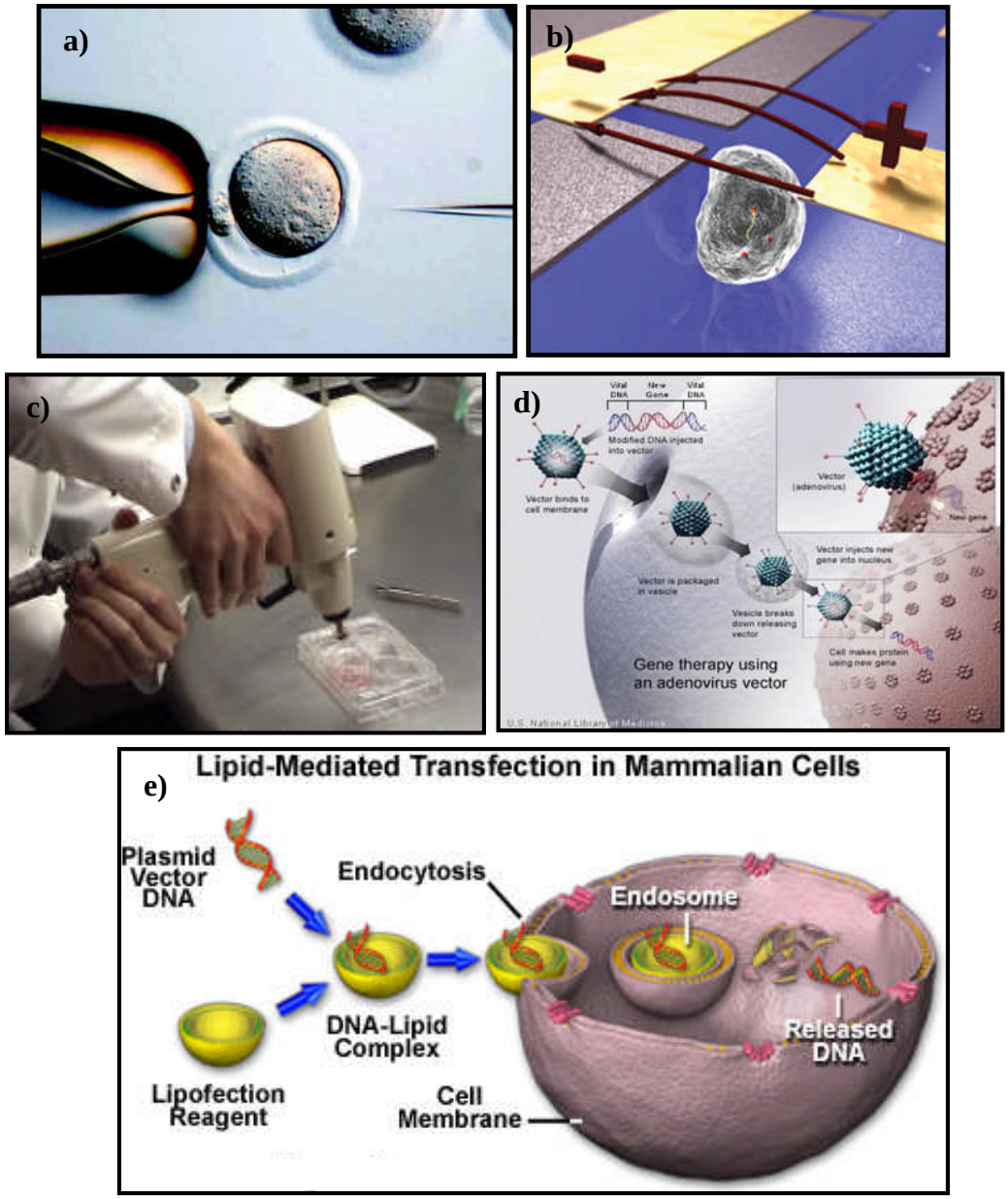

Figure 10: Transfection methods (a) Microinjection[17], (b) Electroporation [18], (c) Gene gun [19], (d) Viral mediated transfection [20], (e) Lipid-mediated transfection [21].

Additionally, significant amounts of scientific expertise and competence, as well as a complicated experimental layout are required in order to carry out cell microinjection [22].

One of the most important transfection methods is electroporation where an electric field is applied across the cell sample treating simultaneously a large number of cells. If the voltage is set to its optimum value, the cells will survive the process, become transfected and proceed with division which basically provides the evidence for safe cell transfection. However, when the applied voltage is above the threshold for safe membrane permeabilization, physiological cell changes occur that can become quite dramatic and irreparable. This can lead to cell necrosis, which is cell death in response to an external traumatic stimulus. Electroporation, as shown in figure 10(b), is a versatile method for transfecting a large number of cells lines with high throughput. One of the disadvantages of this method is that the whole sample under test is subjected to the external applied voltage not giving the opportunity to treat individual cells inside the sample, although recently transfection of a single neuron has been demonstrated [23]. Some of the problems associated with electroporation are that the voltage thresholds for lethal and optimum transfection do not vary significantly, raising concerns for high cell death rates and therefore the viability efficiency of the method, as well as the lack of precise targeting of individual cells or intracellular compartments. Also, each cell type requires specific electroporation parameters, hence the process becomes more complicated when dealing with whole tissues due to the large variations in the cell types [23-26].

The gene gun or Biolistic Particle Delivery System, shown in figure 10(c), was originally

designed for delivering genetic material inside plant cells that have a rigid and hard to penetrate cell wall. Disadvantages of this method are that the area of deposition of the "genetic bullet" inside the targeted cell cannot be easily pre-determined and also a significant number of cells are obliterated by the impact [27-30].

Viral mediated cell transfection is another very popular transfection technique. Viruses are infectious biomolecules that act as vectors or vessels which encapsulate a gene of interest. The mutant gene or therapeutic substance is enclosed inside the virus genome or body which is subsequently introduced inside the infected cell. The virus protects the DNA from degradation and ensures its safe transportation to the nuclear envelope. The viral vector mediated transfection technique is very efficient for genetic material delivery compared to other transfection techniques. However, there are numerous ethical, toxicological issues associated with the employment of such a method, which may raise concerns about its clinical safety and long-term efficiency. Figure 10(d) shows the process of viral gene delivery within a cell during viral mediated cell transfection [31].

Non-viral vector mediated chemical transfection involves bathing the cells inside a chemical solution which causes pores to appear on the cell membrane. Some of the chemical substances used, include lipids such as liposomes, calcium phosphate and the DEAE-Dextran. These substances enhance membrane fusion, DNA concentration on the cell membrane and nuclear targeting in order to increase the probability for gene delivery. Despite the relatively high transfection rates, specific physical and metabolic impediments have been reported that limit the efficiency of the gene transport across the cytoplasm to the nucleus. A large proportion of the internalized plasmid DNA is absorbed

by the lysosomes which trap it and progressively degrade it. In addition, a small portion of the remaining plasmid DNA is subsequently absorbed by the cytoplasm, hence reducing further the amount of genetic material penetrating the nucleus of the cell. These intra-cellular compartments introduce great difficulty in the delivery of therapeutic genes [32]. Figure 10(e) shows the process of lipid-mediated cell transfection.

Sonoporation is another developing transfection method. It utilizes ultrasound waves to transiently permeabilize the cell membrane and hence allow naked or plasmid DNA to enter the cell cytoplasm. Recent studies have also shown that pulsed ultrasounds in the presence of microbubbles lead to enhanced permeability of the cell membrane, caused by the mechanical effects of expansion and contraction and subsequent collapse of the microbubbles in response to the sonication of the cell sample [33, 34]. Upon collapse of the microbubbles, fast moving liquid jets are formed that cause local membrane disruption which leads to membrane permeabilization. Sonoporation has successfully been applied for *in vitro* gene transfer inside cells and also preliminary *in vivo* applications have also been reported.

As discussed, a number of successfully and widely employed transfection techniques are available, each of which comes with both advantages and disadvantages. The suitability of each technique for a specific application will heavily depend on the cell type one wishes to transfect, the number of targeted cells, whether the studies are performed *in vitro* or *in vivo*, in combination or not with other optical, electrophysiological or biomedical techniques and with the least amount of damage. Laser assisted transfection has proved to be very effective for transfection studies *in vitro*, in a non-invasive, sterile

and non-toxic manner of a small or relatively high cell population, with high transfection efficiency, adhered or suspended, in combination with a variety of optical techniques such as optical trapping, microscopy or electrophysiology. Lasers can be easily interfaced with microscope systems allowing single cells and sub cellular organelles to be transfected using a multitude of wavelengths and laser modalities. In combination with electrophysiological patch clamp studies, a state of the art optical, biological and photochemical examination of the biological sample can be readily conducted. During laser transfection, the laser can be easily directed and target the desired area on the cell membrane, near the centre or the edge of the cell with very high spatial precision.

2.2.2 A brief review of laser assisted cell transfection. The merits of femtosecond pulses

The concept of laser assisted cell transfection is one that goes back to 1984 when a tightly focused laser beam was used by Tsukakoshi *et al.* to create a self-healing pore on the membrane of a cell, thus allowing the exogenous genetic material to slip into the cell cytoplasm [35].

Table 1 gives a brief overview of optical transfection as performed in the literature, since Tsukakoshi's first successful transfection studies, using a variety of CW and pulsed laser sources mostly in the UV and NIR part of the spectrum and at a range of pulse durations. A broad range of cell lines have been irradiated and successfully optically perforated, from tobacco protoplast plant cells to highly complex cell lines such as neuronal and embryonic stem cells [36-45].

	Laser source & wavelength	Transfected cell lines	Advanta-ges	Dis-advantages	Physical Mechanism
CW operation	Argon Ion (488nm) [36, 37], Violet diode (405nm) [46]	CHO [37, 46], NIH_{3T3} Murine fibroplast cells [36]	Inexpensive & compact laser sources may used [46]	High irradiance threshold, Collateral damage, High cell death rates	Single photon absorption, photochemical effects
ns pulses	Nd: YAG (355nm) [35, 39], Nd: YAG (1064nm)[38]	Rat kidney cells[35], Fibrosarcoma HT1080-6TG cells [39], Human breast adenocarcinoma cells [38]	Cheaper laser sources than fs laser sources, readily available ns laser sources (ease in generation)	Violent mechanical effects i.e. shock wave emission & cavitation, Collateral damage	Plasma formation primarily due to linear photon absorption.
ps pulses	Nd: YAG (1064nm)[47]	Tobacco protoplast plant cells [47]	Less violent mechanical effects and collateral damage, than CW and ns pulses	Possible complexity in generating ps laser pulses, Mechanical effects such as shock wave and cavitation lead to collateral damage	Plasma formation due to primarily linear photon absorption
fs pulses	Ti: Sapphire (NIR) [14, 40, 42-45]	CHO cells [40, 45], Canine kidney cells[42], Zebrafish embryos [43], Astrocytes [44], Primary rat neurons [14]	Low irradiation threshold & high peak powers; Localized energy deposition, no heating effects, minimum collateral damage	Expensive laser sources	Photochemical effects as a result of multiphoton plasma formation

Table 1: An overview of CW and pulsed laser transfection of cells as reported in the literature and the corresponding physical mechanisms. CW irradiation has been excessively used in near UV wavelengths for cell transfection, however such approach is associated with ablative effects caused by heating and linear photon absorption, severely affecting the cell viability. In pulsed laser operation, ns pulses have been a very popular choice in the literature, since they provide membrane perforation at lower irradiance thresholds than CW irradiation. However, ns irradiation of cells results in violent mechanical effects, such as plasma induced shock wave and cavitation bubbles which induce collateral damage near the target area. As the pulses become shorter in time i.e. in the ps range the irradiance threshold for plasma formation reduces accordingly. In response to this, the mechanical effects become less

pronounced and not significant collateral damage is observed. At pulse durations of the order of fs, due to the dominant multiphoton ionization at the area of interaction, the deposition of energy is ultra confined leading extremely fine “cutting” on the membrane which is mediated by photochemical effects. Collateral damage is minimised therefore fs pulses appear to be the safest option for treating cells.

Distinctly, laser sources at UV and visible wavelengths were the first to be investigated for cell transfection due to the absorption observed at this spectral regime by various membrane constituents, particularly in the presence of dyes such as phenol red. CW laser sources such as diode lasers at near UV wavelengths have been a popular approach as they are inexpensive and compact. However, membrane perforation by means of CW irradiation requires considerably high irradiance thresholds which result in significant temperature increase at the irradiated volume. This can lead to strong ablative effects on the cell membrane and violent material displacement, followed by appreciable collateral damage that is associated with high cell death rates.

Pulsed laser irradiation has been employed at a range of pulse durations in the ns, ps and fs scale. Nanosecond pulses have been widely used for optical transfection of cells and tissues however their effects on biological matter have been associated with violent mechanical effects such as shock waves and cavitation. Such phenomena cause permanent disruption at the area of interaction and collateral damage due to the linear nature of the photon absorption at the target region. As the duration of the pulses becomes shorter, the induced mechanical effects become less severe, due to the lower irradiance thresholds required for membrane rupture. Ps pulses which lie between the ns and fs region, have also been employed for optical transfection but only moderately potentially due to the complexity of the laser systems involved for their generation [48].

Upon ps irradiation, cell perforation occurs due to the plasma induced mechanical effects which are less pronounced compared to ns pulses and are associated with less heating and collateral damage.

The advent of fs laser sources, especially with the development of the Kerr lens ML Ti: Sapphire laser in 1990, with their reliability, robustness and ease in use, has revolutionized optical transfection [49, 50]. The most commonly used lasers in fs cell transfection are the Ti: Sapphire ($Ti:Al_2O_3$) lasers, primarily due to their reliability, ease in use both in CW and ML operation, the usefulness of a wide range of parameters, such as the very short pulse durations and the corresponding broad spectral range in the near infrared regime that extends within the 700-1000 nm region. Focused fs pulses, due to the high peak powers they exhibit, carry sufficient density of photons to initiate non-linear phenomena such as multiphoton absorption of photons precisely at the location of the focus, inducing fluorescence at wavelengths shorter than the incident pump pulses. Due to the intensity-dependent nature of the multiphoton process, the use of fs pulses for optical transfection offers a high degree of spatial confinement of the deposited energy, causing fine, highly localized disruptive effects at the target area, thus preventing any collateral damage. The high spatial localization achieved by fs pulses allows for *in situ*, positionally dependent experiments such as that required when studying neuronal activity and signaling [51].

The use of fs laser pulses for transient membrane perforation for purposes of gene delivery, photoporation, was first reported by Tirlapur and Koenig in 2002. In this experiment, a ML Ti: Sapphire laser was used, emitting 100 fs laser pulses at 80 MHz

repetition frequency. Photoporation studies were successfully performed in CHO cells and rat-kangaroo epithelial cells during which the laser beam was tightly focused and positioned on the cell membrane and transiently perforating it. This permitted the surrounding plasmid DNA, encoding for GFP, to diffuse into the cell cytoplasm [40]. The advantages of using ultrashort pulses for optical transfection soon after became apparent. A number of successful transfection attempts using fs lasers were subsequently reported using a variety of cell lines [42, 43, 45] most importantly neurons [14, 44] and human stem cells [52]. The ultra-precise energy deposition achieved by focused fs pulses has allowed for optical transfection to be performed in combination with other position sensitive optical techniques, such as optical tweezers [53] as well as electrophysiological patch-clamp studies [54].

2.2.3 Mechanisms of femtosecond laser transfection

2.2.3.1 Laser induced optical breakdown

The understanding of the physical mechanisms governing fs cell nanosurgery and specifically photoporation is of vital importance if one wishes to develop further this technique and increase its efficiency. A thorough insight into the nature of the laser-cell interaction could lead to optimization of the photoporation parameters further increasing its applicability to a wider range of cell lines ultimately tissues, *in vitro* or *in vivo*, in a safer manner without compromising the cell viability.

Although a great deal of experimental work on cell transfection has been reported using

lasers, the physics behind the working mechanisms ruling this process remained elusive only until recently. When high intensity laser pulses are tightly focused into a transparent medium, such as water, they can produce free-electron plasma in that medium through multiphoton or single photon processes, depending on the laser parameters, through a process called laser induced optical breakdown (LIOB).

Optical breakdown and its effects in solids [55] as well as liquids has been extensively studied. Depending on the laser irradiance, optical breakdown in solids can cause material defects and permanent damage. With further increase of the laser irradiance, the pressure rise in the breakdown region could lead to the development of a shock wave leading to micro-cracks and further material impairment. Laser induced effects particularly in liquids have raised considerable interest due to their relevance and connection to medical and biomedical applications of lasers [56]. In liquids, electron plasma formation due to *nanosecond* optical breakdown, leads to mechanical effects such as generation of a strong shock wave and cavitation bubble formation that contains the vaporised material. The cavitation bubble oscillates and subsequently collapses as a result of hydrostatic pressure resulting in the damage of the targeted material. In biological matter, shock wave and cavitation are known to be the cause of tissue displacement, and in the context of transfection can be responsible for membrane disruption and permeabilization [57]. For shorter pulses, in the *picosecond* range, the required intensity threshold is reduced as the peak pulse power is increased leading to less pronounced mechanical effects and a reduction in collateral damage in the vicinity of the breakdown area. The use of ultra short *femtosecond* laser pulses almost eliminates the appearance of mechanical effects and the associated heating of the affected volume as the optical

breakdown relies almost entirely on a multiphoton process [57, 58]. The strong non-linear dependence of the fs optical breakdown on intensity produces ultra-fine effects in the targeted area with high spatial resolution. As a result of that, fs pulses become ideal tools for precision dependent nanosurgery for example ocular laser surgery as well as laser-assisted cell transfection.

2.2.3.2 Description of the femtosecond optical breakdown in water

In order to elucidate the mechanisms responsible for optical breakdown in biomaterials, a number of theoretical models and numerical simulations have been developed identifying irradiance thresholds at which laser-induced mechanical, thermal and photochemical effects occur [56, 57]. Most of the theoretical and experimental investigation of optical breakdown in liquids has been conducted using distilled water, as water is the primary constituent of biological matter. Time resolved observations and theoretical models of the laser-induced effects in water, such as cavitation, bubble formation and stress-wave propagation have been developed for various irradiances, pulse durations and laser wavelengths [58-60].

When high intensity ultra short laser pulses interact with matter, simultaneous absorption of multiple photons may occur leading to the excitation of an electron from a low energy state to a higher energy state. The non-linear response of the material will be proportional to I^m, where I is the intensity of the laser beam at the target and m the number of photons simultaneously absorbed. Another photoionization process, tunneling ionization, also plays an important role and contributes towards the creation of free carriers in the

conduction band. The interplay of multiphoton and tunneling ionization leads to free electron plasma formation that is responsible for the mechanical and photochemical changes induced in water upon laser irradiation. Figure 11 shows the process of multiphoton and tunneling ionization. This process is reported as optical breakdown in water with the associated material changes depending heavily on the laser irradiance. The process of plasma formation during laser-induced optical breakdown in transparent material is shown in figure 12.

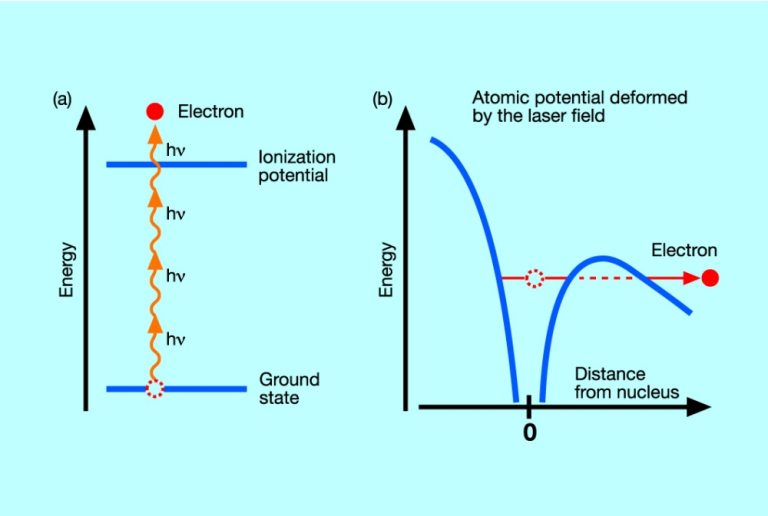

Figure 11: (a) When the energy required for an atom or molecule to be ionized is greater than the energy of the incident NIR or visible photons, then there is a probability that multiple photons will be simultaneously absorbed and cause the transport of an electron from the ground to an excited state. That may occur, provided that the incident laser field is very intense, as in the case of ultra-short laser pulses. This is known as multiphoton excitation occurs when intense laser radiation interacts with matter. (b) Due to the intensity of the incident electric field, the ionization potential may be strongly distorted therefore bound electrons may travel through the potential barrier and become free [61].

It should be noted, that the terms intensity and irradiance are used here interchangeably and refer to the energy of the EM field per unit time, per unit area with units W/cm^2.

In Sacchi's *et al.* [56] and subsequently Vogel's *et al.* [58] theoretical model of optical breakdown, the water was treated as an amorphous semiconductor of bandgap energy E_g = 6.5 eV. The term "free electron" plasma, which is normally used to describe ionization in gases, is used here as the abbreviated form of "quasi free" electrons that upon ionization move from the valence to the conduction band of the water molecule. The energy of a photon at 800 nm is 1.56 eV so approximately simultaneous absorption of five photons is expected for the creation of a free electron in the conduction band.

As soon as a free electron is produced in the conduction band, it can become involved in collisions with ions, a process that may lead to the electron absorbing a photon. This will increase the electron's kinetic energy and will promote it to a higher energy level within the conduction band, through a process called inverse Bremsstrahlung. When the energy of this electron exceeds the conduction band minimum by more than the ionization potential, then it has enough energy to ionize another electron from the valence band and promote it to the conduction band through impact ionization. By additional photon absorption in the conduction band, these two electrons gain enough energy to promote more electrons to the conduction band through impact ionization. Collision events between free electrons and ions may also occur that do not lead to photon absorption but to energy loss instead. The energy gain through Bremsstrahlung events needs to be faster than the energy loss through collisions if cascade increase of free electrons is to be favored, a process named avalanche ionization.

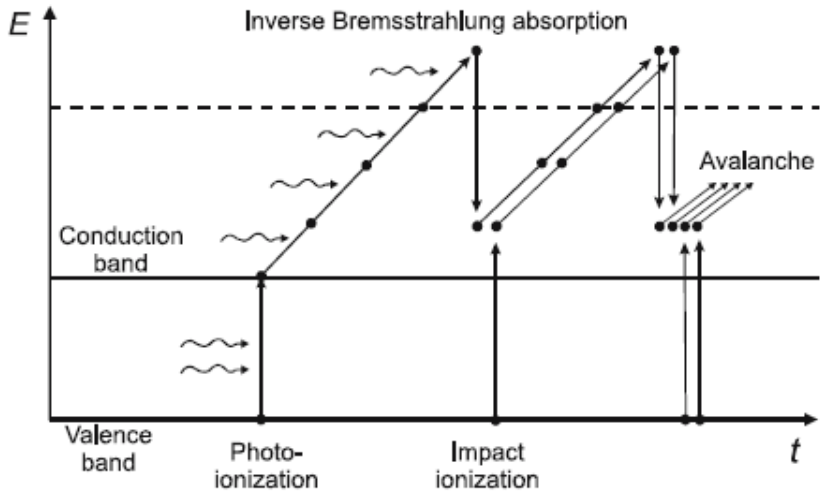

Figure 12: The plasma formation process as a result of laser-induced optical breakdown in water (water is considered as a good approximation to ocular and other biological media). The water is treated as an amorphous semiconductor of bandgap 6.5 eV. The bound electrons located in the valence band, absorb the incoming laser radiation and through photoionisation are transferred into the conduction band where they remain as semi-free electrons. Through interplay of inverse Bremsstrahlung and impact ionisation, more free electrons are generated in the conduction band. If the energy gain of the free electrons through these processes is greater than the energy loss through collisions with ions in the conduction band, then a cascade increase occurs in the number of these seed electrons, resulting in plasma formation in the absorbing medium. Optical breakdown occurs at the point when the free electron plasma density reaches the value $\rho_{max}=10^{21}/cm^3$. In the case of fs irradiation, the photoionization process is dominated entirely by multiphoton ionization [58].

Optical breakdown is defined to be the laser irradiance required to produce free electron density plasma of value $\rho_{max}=10^{21}/cm^3$ during a laser pulse and in the case of fs pulses is the threshold for minute bubble formation with life time of few tens of ns [59]. In their theoretical simulation, Vogel *et al.* investigated fs plasma formation and plasma induced

effects over a range of irradiances starting from well below the optical breakdown threshold up to irradiances slightly above the fs bubble formation threshold ($10^{13} J/cm^2$).

2.2.3.3 Evolution of free electron density and optical breakdown thresholds

One of the interesting features of this model is the time evolution of the free electron density produced under the influence of a laser pulse of *nanosecond* at 1064 nm and *femtosecond* duration at 800 nm as well as its dependence on the irradiance. The breakdown threshold for *nanosecond* pulses is considered to be the intensity threshold at which the first seed electrons are produced allowing for cascade ionization to take the leading role. Figures 13(a) and 13(b) show the development of the plasma density with respect to time t normalized with the respective pulse duration. The dotted lines correspond to the contribution of the photoionization in the plasma generation.

In the case of ns pulses, at the arrival of the pulse in the sample, the irradiance is very low and therefore is not enough to free up any bound electrons from the valence to the conduction band. As the pulse approaches further, the irradiance increases to a threshold value (the optical breakdown for ns pulses) at which a seed electron is created and cascade ionization can start. At that point the irradiance is so high, that cascade ionization results in the rapid development free electron plasma density ρ_c within a small fraction of the laser pulse, as evident from figure 13(a). Experimentally, this phenomenon can be observed as a decrease (below 50%) in the optical transmission of the focal volume.

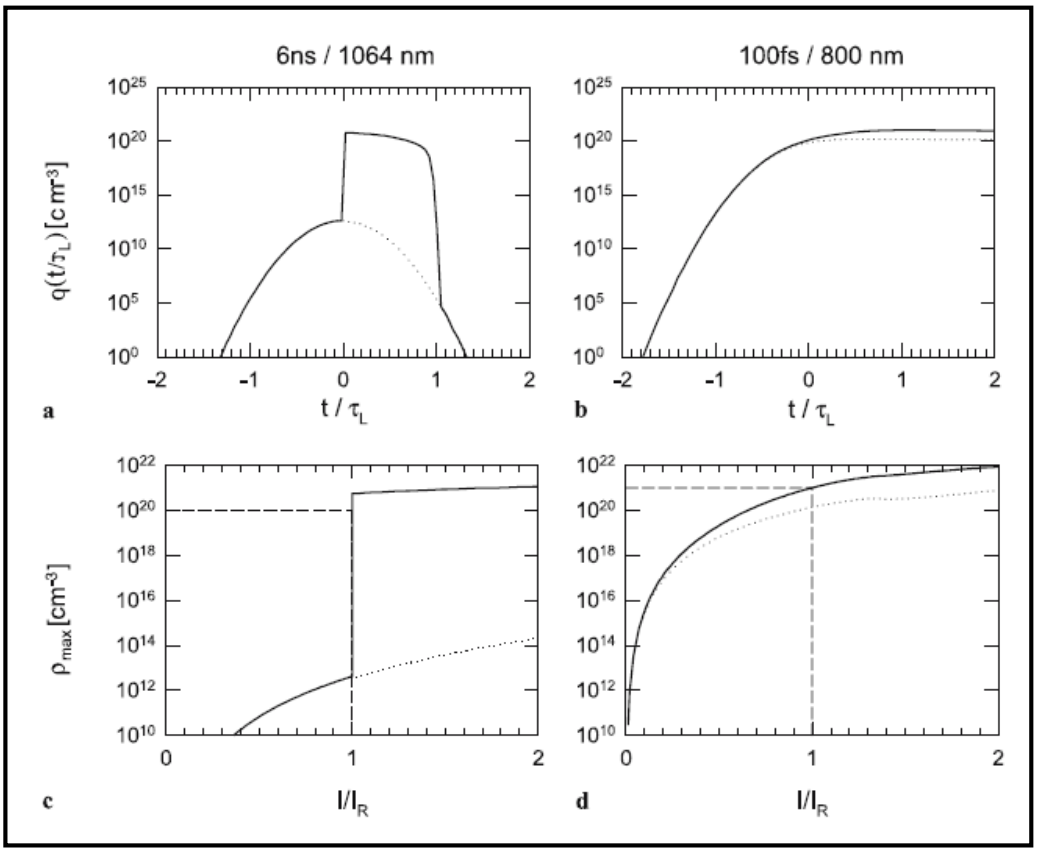

Figure 13: (a) and (b) Evolution of the free electron plasma density $q(t/\tau_L)$ with respect to time t/τ_L, normalised with the pulse duration, for 6 ns laser pulse at 1064 nm and 100 fs. For 6ns pulses, the free electron plasma density is almost solely dominated by avalanche ionization with very little contribution from multiphoton processes as opposed to fs plasma formation which, due to multiphoton ionization, can occur at a range of irradiances well below the breakdown threshold. (c) and (d) Maximum free electron plasma density ρ_{max} achieved during the course of the laser pulse as a function of the irradiance. In the case of ns pulses, the maximum plasma density rises rapidly at the irradiance threshold for breakdown. This threshold corresponds to the formation of the very first seed electrons for cascade (avalanche) ionization. At this point multiphoton ionization has weak contribution, with the plasma density increasing by 9 orders of magnitude due to cascade ionization. In the case of fs pulses, seed electrons are generated early on in the pulse passage and at low irradiances, well below the breakdown threshold. In the course of the pulse, further increase in irradiance is associated with a gradual increase in the plasma density [58].

With time, a saturation point is reached due to recombination of free electrons with holes in the valence band, a phenomenon which is proportional to the plasma density, followed by a rapid decrease in the plasma density as the pulse is trailing off. As shown by the dashed line in figure 13(a), multiphoton processes such as multiphoton ionization have little to do with the plasma formation in the case of ns pulses, a phenomenon which is almost entirely associated with avalanche ionization. Figure 13(c) shows the maximum plasma density ρ_{max} as a function of the normalized irradiance (with the threshold irradiance). It is evident, that the plasma density remains at low value at irradiances below threshold, at which point the first seed electrons are formed and the plasma density increases by almost nine orders of magnitude. This proves that avalanche ionization due to ns pulses is dominant with multiphoton ionization only having a weak contribution towards the creation of the initial seeding electrons.

In contrast to ns pulses, the model predicts that fs pulses due to their shorter time duration carry early on very high peak powers. This will result in the creation of sufficient seed electrons through multiphoton ionization during the leading edge of the pulse. An avalanche of electrons is created over a large range of irradiance levels well below the optical breakdown threshold for fs pulses, with the electron density plasma increasing gradually throughout the pulse duration reaching a plateau during the trailing edge of the pulse. This is a very interesting and important result which concludes that fs laser induced effects in media such as water can be associated with the formation of low density plasmas of the order of $10^{19} J/cm^3$ at irradiances well below the optical breakdown [57]. The gradual and smooth evolution of plasma density below optical breakdown achieved with fs pulses can allow us control over the laser induced thermomechanical and

chemical changes in the medium by tuning the irradiance level.

2.2.3.4 Mechanisms of femtosecond cellular transfection

Vogel *et al*.[58] reported a detailed comparison between experimental parameters used in the literature for cell surgery including cell transfection and their numerical simulations. This comparison reveals the nature of the disruptive effects induced by optical breakdown in biomaterials at various laser irradiances and shines light on the mechanisms of different nanosurgery procedures.

This comparison has revealed that depending on the repetition rate of fs laser pulses, nanosurgery is the product of two different physical mechanisms. The first arises from the use of fs pulses with MHz repetition rates at energies below the optical breakdown. This is also the regime of laser operation for cell transfection reported in this thesis. Transient membrane perforation of cells using fs pulses at a low irradiance level approximately $0.3\text{x}10^{12}\,\text{J}/\text{cm}^2$ appears to be the result of low density electron plasma mediated photochemical effects. The exact nature of the chemical changes involved is not well understood, but is potentially associated with the creation of reactive oxygen species at the laser focus. At higher irradiances, towards the optical breakdown threshold, there is interplay of chemical, mechanical and thermal effects that are proved damaging to the targeted cell. At large laser powers, greater than the threshold for safe transfection, bubbles of few seconds lifetime have been observed with unaided eye, potentially related to the dissociation of water molecules that may be rising from a combination of chemical bond breaking and cumulative thermal effects.

It should be stressed here that these bubbles observed under brightfield imaging during transfection experiments bare no relation to the bubble formation reported in the literature by Vogel *et al*.[58], associated with the stress wave generation and cavitation of vaporised material. The former are bubbles generated due to high power laser pulses and are associated with accumulative thermal effects. The observation of these bubbles, with less than a few seconds lifetime, has become the criterion of lethal laser dose during my transfection experiments. At energy levels used for successful cell transfection, no bubble formation of this nature should been observed as this will be a direct indication of cellular damage and death. To conclude, when we operate at this laser regime and at low electron plasma densities, no transient bubbles with sub-microsecond lifetime, associated with stress wave and cavitation, are generated during transfection. The creation of long-lived bubbles due to accumulative chemical and thermal effects at large laser powers should be avoided as they lead to cell death.

The use of fs laser pulses with kHz repetition rates and energies above the bubble-formation threshold (optical breakdown threshold) defines the second regime of nanosurgery mechanisms. At such repetition rates, it is considered that at low irradiances no accumulative chemical effects are taking place due to the long time intervals between laser pulses. At kHz repetition rates, the laser power has to be raised for biomaterial photodisruption to occur. By raising the power at irradiances just above the optical breakdown, transient bubbles of tens of ns lifetime have been observed associated with mechanical and thermomechanical disruption effects. These effects do not lead to accumulative bubble formation that could be detrimental to biomaterials as long the

irradiance remains close to the optical breakdown threshold.

2.3 Summary

The cell is the basic structural and functional unit of every living organism. An animal or a plant cell starts its life as a single cell, a fertilized egg. This egg will subsequently divide, form groups of cells, tissues, organs and finally the complete organism. This multicellular and highly complex organism consists of a variety of cells that have different functions, shape and chemistry. Despite the phenotypic and functional differences amongst cell types in the same organism, all of these cells carry the same genetic information, the same genome. Their differentiation is due to the selective gene expression that will ultimately define the characteristics, the position and the role of each cell inside the organism. Errors occurring during the decoding of the DNA or the protein expression could lead to genetic alterations causing cell malfunction, lack of certain proteins or inactivation of some others. These changes could have profound and detrimental consequences for the organism, leading to the development of serious hereditary genetic diseases. The process of understanding protein function and identifying factors that influence the gene expression in a cell are of vital importance if we are to treat and prevent undesired genetic modifications. One method of approaching this problem is cell transfection. By selectively introducing foreign genes inside a cell we could alter the cell genome at will, control and monitor variations in the protein function and how that affects the cell. Laser-assisted cell transfection offers an attractive alternative to commonly used transfection techniques. It is a highly selective method, ideal for small or large population of cells that can be performed in a non-invasive and

sterile manner and in combination with other optical techniques.

The use of fs pulses in cell transfection enables the generation of extremely confined disrupting effects on the cell membrane leading to an unprecedented accuracy in membrane targeting. The physical mechanism behind membrane photoporation is plasma mediated optical breakdown, which for ultra-short pulses is almost entirely a multiphoton process. Depending on the laser irradiance and repetition rate of the laser pulses during cell targeting, the disrupting effects could be of chemical, thermal or of mechanical nature. Due to the non-linear nature of the plasma formation, the spatial resolution of the membrane disruption is very high, and for sufficiently low laser irradiances pore sizes well below the diffraction limit can be achieved. At MHz repetition rates and irradiances well below the optical breakdown, fs cellular transfection occurs solely due to photochemical effects caused by multiphoton plasma formation in the breakdown area, with thermal and mechanical effects contributing to the photoporation process when irradiance level is approaching the optical breakdown threshold.

References

[1] B. Alberts, et al., "*Essential cell biology",* 2nd ed. (2003), Garland Science,

[2] M.J. Farabee "*On-Line Biology Book"* (2006), Web page: http://www.estrellamountain.edu/faculty/farabee/biobk/biobooktoc.html.

[3] W.K. Subczynski and A. Wisniewska, "*Physical properties of lipid bilayer membranes: relevance to membrane biological functions,"* Biochimica et Biophysica Acta (BBA) **47**(3), p. 613, 2000.

[4] Wikipedia and contributors "*Cell membrane"* (2009), Web page: http://en.wikipedia.org/w/index.php?title=Cell_membrane&oldid=265687432.

[5] M. Gregory "*The Biology Web: Membranes "* (2006), Web page: http://faculty.clintoncc.suny.edu/faculty/michael.gregory/files/Bio%20101/Bio%20101%20Lectures/Membranes/membrane.htm

[6] A. Scordato and S. Schwartz " *NIKON Microscopy website : African Monkey Kidney Cells with Propidium Iodide "* Web page: http://www.microscopyu.com/articles/fluorescence/filtercubes/green/tritchyq/tritchyqu2propidium.html.

[7] H. Benlalam, et al., "*Gap Junction Communication between Autologous Endothelial and Tumor Cells Induce Cross-Recognition and Elimination by Specific CTL,"* Journal of Immunology **182**(5), p. 2654, 2009.

[8] C. Stubbs, et al., "*The use of time-resolved fluorescence imaging in the study of protein kinase C localisation in cells,"* BMC Cell Biology **6**(1), p. 22, 2005.

[9] A. Bruce, et al., *Molecular Biology of the Cell* Fourth ed. (2002), Garland Science, Web page: http://www.ncbi.nlm.nih.gov/books/bv.fcgi?rid=mboc4

[10] B. Alberts, et al., *Molecular Biology of The Cell* Fourth ed. (2002), Garland Science, Web page: http://www.ncbi.nlm.nih.gov/books/bv.fcgi?highlight=Read,Protein,Genome,DNA,Cells&rid=mboc4.chapter.972

[11] J. Wolff, et al., " *Book section: The Mechanism of Naked DNA Uptake and Expression"*, in *Advances in Genetics*, (2005), Academic Press, p. 1.

[12] Flickr "*DNA transcription graphic 5-03"* Web page: http://www.flickr.com/photos/justhman/1238267008/in/set-72157601664657158/.

[13] A. Zamora "*Transcription of DNA to mRNA, and of mRNA to proteins"* Web page: http://www.scientificpsychic.com/fitness/transcription.gif.

[14] L.E. Barrett, et al., "*Region-directed phototransfection reveals the functional significance of a dendritically synthesized transcription factor,"* Nature Methods **3**(6), p. 455, 2006.

[15] Lonza "*Stable transfection"* (2009), Web page: http://www.amaxa.com/applications/stable-transfection/.

[16] S. Mehier-Humbert and R.H. Guy, "*Physical methods for gene transfer: Improving the kinetics of gene delivery into cells,"* Advanced Drug Delivery Reviews **57**(5), p. 733, 2005.

[17] K. Chen "*The transgenic and gene targetting facility"* Web page: http://www.aecom.yu.edu/transgenic/.

[18] A. Valero, et al., "*Gene transfer and protein dynamics in stem cells using single cell electroporation in a microfluidic devide,"* Lab on a Chip **8**, p. 62, 2008.

[19] MRC "*Medical research council webpage: Gene guns: How one researcher improved his shot"* Web page: http://www.mrc.ac.uk/Newspublications/News/MRC003469.

[20] M. Clifton, et al. "*U.S. National Library of Medicine: What is gene therapy"* Web page: http://heather.mantunes.com/therapy/Gene_therapy_homepage.html.

[21] D. Piston "*NIKON Microscopy Website: Propagation, Isolation, and Transfection of Fluorescent Protein Plasmids"* Web page: http://www.microscopyu.com/articles/livecellimaging/fpintro.html.

[22] Y.M. Shen, et al., "*Gene transfer: DNA microinjection compared with DNA transfection with a very high efficiency,"* Mol. Cell. Biol. **2**(9), p. 1145, 1982.

[23] K. Kitamura, et al., "*Targeted patch-clamp recordings and single-cell electroporation of unlabeled neurons in vivo,"* Nature Methods **5**(1), p. 61, 2008.

[24] T. Muramatsu, et al., "*In vivo electroporation: A powerful and convenient means of nonviral gene transfer to tissues of living animals (Review),"* International Journal of Molecular Medicine **1**(1), p. 55, 1998.

[25] T. Suzuki, et al., "*Direct gene transfer into rat liver cells by in vivo electroporation,"* Febs Letters **425**(3), p. 436, 1998.

[26] W.J. Buchser, et al., "*96-Well electroporation method for transfection of mammalian central neurons,"* Biotechniques **41**(5), p. 619, 2006.

[27] M.L. Chang, et al., "*Gene gun bombardment with DNA-Coated gold particles is a potential alternative to hydrodynamics-based transfection for delivering genes into superficial hepatocytes,"* Human Gene Therapy **19**(4), p. 391, 2008.

[28] N. Carsono and T. Yoshida, "*Transient expression of green fluorescent protein in rice calluses: Optimization of parameters for Helios gene gun device,"* Plant Production Science **11**(1), p. 88, 2008.

[29] M.L.M. Voiland, "*Development of the gene gun at Cornell*" Tutorial notes, Cornell University

[30] N.S. Yang and W.H. Sun, "*Gene gun and other non-viral approaches for cancer gene therapy,"* Nature **1**(5), p. 481, 1995.

[31] L.D. Kimberly, "*Toward Development of Artificial Viruses for Gene Therapy: A Comparative Evaluation of Viral and Non-viral Transfection,"* Biotechnology Progress **24**(4), p. 871, 2008.

[32] L.G. Lechardeur D, "*Intracellular Barriers to Non-Viral Gene Transfer,"* Current gene therapy **2**, 2002.

[33] P. Prentice, et al., "*Membrane disruption by optically controlled microbubble cavitation,"* Nature Physics **1**(2), p. 107, 2005.

[34] K.Y. Ng and Y. Liu, "*Therapeutic ultrasound: its application in drug delivery,"* Medicinal Research Reviews **22**(2), p. 204, 2002.

[35] M. Tsukakoshi, et al., "*A novel method of DNA transfection by laser microbeam cell surgery,"* Applied Physics B-Photophysics and Laser Chemistry **35**(3), p. 135, 1984.

[36] G. Palumbo, et al., "*Targeted gene transfer in eucaryotic cells by dye-assisted laser optoporation,"* Journal of Photochemistry and Photobiology B: Biology **36**(1), p. 41, 1996.

[37] H. Schneckenburger, et al., "*Laser-assisted optoporation of single cells,"* Journal of Biomedical Optics **7**(3), p. 410, 2002.

[38] S.K. Mohanty, et al., "*Laser-assisted microinjection into targeted animal cells,"* Biotechnology Letters **25**(11), p. 895, 2003.

[39] W. Tao, et al., "*Direct gene transfer into human cultured cells facilitated by laser micropuncture of the cell membrane,"* Proceedings of the National Academy of Sciences of the United States of America **84**, p. 4180, 1987.

[40] U.K. Tirlapur and K. Konig, "*Cell biology - Targeted transfection by femtosecond laser,"* Nature **418**(6895), p. 290, 2002.

[41] E. Zeira, et al., "*Femtosecond infrared laser - An efficient and safe in vivo gene delivery system for prolonged expression,"* Molecular Therapy **8**(2), p. 342, 2003.

[42] V. Kohli, et al., "*Reversible permeabilization using high-intensity femtosecond laser pulses: Applications to biopreservation,"* Biotechnology and Bioengineering **92**(7), p. 889, 2005.

[43] V. Kohli, et al., "*An alternative method for delivering exogenous material into developing zebrafish embryos,"* Biotechnology and Bioengineering **98**(6), p. 1230, 2007.

[44] M. Lei, et al., "*Femtosecond laser-assisted microinjection into living neurons,"* Journal of Neuroscience Methods **174**(2), p. 215, 2008.

[45] D. Stevenson, et al., "*Femtosecond optical transfection of cells: viability and efficiency,"* Optics Express **14**(16), p. 7125, 2006.

[46] L. Paterson, et al., "*Photoporation and cell transfection using a violet diode laser,"* Optics Express **13**(2), p. 595, 2005.

[47] H. Schinkel, et al., "*Infrared picosecond laser for perforation of single plant cells,"* Biotechnology and Bioengineering **99**(1), p. 244, 2008.

[48] T. Omatsu, et al., "*MW ps pulse generation at sub-MHz repetition rates from a phase conjugate Nd:YVO4 bounce amplifier,"* Optics Express **15**(15), p. 9123, 2007.

[49] D.E. Spence, et al., "*60-fsec pulse generation from a self-mode-locked Ti:Sapphire laser,"* Optics Letters **16**(1), p. 42, 1991.

[50] S. Backus, et al., "*High power ultrafast lasers,"* Review of Scientific Instruments **69**(3), p. 1207, 1998.

[51] M.C. Fischer, et al., "*Self-phase modulation signatures of neuronal activity,"* Optics Letters **33**(3), p. 219, 2008.

[52] A. Uchugonova, et al., "*Targeted transfection of stem cells with sub-20 femtosecond laser pulses,"* Opt. Express **16**(13), p. 9357, 2008.

[53] B. Agate, et al., "*Femtosecond optical tweezers for in-situ control of two-photon fluorescence,"* Optics Express **12**(13), p. 3011, 2004.

[54] J. Baumgart, et al., "*Quantified femtosecond laser based opto-perforation of living GFSHR-17 and MTH53 a cells,"* Optics Express **16**(5), p. 3021, 2008.

[55] C.B. Schaffer, et al., "*Micromachining bulk glass by use of femtosecond laser pulses with nanojoule energy,"* Optics Letters **26**(2), p. 93, 2001.

[56] C.A. Sacchi, "*Laser-induced breakdown in water "* Journal of the Optical Society of America B-Optical Physics **8**(2), p. 337, 1991.

[57] J. Noack, et al., "*Influence of pulse duration on mechanical effects after laser-induced breakdown in water,"* Journal of Applied Physics **83**(12), p. 7488, 1998.

[58] A. Vogel, et al., "*Mechanisms of femtosecond laser nanosurgery of cells and tissues,"* Applied Physics B-Lasers and Optics **81**(8), p. 1015, 2005.

[59] A. Vogel, et al., "*Femtosecond-laser-induced nanocavitation in water: implications for optical breakdown threshold and cell surgery,"* Physical Review Letters **100**(3), 2008.

[60] A. Vogel and V. Venugopalan, "*Mechanisms of pulsed laser ablation of biological tissues,"* Chemical Reviews **103**(5), p. 2079, 2003.

[61] W. Laasch and B. Vennemann "*Multiphoton Ionization "* (2009), Web page: http://hasylab.desy.de/facilities/flash/research/multiphoton_ionization/index_eng.html.

Chapter 3

Femtosecond cellular transfection using a tightly focused Gaussian beam

Introduction

This chapter explores the concept of fs photoporation and optical transfection of CHO cells using a laser beam with a Gaussian beam profile. The process of fs photoporation requires a tightly focused Gaussian beam to be positioned on the cell membrane and irradiated with short bursts of light. Optical transfection by means of a tightly focused Gaussian beam has been explored excessively in the literature using a variety of laser wavelengths in the UV, visible and NIR spectral range in both CW and pulsed laser operation at a range of pulse durations.

Due to the non-linear nature of the membrane perforation, there are stringent requirements in the accurate positioning of the laser focus on the cellular membrane. This introduces difficulties in alignment hence any significant mismatching between the laser focus and cell membrane results in an associated reduction in the transfection rate. Herein, I present a thorough study on the transfection rate of CHO cells as a function of the axial position of the cell membrane with respect to the laser focus. This provides a good insight into the “useful” axial range over which transfection can be achieved without jeopardizing the efficiency of the method. A series of AFM images were also obtained, illustrating the pore formation on the cell membrane of CHO cells as a function

of laser power. This study offers a qualitative view of the surface morphology of the photoporated cells, offering a useful aid to our current understanding of the photoporation process.

3.1 Propagation properties of a Gaussian beam

As indicated by the name, the intensity distribution of a Gaussian beam, in any plane transverse to the propagation axis, can be described by a Gaussian function. The intensity peak of such function is observed at the beam axis and gradually decreases with the radial distance, exhibiting circular symmetry [1-4]. Gaussian beams are solutions to the paraxial Helmholtz wave equation and are composed of paraxial waves whose wavefront normals (rays) form small angles with respect to the propagation axis z. The wave equation solutions describing Gaussian beams are given by:

$$E(r,z) = A_0 \frac{\omega_0}{\omega(z)} \exp\left(\frac{-r^2}{\omega(z)^2}\right) \exp(-i\varphi(r,z)) \tag{3.1}$$

where A_0 is a constant, r and z are the radial and axial positions, with r given as:

$$r = \sqrt{\left(x^2 + y^2\right)} \tag{3.2}$$

φ is a function of r and z, and ω_0, $\omega(z)$ are the waist radius and beam radius respectively. The last two terms are two important propagation characteristics of a Gaussian beam and will be detailed below.

Properties

A Gaussian beam possesses a number of interesting properties. Figure 1(a) summarizes its most common propagation characteristics. At the transverse plane z=0, the beam cross-sectional area takes its minimum value, with the radial distance from the beam axis known as the waist radius ω_0. The quantity $2\omega_0$ is called the beam waist or spot size of the Gaussian beam. At the beam waist, the wavefront is approximately planar. However, due to diffraction, as the axial distance from the beam waist increases, the wavefront normals will form small angles with the z axis, with the angular spreading described by the angle θ. In response to the angular spreading of the beam rays, the radius of the beam's cross-section at any transverse plane along the z axis, known as the beam radius or beam width $\omega(z)$, will also increase. At an axial distance from the beam waist equal to the Rayleigh range z_0, the beam width will increase by a factor of $\sqrt{2}$ therefore the beam's cross-sectional area ($\pi\omega(z)^2$) will double. The Rayleigh range is given by the formula:

$$z_0 = \frac{\pi\omega_0^{\,2}}{\lambda} \tag{3.3}$$

where λ is the wavelength of the light. The beam width as a function of the axial distance is given as:

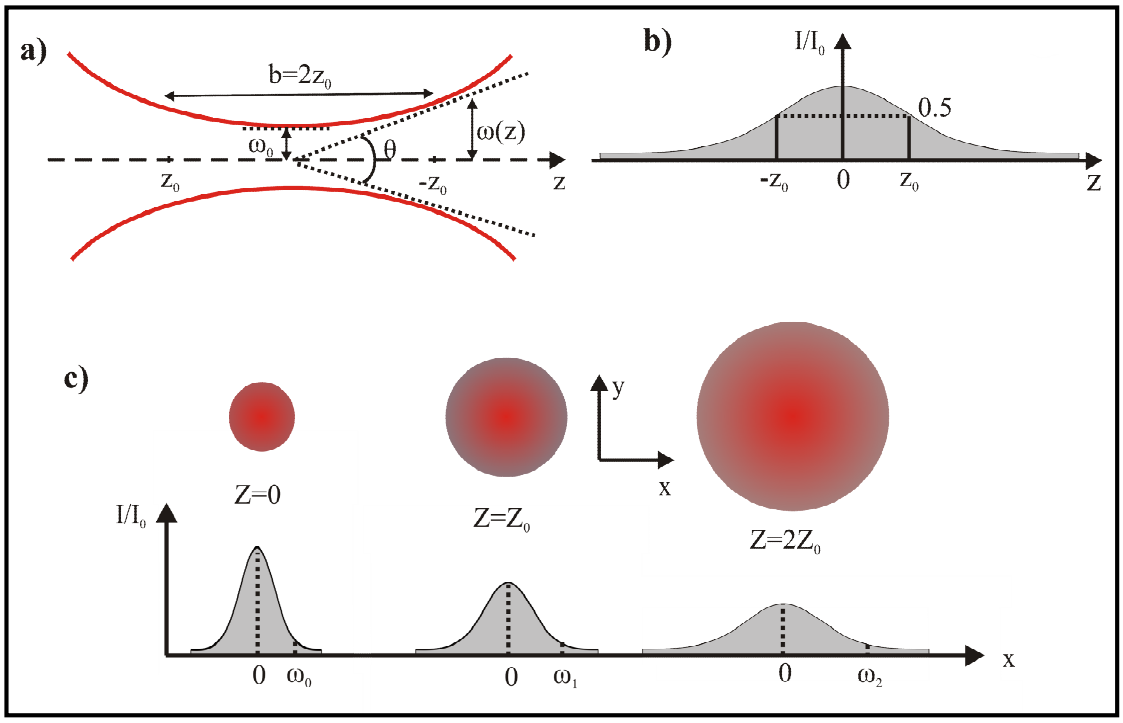

Figure 1: (a) "ω_0" is denoted as the Gaussian beam waist and corresponds to the smallest beam radius at z=0, where the field wavefront is planar. "b" is defined as the confocal parameter of the beam and represents the beam's depth of focus. At distance equal to "$b/2$" from the beam waist, equal to the Rayleigh range z_0, the beam's cross-sectional area doubles. "θ" is the total angular spread of the beam away from the beam waist. "$\omega(z)$" is the beam radius at axial distance z and is defined as the radial distance from the beam axis at which the peak intensity decreases by a factor of 0.135. (b) The normalised intensity distribution I/I_0 (at zero radial distance) along the propagation direction of the beam, with z=0 to be the beam waist which represents the point of maximum intensity. As the axial distance from the beam waist increases, the intensity gradually decays and reaches half its value at distance equal to the Rayleigh range. (c) The normalised intensity distribution I/I_0 is given as function of the radial distance ρ from the beam axis at three axial distances i) beam waist z=0, ii) Rayleigh range $z = z_0$ and iii) at $z = 2z_0$. It becomes obvious that the intensity decreases the further we move from the beam waist whilst the beam's cross-sectional area increases. This is the nature of diffraction.

$$\omega(z) = \omega_0 \sqrt{\left(1 + \left(\frac{z}{z_0}\right)^2\right)} \tag{3.4}$$

At axial distances greater than the Rayleigh range z_0 ($z \gg z_0$) the relation (3.4) reduces to:

$$\omega(z) \approx \frac{\omega_0}{z_0} z \tag{3.5}$$

The confocal parameter, b, is another significant parameter that characterizes the propagation of Gaussian beams and gives a measure of the depth of focus of the beam. For our purposes, the confocal parameter controls the axial "working distance" available for multiphoton processes such as photoporation. In either direction from the beam waist where the best focus is achieved, the beam gradually goes out of focus due to the angular spreading of the wavefront normals. The axial distance over which the beam cross-section is no greater than a factor of 2, is denoted as the confocal parameter, and its axial extend is equal to twice the Rayleigh range.

The optical intensity of a Gaussian beam can be obtained from equation (3.1) as:

$$I(r,z) = \left|E(r,z)\right|^2 = I_0 \left(\frac{\omega_0}{\omega(z)}\right)^2 \exp\left(-\frac{2r^2}{\omega(z)^2}\right) \tag{3.6}$$

where $I_0 = \left|A_0\right|^2$. On the beam axis, where r=0, the optical intensity of a Gaussian beam can be deducted from formula (3.6) as:

$$I(r=0,z) = I_0\left(\frac{\omega_0}{\omega(z)}\right)^2 = \frac{I_0}{1+\left(\frac{z}{z_0}\right)^2} \tag{3.7}$$

This relation suggests that the on-axis beam intensity will exhibit a maximum value at the beam waist, where z=0, and will gradually decay with respect to the inverse square law, in response to the increasing axial distance z. The on-axis intensity distribution of a Gaussian beam is shown in figure 1(b). At axial distance equal to the Rayleigh range, the on-axis intensity will reach half its maximum value.

At a given transverse plane along the beam axis, the optical intensity of a Gaussian beam will vary in accordance with equation (3.6), reaching its maximum value on the beam axis, where r=0, and will monotonically decrease radially away from it. Figure 1(c) shows the spreading of the beam cross-section at three different transverse planes, at the beam waist (z=0), at distance equal to the Rayleigh range ($z = z_0$) and at distance equal to twice the Rayleigh range ($z = 2z_0$). As a result of the angular increase of the beam cross-section, the peak intensity on the beam axis will decrease and the overall transverse intensity profile will broaden over a longer radial distance.

The spreading nature of a Gaussian beam imposes a degree of restriction in applications that rely on multiphoton phenomena and therefore on high photon flux over a certain axial range such as photoporation. When a Gaussian laser beam is tightly focused on a cell specimen by means of a microscope objective lens, an area of very high intensity is created at the beam focus with the rays rapidly diverging on either side of the focal point.

The degree of divergence depends on the strength of the focusing, in other words the NA of the microscope objective. In the lateral plane, according to the Rayleigh criterion, the radius of the beam focus is inversely proportional to the NA of the objective lens whereas in the axial direction is inversely proportional to the $(NA)^2$ [5]. This means that the tighter the focusing (for high NA objectives) the greater the resulting angular spreading. When performing photoporation, one wishes to achieve high photon concentration at the laser focus in order to induce multiphoton absorption required for plasma generation and subsequently membrane pore formation. It is therefore a prerequisite to achieve a focused spot as close to its diffraction limited value as possible; however this is at the expense of the beam's depth of focus, resulting in a small confocal parameter. A small confocal parameter implies a short depth of focus, hence a short axial range over which we are "allowed" a mismatch between the laser focus and the cell membrane. This particular issue introduces significant alignment difficulties when one uses a tightly focused Gaussian beam for multiphoton membrane perforation due to the stringent requirements for exactly locating the cell membrane with respect to the laser focus. For multiphoton processes in Biophotonics such as photoporation, it would be a major advance to be able to operate without such strict focus alignment requirements.

In the section that follows, I describe the methods employed for the characterization of the beam waist and temporal duration of the pulsed output of the fs Ti: Sapphire oscillator used for my photoporation experiments. Following this, I detail the experimental process and results obtained on photoporation and optical transfection of CHO cells using a Gaussian beam.

3.2 Optical transfection of CHO cells using a Gaussian beam

3.2.1 Beam profile and pulse duration measurements of the fs laser beam

Beam profile and laser characteristics

The experiments that will be discussed in the chapters that follow were all performed using a Kerr lens mode-locked Ti: Sapphire laser (MIRA, Coherent) which emits NIR pulses of approximately 100 fs duration at a central wavelength 790 nm, repetition rate 80 MHz and 1 W average output power. The energy per pulse at the laser exit was estimated to be 12.5 nJ and the associated pulse peak power 0.125 MW.

The beam diameter at the laser exit was measured using a laser beam profiler which captured, recorded and displayed the transverse intensity profile of the laser beam based on the scanning knife-edge technique. Figure 2 shows the images of the transverse intensity profile of the laser beam near the laser exit. The bottom left window provides the numerical measurement of the beam spot size corresponding to the $1/e^2$ value of the peak intensity. The output beam spot size ($2\omega_0$) during mode-locked operation along the x-direction was measured to be 1.739 ± 0.001 mm and along the y direction 1.693 ± 0.001 mm, as shown in figure 2.

Femtosecond pulse duration measurement

The temporal profile of the laser pulses was measured at the laser exit as well as at the microscope objective focus, upon travelling through the optics of the Gaussian transfection setup. The first set of measurements near the laser exit was obtained using a

commercially available interferometric autocorrelator (Timewarp, E750) which consisted of an optical head and a control unit.

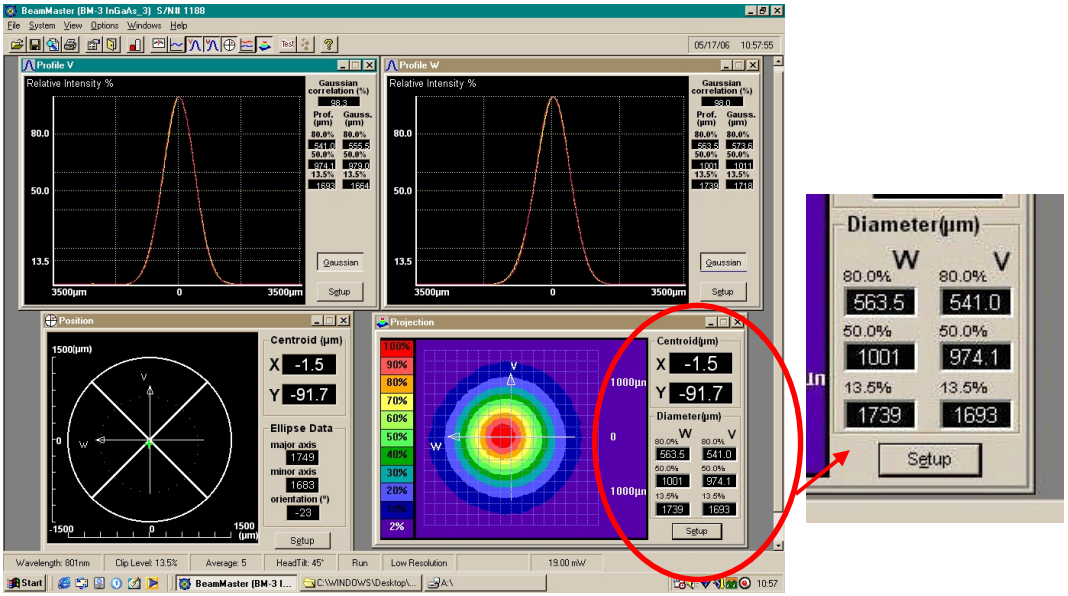

Figure 2: Beam profiler images of the laser intensity distribution along the x and y direction, perpendicular to the direction of propagation, as measured near the laser exit. The $1/e^2$ diameter (which corresponds to 13.5% of the peak intensity I_0) of the circular beam spot was measured to be 1.739 ± 0.001mm along the x and 1.693 ± 0.001mm along the y direction. For purposes of clarity, the bottom right part of the image is enlarged and displays the time averaged beam spot size in the x and y transverse directions.

The pulse duration at the focal plane of the microscope objective was difficult to be measured using the above method due to the highly divergent nature of the beam at the objective focal plane. For this purpose, a home built intensity autocorrelator was assembled.

The basic operating principle behind the home-built intensity autocorrelator as well as the

Timewarp autocorrelator, as shown in figure 3(a), is based on a Michelson interferometer. The interferometer consisted of a beam splitter, two mirrors M_1 and M_2, one movable and one static, a SHG crystal, a filter and a photomultiplier tube (PMT). The movable mirror was mounted on a loudspeaker that vibrates at a frequency approximately 18 Hz. The beam splitter separated the incoming pulse train into two replicas that subsequently travelled down a separate arm of the interferometer. Upon reflection off the mirrors the two pulse trains returned to the beam splitter and recombined. A focusing lens (f=100 mm) was used to focus the two beams on the SHG (KDP) crystal. The second harmonic signal was obtained upon spatial overlap of the two beams on the SHG crystal and was detected by the PMT. When the loudspeaker was in operation, the movable mirror introduced a relative path difference between the two pulse trains, resulting in a difference in the arrival time of the pulses at the SHG crystal. Full spatial overlap (zero delay) of the pulses on the SHG crystal would produce maximum signal on the detector. When the delay was increased, the pulses did not fully overlap on the crystal, therefore the frequency doubled signal was weaker. The resulting SHG intensity distribution (intensity autocorrelation) detected by the detector as a function of the delay, provided information about the duration of the laser pulses for a known pulse shape i.e. Gaussian or sech^2 shaped pulses [6-8]. The pulse duration at the laser exit and the sample plane was determined as a function of the laser wavelength across the Ti: Sapphire spectrum. For this purpose the laser was wavelength tuned and the pulse duration versus wavelength was obtained using the above mentioned autocorrelation methods.

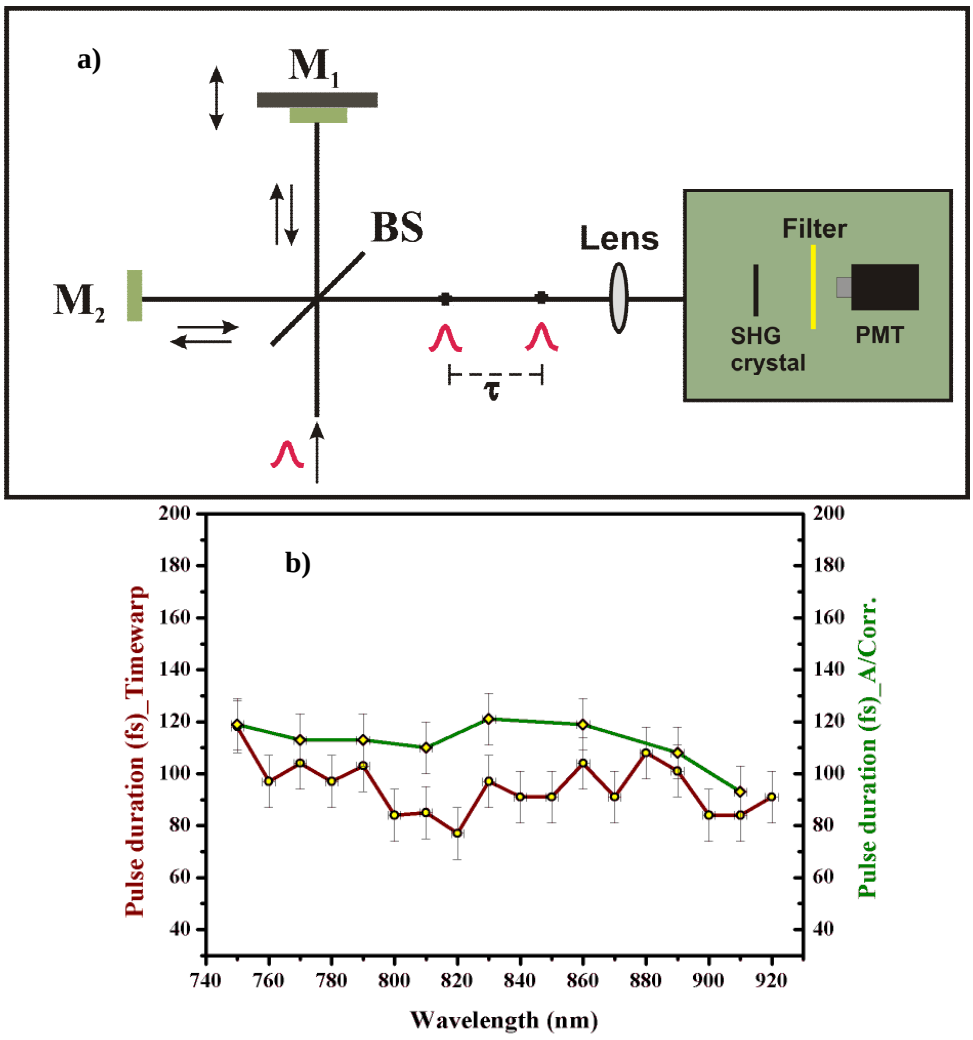

Figure 3: (a) Intensity autocorrelation for the measurement of ultra-short pulses generated by a Ti: Sapphire laser. A beam splitter (BS) separates the incident beam in two beams that propagate along the two arms of the interferometer. The mirrors M_1 and M_2 reflect the two pulse replicas back to the BS where they recombine. By varying the relative delay between the two pulse copies, the pulses arrive at the photomultiplier tube (PMT) with a delay τ with respect to each other, then they are spatially overlapped on the KDP crystal, giving rise to SHG signal with intensity that depends on the delay τ. (b) Pulse duration near the laser exit measured using the Timewarp (red bottom graph) and at the objective focus of the photoporation setup using the intensity autocorrelator (green top graph). The pulse duration remains constant (within a 10% error) across the laser spectrum due to the intra-cavity dispersion compensation scheme; however the duration of the pulses has increased upon traversing the photoporation optics and this is so at each wavelength.

In the case of the home-built autocorrelator, the setup was slightly varied from what is shown in figure 3(a). In this case, upon recombination on the BS, the two pulse replicas travelled through the photoporation setup, instead of being sent directly to the PMT detector. This was achieved by introducing a flip mirror between the BS and the focusing lens in order to redirect the beam towards the photoporation optics. Upon exit from the microscope objective, the beam focus was delivered on the SHG crystal and the autocorrelation signal was obtained. A simpler and more accurate alternative for the measurement of the pulse duration at the sample plane is the dual-objective method. In this case, the measurement is performed independently from the photoporation setup. The focusing objective lens is temporarily removed from the setup and is mounted horizontally along the optical bench following the magnifying telescope. The objective is illuminated by the expanded beam and provides a focused laser spot. The beam is subsequently recollimated by an identical objective lens mounted also horizontally, with its front lens facing the front lens of the focusing objective. The collimated laser beam is then directed into the TIMEWARP autocorrelator where the pulse duration can be measured. Through simple calculations, the contribution of the second collimating objective lens to the pulse temporal broadening can be excluded. This method can provide greater flexibility and ease in performing pulse duration measurements without the need for home built interferometric autocorrelation systems. In either case

Figure 3 (b) shows the estimated pulse duration of the pulses at the laser exit, using the Timewarp and at the microscope objective focal plane, using the home-built intensity autocorrelator. Using both the Timewarp and the home-built autocorrelator, I found that

the pulse duration varied slightly with wavelength. Due to the self phase modulation (SPM) within the Ti: Sapphire crystal and the positive group velocity dispersion (GVD) from the many dispersive materials inside the cavity (e.g. beam splitters, birefringent filters for wavelength tuning), temporal reshaping of the wave packet spectrum occurs. The blue components are retarded with respect to the red within the pulse therefore a systematic variation of phase with wavelength occurs. In order to compensate for the chirped pulse output, a compensation scheme is introduced inside the cavity comprising of a prism pair that introduces negative GVD. A more detailed description of the operation principle of prism pairs for dispersion compensation is presented in chapter 7. A birefringent filter is also present and its rotation results in the tuning of the laser's central wavelength. As the wavelength changes, the angle of refraction inside the first prism changes, and finds the second prism at a different location. Depending on the wavelength (e.g. red), the beam will travel through a different amount of prism glass (greater amount of glass) increasing the negative GVD. In order to maintain the same pulse width through the wavelength tuning, the prism should be translated accordingly in response to any change in wavelength. This was done during the experiments, so in theory no change with wavelength was anticipated. As far as the cavity adjustment is concerned, small systematic errors associated with the prism translation might have contributed to the pulse duration fluctuating across the spectrum. Other potential sources of the observed fluctuations, particularly pronounced when I used the home-built system, could be the random and experimental errors associated with the apparatus itself (i.e. actuators, alignment), as well as reading errors that have been taken into account.

The laser pulses, upon traveling through the photoporation optics undergo a small amount

of temporal stretching, which results in an approximately 10-15 fs increase in pulse duration at 790 nm. At pulse durations ranging from 100 fs and above, GVD is not as significant as it is at lower pulse durations particularly below 30 fs. The wavelength measurement was performed using a spectrum analyzer (IST-REES) and an oscilloscope with an associated systematic error of ± 2 nm.

Error analysis in the form of combination of independent errors, involving systematic, random and calculation errors, was applied for the each pulse duration measurement. Assuming that f is a function of x, y and z, each of which associated with independent errors s_x, s_y and s_z respectively, then the general formula that gives the error s_f for the function f (here the error in the pulse duration calculation) is:

$$s_f = \left(s_x{}^2 \left(\frac{\partial f}{\partial_x} \right)^2 + s_y{}^2 \left(\frac{\partial f}{\partial_y} \right)^2 + s_z{}^2 \left(\frac{\partial f}{\partial_z} \right)^2 \right)^{\frac{1}{2}} \qquad (3.8)$$

All the cell transfection experiments were performed at 790 nm, with pulse duration at laser exit equal to 100 fs and at the sample plane 113 fs, assuming sech^2 shaped pulses. By assuming Gaussian shaped pulses the pulse duration at 790 nm was estimated to be to 123 fs. For our application such variation in the pulse duration can be considered insignificant.

The optical setup used for Gaussian beam photoporation and transfection of CHO cells is detailed in the section that follows along with the sample preparation protocol for photoporation.

3.2.2 Experimental setup

The optical setup used for Gaussian beam photoporation and transfection is shown in figure 4. A Ti: Sapphire laser beam was directed through an electronic shutter (Newport, 845HP-02) which allows on and off control of the laser beam with a response rise time of less than 3 ms. The beam was subsequently incident on a HWP (at 790 nm) and a PBS which controlled the laser power delivered on the sample by changing the polarization of the incident laser beam. The beam of orthogonal polarization was discarded by the PBS onto a beam stop. A periscope consisting of two dielectric mirrors M_1 and M_2 with coatings to maximize reflection in NIR region, directed the laser beam through a x4 magnifying telescope, consisting of a two plano-convex lenses of focal lengths $F_1 = 50$ mm and $F_2 = 200$ mm respectively. The magnified beam slightly overfilled the 5 mm in diameter circular back aperture of the microscope objective (NA=0.85, x60, Newport) and was focused down to a small area of $(1/e^2)$ of diameter $1.8 \pm 0.3 \mu m$. The estimated confocal parameter was $6.4 \pm 0.81 \mu m$.

The diameter of the focused beam was measured using the direct camera technique which involves direct illumination of the CCD camera. The image of the focused spot was captured and processed using the IMAQVision program (National Instruments).

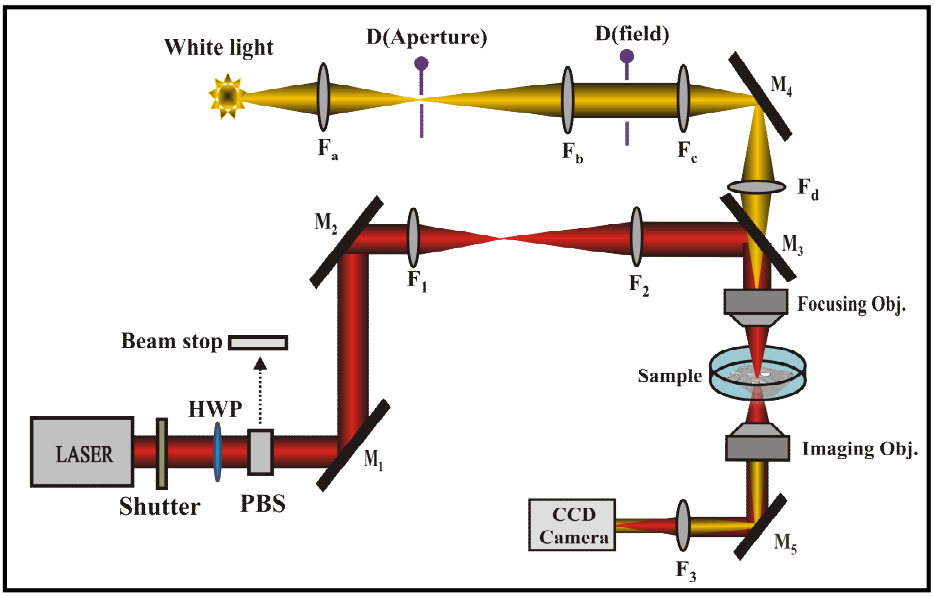

Figure 4: Optical setup for transfection of CHO cells. The laser beam emitted by a Ti: sapphire laser was directed through a set of two mirrors, M_1 and M_2 into a magnifying x4 telescope consisting of two planoconvex lenses F_1=50 mm and F_2=200 mm, prior illuminating a (NA=0.85, X60, Newport) microscope objective. A shutter was also placed in the beam path to control the duration of the laser dose delivered on the cell sample, whereas the combination of a HWP (at 790 nm) and a PBS adjusted the laser power. A beam stop was used to block the beam of orthogonal polarisation to the one delivered on the cells. The mirrors M_1 to M_3 were dielectric as opposed to M_4 and M_5 that were silver coated mirrors. The first part of the illumination path comprised of a fibre optic white light source and an F_a=35 mm lens that imaged the beam onto the aperture diaphragm. A telescope (F_b=50 mm and F_c=100 mm) was positioned behind the aperture diaphragm and relayed the filament onto the M_4 mirror. A field aperture controlled the field of view on the sample. The lens F_d=100 mm imaged the source filament at the back aperture of the objective. For the purposes of this experiment, the cell monolayer was bathed in plasmid DNA solution encoding for the DS-Red protein and is subsequently imaged through a long working distance objective and a CCD camera. Each targeted CHO cell was irradiated with three laser doses, each of 40 ms duration.

This approach proved to be particularly inaccurate as it is associated with rather large errors i.e. experimental (related to saturation degree of the beam spot) and systematic (related to the image processing i.e. intensity line profile of the beam spot and estimation of the beam waist) errors. After the completion of the experiments, I resorted to alternative, more accurate methods of measuring and estimating the beam waist such as the knife edge technique which is the operating principle of the laser beam profiler. The pulse energy at the objective front focal plane was estimated to be 0.875 ± 0.025 nJ with an associated pulse peak power 7.7 ± 0.09 KW. The irradiance delivered upon the cell membrane was estimated to be $(0.3\pm0.2)x10^{12}$ J/cm^2. Koehler illumination was setup to provide uniform specimen illumination.

In the context of an optical setup as the one shown in figure 4, Koehler illumination requires imaging the filament of the white light source at the back aperture of the focusing objective lens. In its simplest form, Koehler illumination for optical transfection can be achieved by simply using a white light source and an imaging lens in conjunction with the focusing objective lens. Herein, a series of lenses have been used here, in combination with two diaphragms named the aperture and the field diaphragms. More specifically, a lens of focal length F_a =35 mm was used to image the filament of the fibre optics white light source onto the aperture diaphragm D (aperture). The latter provided adjustment of the NA the illumination and obstructed any out of focus rays. A telescope consisting of two lenses of focal length F_b =50 mm and F_C =100 mm was placed appropriately behind the D (aperture) and relayed the filament image on the M_4 mirror. A field diaphragm D (field) was positioned at the afocal plane of the telescope which

controlled the field of view at the sample stage. A final focusing lens of focal length F_d =100 mm imaged the white light filament at the back aperture of the focusing objective. A long working distance objective (NA=0.7, x100, Mitutoyo) was used for the imaging of the cell specimen. A tube lens of 100 mm focal length was also positioned behind the microscope objective and focuses the collected ray bundle onto the sensor of a CCD. The mirrors M_4 and M_5 were silver coated. Figure 5 shows part of the optical setup used for Gaussian photoporation experiments.

3.2.3 Sample preparation protocol

For the cell transfection experiments, CHO cells were grown to sub-confluence in 30 mm diameter glass-bottomed culture dishes (usable area 23 mm; World Precision Instruments, Stevenage, UK) in 2 ml of Modified Eagles Medium (MEM) fortified with 10% fetal calf serum (FCS) (Invitrogen, Paisley, UK) and antibiotics (Sigma, UK) comprising 18 units/ml of penicillin, 18 μg/ml of streptomycin, and also 1.8 mM of L-Glutamine, in a humidified atmosphere of 5% CO2 / 95% air at 37 ºC. The typical culture dishes used for the culture of CHO cells are shown in figure 6.

The cell monolayer was washed twice with OptiMEM (Invitrogen), and exposed to a 40 μl solution of OptiMEM containing 1.2. μg/μl mitoDSRed plasmid which encodes a mitochondrially targeted *Discoideum* red fluorescent protein (BD Biosciences, UK).

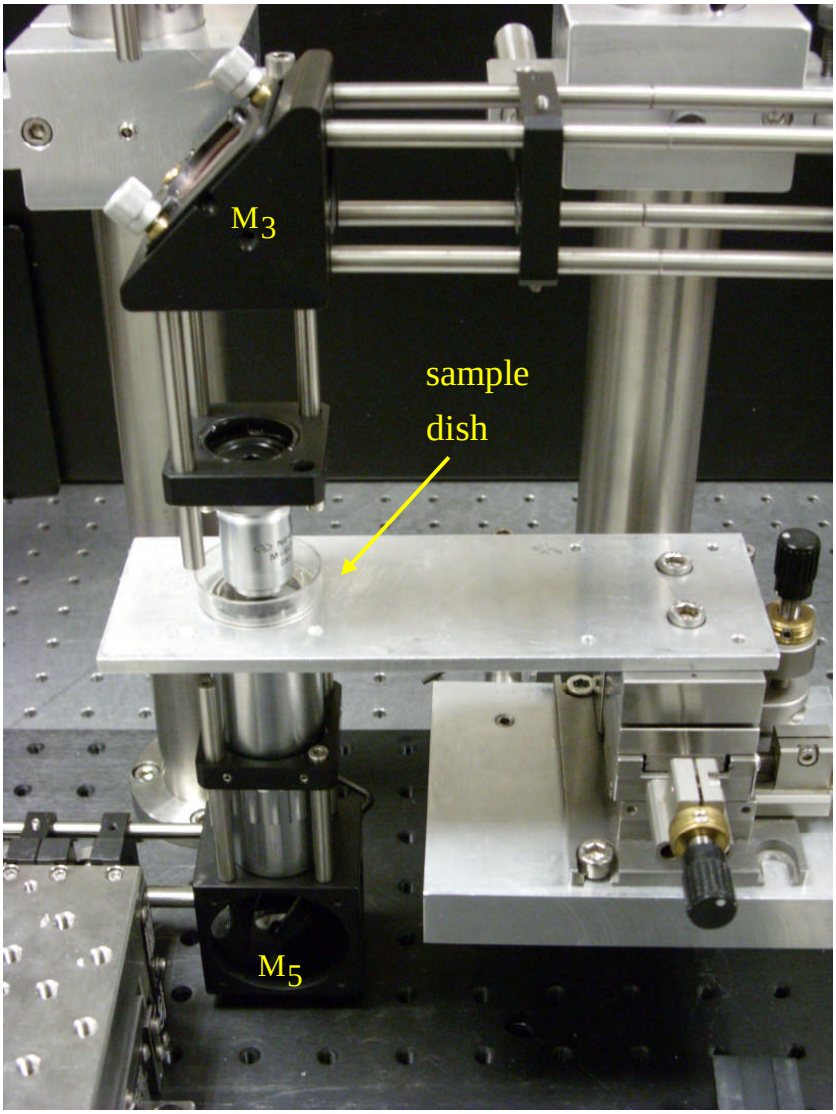

Figure 5: Photoporation setup. The incoming laser beam is reflected off the M_3 mirror and subsequently illuminates the back aperture of the microscope objective. The beam is then focused to a spot of width 1.8 μm. The culture dish, containing the adhered CHO cells, is located directly below the objective. During photoporation, the laser focus is aligned with respected to the cellular membrane and laser doses, each of 40 ms duration, are delivered. The cells and the laser beam are imaged through the imaging objective which collects and delivers the transmitted light on M_5 mirror which directs the light through a tube lens on a CCD camera.

A 23 mm diameter type-0 (90 μm thickness) coverslip (BDH, Poole, UK) was then floated on top of this 40 μl solution.

A dark circular area was then drawn on the reverse side of the glass-bottomed culture dish, to indicate the area that would enclose the photoporated cells. Cells that were grown in close proximity to the edges of the dish well were not targeted during photoporation. This way I could eliminate the possibility of accidental physical contact with the cells during adding and removing the coverslip that could potentially compromise the cell membrane and lead to undesired transfection.

For the purposes of the precursor photoporation studies of CHO cells using the Trypan Blue stain, the sample dish was bathed in 40 μl solution comprising 50% OPTI-MEM and 50% Trypan Blue solution (0.1% final concentration).

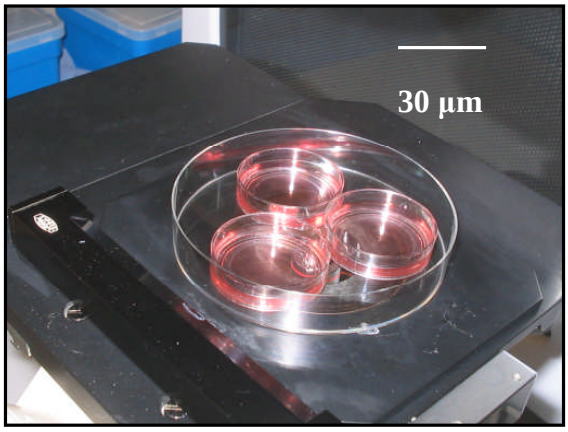

Figure 6: The cell cultured dishes which were used to grow CHO cells for the photoporation experiments. During photoporation a coverslip was floated on top of the 40 μl of plasmid DNA solution, encoding for the DS-Red protein, which surrounded the cell monolayer.

A circular type-0 coverslip was floated on top of the Trypan Blue solution that

surrounded the cell monolayer. The area of interest was located within the dark circular line drawn at the reverse side of the culture dish.

The section that follows details the experimental findings of fs Gaussian photoporation of Chinese hamster ovary (CHO) cells using Trypan Blue and DS-RED plasmid DNA. The transfection efficiency was monitored versus the axial position of the cell membrane along the propagation direction of the Gaussian beam.

3.2.4 Experimental results

3.2.4.1 Trypan Blue phototranslocation of CHO cells

In early photoporation studies [9], a way to ascertain and confirm whether photoporation of cells acts towards membrane perforation, was for CHO cells to be photoporated in the presence of the normally membrane impermeable and toxic dye, Trypan Blue. Upon laser irradiation, at power levels normally greater than 100 mW, membrane perforation took place, resulting in the diffusion of Trypan Blue through the open pore. The presence of Trypan Blue inside the cell cytoplasm leads to blue staining of the cell, around the site of irradiation, called photo-translocation, as shown in figure 7. The number of Trypan Blue macromolecules that diffuse through the laser-induced pore and hence the intensity of the local staining, depends on the power at the laser focus. Live cells with uncompromised and healthy membranes are excluded from staining.

During the Gaussian photoporation studies described in the present chapter, Trypan Blue

was only used for preliminary studies of membrane perforation. At power levels above 100 mW, Trypan Blue translocation was clearly observed 30 sec after laser irradiation; however no DS-Red expression occurred at the same power level. On the other hand, at power levels below 100 mW, no Trypan Blue staining was visibly evident, although at 70 mW at focus, transient transfection of DS-Red was obtained. The lack of blue staining of the irradiated cells at powers below 100 mW could be attributed to the small size of the induced pore, which prevented the Trypan Blue macromolecules to enter, or allowed only a small number of macromolecules to enter resulting in very low staining intensity that was impossible to be viewed under the home-built bright field illumination. In addition, lack of staining at powers below 100mW, may partly be attributed to unsuccessful membrane perforation as a result of laser irradiation.

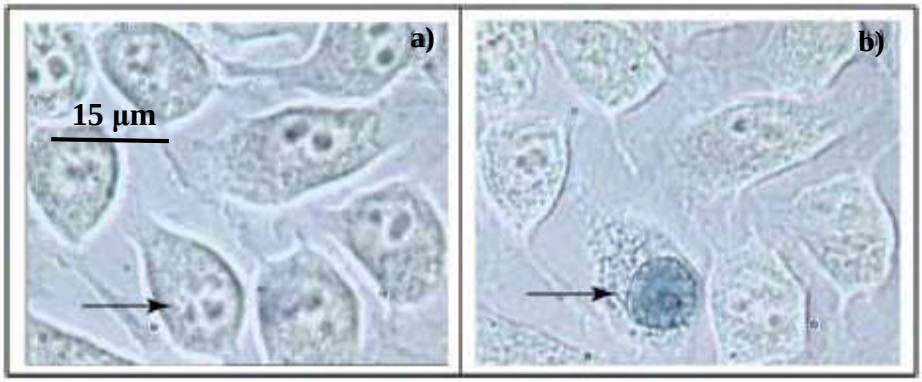

Figure 7: (a) CHO cell (indicated) photoporated in the presence of the normally membrane impermeable dye, Trypan Blue. (b) 30 second later, photoporation has lead to cell membrane perforation, allowing the external substance to enter the cell cytoplasm by phototranslocation.

It was concluded that at low powers (~70 mW) at the laser focus, the induced membrane pore is wide enough to allow a number of plasmid DNA molecules to enter the cytoplasm but not wide enough to allow sufficient number of Trypan Blue molecules to enter the

cell and cause any visible staining. Due to the false positive results collected at low power levels using Trypan Blue, I made no further use of this particular dye in later experiments.

An alternative option to Trypan Blue is PI which is a nucleic acid stain with excitation peak at wavelength 535 nm and emission peak at 617 nm. As with Trypan Blue, PI is membrane impermeable and is excluded from viable cells. In contrast to Trypan Blue that locally stains the cell interior around the targeted area, PI binds to DNA which causes the nucleus of the host cell to fluoresce red. In order to assess the optimum laser parameters for photoporation, the cell sample is bathed in PI and photoporation takes place. Upon successful membrane perforation, PI is internalized into the cytoplasm, binds to the DNA and red fluorescence is observed. This is an indication of successful photoporation. If PI is used in combination with Calcein AM stain, cell viability can also be assessed. Calcein AM, with excitation and emission peaks at 494 nm and 517 nm respectively, is membrane permeable and can be used to determine cell viability, as it is well retained in living cells and exhibits intense green fluorescence within the cytoplasm. If the delivered laser dose on a cell during photoporation is lethal, the irradiated cell will cease fluorescing green which will be an indication of operating above the irradiance threshold for safe photoporation.

3.2.4.2 Optical transfection of CHO cells using DS-Red plasmid DNA

Laser assisted transfection of cells is a complex process that consists of two main steps: photoporation and transfection. Photoporation is the laser-induced membrane disruption

that enables the insertion of the surrounding plasmid DNA into the cell cytoplasm. Upon successful photoporation, the cell survives the laser-treatment and the internal mechanism of plasmid DNA processing begins. As discussed already, this involves transportation of the internalized nucleic acids across the cytoplasm to the nucleus where the transcription can begin, with the ultimate goal the correct translation of the gene into the corresponding protein [10, 11]. When the second step is completed successfully, the cell becomes transfected [12-15].

Figure 8(a) shows photoporation of CHO cells in the presence of plasmid DNA using a tightly focused Gaussian beam [9, 16]. The cells were positioned at the laser beam focus by manipulating an XYZ translation stage upon which the sample dish was placed.

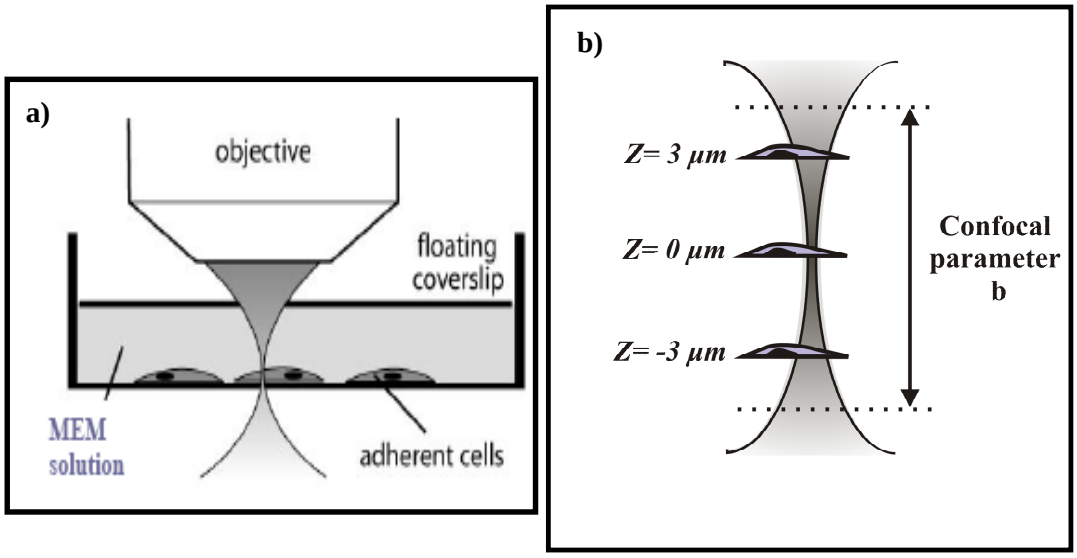

Figure 8: (a) Photoporation of CHO cells using a tightly focused Gaussian beam. The CHO cells were adhered on a glass bottomed culture dish in the presence of plasmid DNA encoding for DSRed fluorescent protein. Each cell was irradiated with three laser doses, each of 40 ms duration, upon which a self-healing pore was created on cell membrane that allowed the plasmid DNA to enter the cell cytoplasm of the cell. (b) The transfection efficiency was monitored as a function of position z along the beam propagation direction.

The mean power sent to the Gaussian optical system was 100 mW. The power transmission of the optical system was such that the sample was laser treated at power levels of 70 mW.

The number and duration of laser doses was experimentally determined for a given irradiance at the laser focus. I found that using more than one laser dose, whilst slightly adjusting the axial position of the cell sample with respect to the focus, increased the possibility of correct alignment of the focus on the cell membrane. During laser irradiation, there was no visual evidence of large scale bubble formation which is a result of accumulative photothermal effects that are known to occur on the cell membrane above the breakdown optical threshold [17]. The occurrence of such visible effects was a direct indication of exceeding the power threshold for safe photoporation.

The transfection efficiency was monitored as a function of the location of the cell membrane along the (axial) direction of beam propagation, as shown in figure 8(b). This study allowed us to ascertain the axial range over which strong enough focusing could be achieved for successful multiphoton membrane perforation. The total number of photoporated cells per culture dish was fifty and the total number of culture dishes treated per axial position varied between five and six. Considering that the confocal parameter of the focused Gaussian beam was approximately 6.4 μm, the transfection rate was monitored at nine different axial positions: at the laser focus (z=0), at 3 μm above and below the laser focus ($z=\pm 3\mu m$), at 6 μm above and below the laser focus ($z=\pm 6\mu m$) and at 10 μm above and below the laser focus ($z=\pm 10$ μm). The positioning of the sample stage was adjusted with respect to the focus using a motorized stage with a 0.5

μm step.

Upon laser treatment, the cell specimen was returned to the cell culture lab where the coverslip was removed. The cell monolayer was subsequently bathed in MEM fortified with 10% fetal calf serum (FCS) and antibiotics as described above, and the culture dish was returned to the incubator. 48 h after treatment, cells were viewed by fluorescent microscopy for red fluorescent protein (RFP) expression, allowing for the transfection efficiency to be quantified. Images were captured by a CCD camera (Pulnix) and a personal computer equipped with a frame-grabber board.

The transfection efficiency was calculated by dividing the number of cells expressing RFP at 48h by the total number of cells that were treated by the laser in a particular region of interest at 0 h. Cells destroyed or irreversibly damaged as a result of the laser action were included in the data in order to provide a real and representative figure for the transfection efficiency of the fs optical transfection technique. In this case, the transfection efficiency coincided with cell viability, as no dead fluorescent cells were observed. Fluorescent microscopy showed that transient RFP expression had been achieved and that cells expressing RFP are viable and display normal morphology, thereby confirming that successful optical transfection has occurred.

In order to ascertain the possibility of spontaneous transfection that may occur when cells are in the presence of plasmid DNA, control sample dishes were also prepared. Each photoporated dish was accompanied by a control dish, where cells were exposed to the standard protocol of culture and preparation i.e. plasmid DNA concentration and coverslip, however there was no exposure to laser irradiation. The average number of

spontaneously transfected cells in the control dishes varied between 0 and five, and this was taken into consideration when monitoring transfection efficiency.

As evident from figures 8(a)-(b), the surface morphology of a cell is not a uniform, flat area of a certain thickness. Instead, the edges of a cell are particularly thin (1 to 2 μm) as opposed to the more central parts of the cell where the thickness may increase to several microns. When cells are adhered on the culture dish surface, due to the curved cell morphology, the membrane resides at a different plane to the dish bottom. In addition, due to the low refractive index difference between the cells and their liquid environment, it becomes particularly difficult to determine the exact location of the cell membrane. This imposes particular difficulty in aligning the laser focus with respect to the cell membrane when performing photoporation. Significant mismatching may jeopardize the efficiency of the technique, considering the multiphoton nature of the process. Figure 9 shows the transfection efficiency of CHO cells, photoporated using a Gaussian beam, as a function of the axial position z. As evident from figure 9, when the cell membrane is positioned at the laser beam waist (at z=0), approximately 50% transfection efficiency can be achieved due to the high energy confinement at the laser focus. However, when the cell membrane is positioned at distance 3 μm away from the focus, which approximately coincides to the beam's Rayleigh range, the transfection efficiency rapidly drops just below 20%, in response to the decrease in the beam's peak intensity at that axial location.

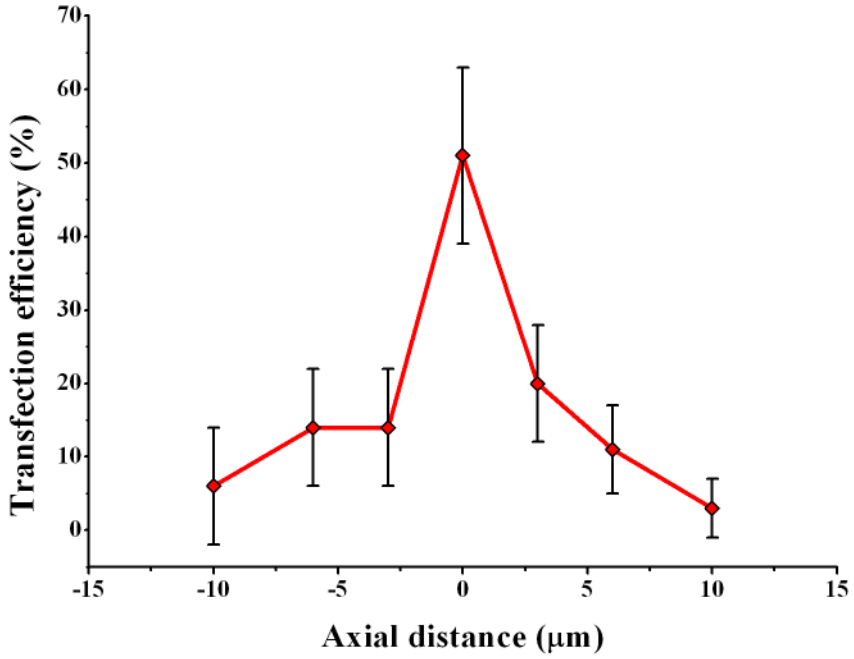

Figure 9: Transfection efficiency as a function of the position of cell membrane along the axial direction of the beam propagation. At the laser beam focus there is maximum energy confinement resulting to 50% transfection efficiency. Just 3 μm away from the focus, the transfection rate drops significantly to less than 20 % and as we move further away from the focus no significant transfection occurs.

A further decrease in the transfection efficiency is evident when the cell membrane is displaced by 6 μm (approximately equal to the confocal parameter of the beam) from the focal region. At an axial distance 10 μm away from the focus the transfection rate becomes negligible. Each data point in the graph corresponds to an average of seven photoporated sample dishes. Considering that 50 cells were treated per sample dish, this gave an average of 350 cells per data point. Error analysis was performed in order to obtain a value for the error involved in the calculation of the average transfection efficiency per data point. Firstly, the mean value of the transfection efficiency was obtained at each axial distance and then the calculation of the standard error of the

resulting mean value was calculated. The error bars shown in figure 9, correspond to the standard deviation of the mean value of the transfection efficiency at each axial distance.

It becomes evident that the multiphoton nature of the photoporation process imposes strict requirements for careful and precise positioning of the cell membrane with respect to the laser focus due to the high photon flux required to initiate multiphoton ionization at the target area. This results in demanding alignment when moving from one cell to the next, in order to precisely locate the cell membrane and successfully photoporate. Due to the stringent requirements of alignment, photoporation becomes a rather tedious technique to perform that requires considerable experimental expertise. This has lead to the investigation of alternative beam shapes such as the use of “non-diffracting” beams such as the BBs that exhibit an elongated depth of focus and hence introducing considerably fewer alignment limitations. This approach will be explored analytically in chapter 4 that follows.

The next step in my experimental work on photoporation was the investigation of the topography of the laser irradiated cells as a function of the power on the laser focus. This work is detailed in the section that follows.

3.2.5 Investigation of the topography of photoporated cells using Atomic Force Microscopy (AFM)

One step towards elucidating the effect of laser irradiation on the cellular membrane is to monitor the topography of the cell membrane upon laser treatment. By identifying the

size and shape of the laser-induced membrane pore as a function of the power at focus, one ultimately could obtain a useful insight of the cell viability upon laser treatment and ascertain the optimum laser parameters for safe transfection. Atomic force microscopy (AFM) was used to investigate the size of the pore induced upon laser irradiation on the membrane of CHO cells.

3.2.5.1 Experimental process

Sample fixation protocol

The cell monolayer was grown on a rectangular coverslip (type-1, of 125 μm thickness) in 5 ml of MEM fortified with FCS and antibiotics, as described in previous section. Prior to the experiment, the MEM media were removed and 40 ml of OPTI-MEM were inserted on the surface of the rectangular coverslip upon which a type-0 circular coverslip was suspended. The fixative solution consisted of formaldehyde (of 40% concentration) and distilled water in 1:10 ratio. The solution was aliquoted in quantities of 5ml and subsequently stored for roughly 2 hours at -20°. It was then thawed for 10-15 minutes at 37° in a hot bath and finally placed in the fridge at 4° temperature prior to being transported to the laser lab along with the cell sample.

Experimental setup

For the purposes of this study, the optical setup used was the one shown in figure 4. Slight adjustments in the optical setup were performed in order to take into account the fact that the microscope objective was of finite tube length. The optical setup was re-

arranged by inserting a plano-convex lens of 160 mm focal length after the x 4 expanding telescope. This lens was positioned at a distance 320 mm from the back aperture of the objective resulting in a divergent bundle of rays reaching the back aperture of the focusing objective. In this case, best focusing performance was achieved when the incident rays where incident as a divergent bundle instead coming collimated. The $1/e^2$ diameter of the focused laser spot was estimated to be approximately 1.6 μm which is not significantly different from the estimated diameter 1.8 μm obtained when a collimated ray bundle was incident on this objective.

Each cell was exposed to a single laser dose of 40 ms duration at various power levels at the laser focus. Instantly, the formaldehyde solution was introduced into the cell culture dish, whilst the culture dish was still located on the XYZ translation stage. This way any morphological change on the cell membrane induced by the laser beam could be maintained and later revealed by the AFM scans. After photoporation, the sample was washed several times with distilled water in order to remove any residue of buffer crystals that could prohibit the scanning process and the coverslip was removed. The samples remained in distilled water and were subsequently dried out upon arrival at Dundee University where the AFM facilities were located.

3.2.5.2 Results and discussion

Figure 10 shows the topography of photoporated cells exposed to different power levels at the laser focus. When the cell was exposed to a single laser dose of 40 ms duration and power 100mW (figure 10 (a)), a small pore of 0.9 ± 0.1nm in diameter was formed on the

cell surface. The size of the pore is smaller than the FWHM diffraction limited spot size (1.1 μm) of the focused beam. The small size of the induced pore manifests the fact that fs laser pulses at irradiances well below the optical breakdown threshold produce very fine effects with a spatial extent below the diffraction limit at the operating wavelength.

At low enough irradiances, sub-diffraction limited resolution stems from the fact that the multiphoton nature of the interaction diminishes the affected volume into which the energy is deposited [17]. At power 150 mW at focus, the induced pore appears to be of circular shape with diameter $2.5 \pm 0.3 \mu m$. Some residue of cellular matter appears around the formed pore, potentially as a result of material displacement at the irradiation site. At power equal to 270 mW, a pore appears on the cell membrane with size of the order of several microns. Any further increase of the input power, at levels above 300 mW, has catastrophic effects on the cell, resulting in crater-shape deformation of the cellular membrane with clear signs of collateral damage. At power levels above 100 mW, there was visible evidence of bubble formation that scaled up with power, resulting in accumulating thermal effects at the irradiation site causing cell damage and necrosis.

When performing Gaussian photoporation using multiple laser doses, the laser focus is normally adjusted between exposures in order to increase the probability of correct alignment of the laser focus with respect to the membrane. In some occasions, this may result in successive laser doses being delivered at slightly different ($\pm 1 \mu m$) locations on the membrane, as evident from figure 11(a), where the cell was exposed to three laser doses at power of approximately 150 mW.

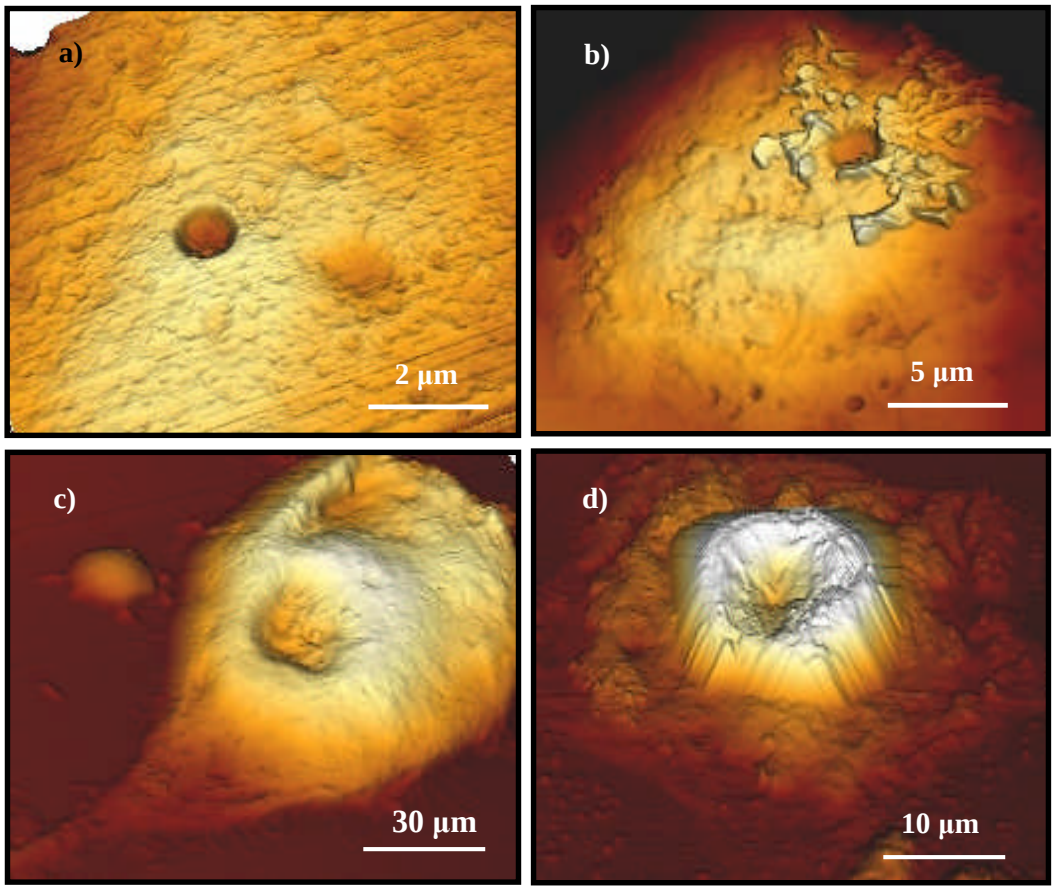

Figure 10: Topography of photoporated CHO cells using AFM and the resulting pore formation upon laser irradiation at (a) P=100 mW, (b) P=150 mW, (c) P=270 mW, (d) P=360 mW. The induced pore shape appears circular at low enough irradiances as shown in (a) and (b), while at power levels significantly exceeding the safe photoporation threshold, catastrophic effects occur as indicated in (c) and (d).

For the purposes of this experiment, a single laser dose of 40 ms duration was delivered on each cell in order to obtain a more accurate view of the shape and size of the irradiated area.

When the power was reduced below 100 mW, there was no visual evidence of large scale bubble formation. This indicates operation below the threshold for safe photoporation.

Using a single laser dose made it difficult to ascertain successful alignment of the laser focus with respect to the cell membrane, hence several runs yielded no membrane deformation.

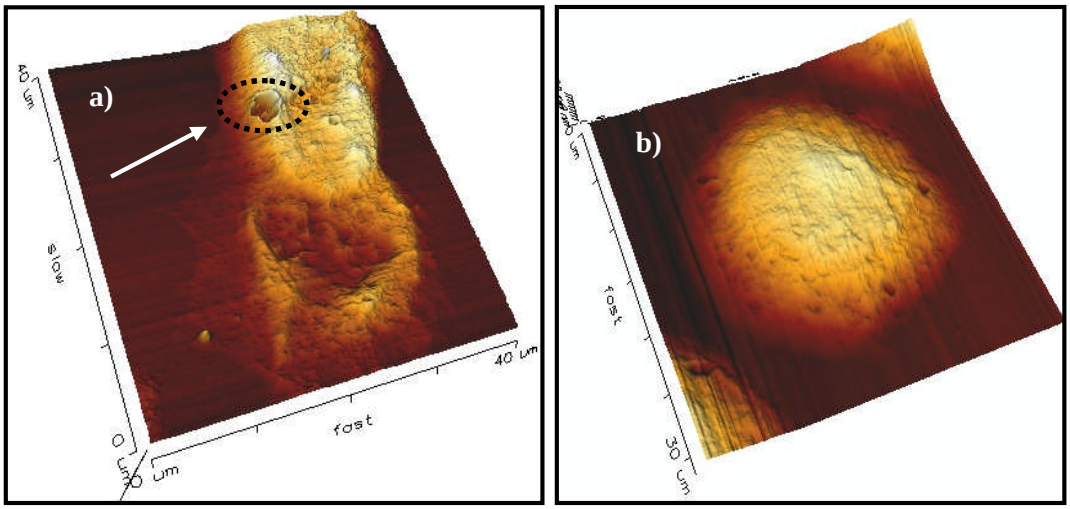

Figure 11: (a) Topography of a photoporated CHO cell exposed to three laser doses, each of 40 ms duration, at input power 150 mW at the laser focus. It is evident that the three laser doses were delivered in adjacent sites due to the routine micron-scale adjustments of the axial position of the cell with respect to the laser focus. (b) The topography of a fixed cell that was used as a control sample, in the absence of laser exposure. Tiny pores around the edges of the cell become apparent in addition to a characteristic rough, uneven overall surface morphology as a result of the fixation treatment upon laser irradiation.

In addition, fixative substances such as formaldehyde, when added in the sample, cause unavoidable nano-scale defects that could be easily confused with pore formation at irradiances well below the threshold for safe photoporation. Figure 11(b) shows the topography of a CHO cell that was not photoporated but was nevertheless scanned to provide a control. Small circular features appear around the edges of the cell that are due to the fixative solution introduced into the cell specimen.

It is therefore essential during the AFM scans to be able to identify the irradiation sites on the membrane as well as the location of the irradiated cell inside the area of interest. For this reason, one to two cells of well distinguished features were irradiated per dish as well as a map of the area of interest was drawn.

This set of experiments has proved to be a useful aid to the way we view the cell photoporation process. Further investigation of the pore size with respect to the time that follows the delivery of the laser dose at t=0, could lead to very useful information regarding the pore healing process and help us identify the optimum laser parameters for reversible membrane perforation. Further studies of pore formation as a function of pulse duration could also yield important insight into the spatial resolution of the irradiated site especially when using pulse durations below 30 fs.

This set of experiments was performed in collaboration with Dr Paul Prentice and Dr Paul Campbell, based at the department of Division of Electronic Engineering and Physics of the University of Dundee. The experimental procedure and cell preparation were performed at the university of St Andrews by myself in the presence of Dr P. Prentice. The cell samples were transferred to Dundee by Dr P. Prentice where they were subsequently scanned using the AFM.

3.3 Conclusion

In this chapter, I detailed photoporation and optical transfection of CHO cells using a tightly focused Gaussian beam. Femtosecond photoporation is a powerful technique for modifying the genetic profile of cells at will. This is due to its non-invasive, highly

selective character that allows us to target a single or a group of cells randomly located within a sea of other cells. Due to the short duration of fs pulses, photoporation offers ultra-precise energy deposition at the target area, resulting in ultra-fine pore formation on the cellular membrane without the occurrence of collateral damage.

I have presented an extensive study of fs photoporation and transfection of CHO cells whereby the transfection rate of CHO cells was investigated as a function of the position of the cells along the axial direction of the beam propagation. When the cell membrane was positioned at the laser focus, one out of two cells were successfully transfected whereas when the cells were axially displaced from the focus the transfection rate significantly dropped and became negligible at axial displacements beyond the beam's Rayleigh range. From these results, it became evident that Gaussian transfection introduces strict requirements in the positioning of the laser focus on the cell membrane due to the multiphoton nature of the pore creation. The highly divergent nature of a Gaussian beam requires demanding alignment when moving manually from cell to cell during photoporation. This makes the technique tedious to perform and be adopted by life-scientists who more often than not have a preference towards automated, alignment free optical setups and microscopes.

For the purposes of these studies, plasmid DNA encoding for a red fluorescent protein, the DS-Red, was introduced in the solution surrounding the cell monolayer during laser irradiation. Successful internalization of the DS-Red plasmid was evident 48h upon laser treatment and identified by means of a fluorescent microscope. The transfected and viable cells exhibited red fluorescence within their mitochondrial area and appeared to

have normal and healthy morphology. Precursor photoporation studies were also performed, in order to ascertain the correct laser parameters (i.e. laser dose duration, power level at laser focus, number of laser doses, site of irradiation) leading to successful internalization of the plasmid DNA. For the purposes of these initial studies, the membrane impermeable stain Trypan Blue was implemented. Successful internalization of Trypan Blue, results in local blue staining within the cytoplasm, around the area of irradiation. The blue staining occurs within several seconds upon cell irradiation ultimately leading to cell necrosis due to its toxicity. Trypan Blue photoporation studies might have appeared helpful in early experimental stages; however they did not offer conclusive results as to the optimum laser parameters for photoporation. Alternative stains such as Propidium Iodine and Calcein AM will be used in the future for performing transfection efficiency and viability studies.

In order to elucidate the effect of the fs laser pulses on the cell membrane, the topography of the photoporated cells with respect to the laser power was also studied and presented using AFM. Upon laser irradiation, the cells were fixed in formaldehyde solution and were subsequently scanned using the AFM. At low power at the laser focus, close to the threshold for safe photoporation, an ultra-fine pore was formed on the membrane which appeared to be of circular shape with diameter just below 1 μm. This manifested the multiphoton character of the interaction, which resulted in a selective and ultra-confined energy deposition on the targeted area, significantly decreasing the possibility of collateral damage. However, when the power was increased above the threshold of safe membrane perforation, thermal effects in conjuction with multiphoton chemical effects came to play that resulted in greater pore diameters. At sufficiently high powers, the

membrane morphology showed strong signs of collateral damage ultimately leading to cell necrosis.

Femtosecond optical transfection of cells is a powerful technique that surpasses in various aspects many of the currently employed transfection techniques. The limitations introduced by the highly divergent nature of the Gaussian laser beam make the technique less popular due to the demanding alignment when moving from cell to cell within a cell sample. As detailed in the chapter that follows, such limitations can and have been overcome by means of a “non-diffracting” BB. As shall be explained, such laser beam possess an elongated depth of focus which permits longer axial mismatching in positioning of the laser focus on the cell membrane. This significantly improves the way the photoporation process is performed in terms of alignment and paves the way towards complete automation of the optical transfection.

References

[1] B. Saleh and M. Teich, "*Fundamentals of Photonics"*, 2nd ed. (2001), John Wiley & Sons,

[2] A. Siegman, " *Chapter 17: Physical properties of Gaussian beams"*, in *Lasers,* (1986), University Science Books, California, USA, p. 663.

[3] E. Hecht, "*Optics"*, 4th ed. (2002), Addison Wesley, New York

[4] V.N. Mahajan, "*Uniform versus Gaussian beams-A comparison of the effects of diffraction, obscuration, and aberrations,"* Journal of the Optical Society of America A **3**(4), p. 470, 1986.

[5] A. Diaspro, "*Confocal and Two-Photon Microscopy: Foundations, Applications and Advances",* 1st ed. (2002), John Wiley and Sons, New York

[6] H.A. Haus, et al., "*Structures for additive pulse mode locking,"* Journal of Optical Society of America B **8**(10), p. 2068, 1991.

[7] I. Cormack, "PhD thesis: Rapid techniques for ultrashort optical pulse characterisation", Supervisor: W. Sibbett, (2001), School of Physics & Astronomy, University of St Andrews

[8] A. Miller and D.T. Reid, " *Measuring ultrafast laser pulses",* in *Ultrafast Photonics,* (2004), Institute of Physics publishing, London, p. 59.

[9] D. Stevenson, et al., "*Femtosecond optical transfection of cells: viability and efficiency,"* Optics Express **14**(16), p. 7125, 2006.

[10] D. Lechardeur and G. Lukacs, "*Intracellular barriers to non-viral gene transfer,"* Current Gene Therapy **2**(2), p. 183, 2002.

[11] G.L. Lukacs, et al., "*Size-dependent DNA mobility in cytoplasm and nucleus,"* Journal of Biological Chemistry **275**(3), p. 1625, 2000.

[12] S. Kurata, et al., "*The Laser Method for Efficient Introduction of Foreign DNA into Cultured-Cells,"* Experimental Cell Research **162**(2), p. 372, 1986.

[13] V. Kohli, et al., "*Reversible permeabilization using high-intensity femtosecond laser pulses: Applications to biopreservation,"* Biotechnology and Bioengineering **92**(7), p. 889, 2005.

[14] S. Sagi, et al., "*Gene delivery into prostate cancer cells by holmium laser application,"* Prostate Cancer and Prostatic Diseases **6**, p. 127, 2003.

[15] H. He, et al., "*Targeted photoporation and transfection in human HepG2 cells by a fiber femtosecond laser at 1554 nm,"* Optics Letters **33**(24), p. 2961, 2008.

[16] U.K. Tirlapur and K. Konig, "*Cell biology - Targeted transfection by femtosecond laser,"* Nature **418**(6895), p. 290, 2002.

[17] A. Vogel, et al., "*Mechanisms of femtosecond laser nanosurgery of cells and tissues,"* Applied Physics B-Lasers and Optics **81**(8), p. 1015, 2005.

Chapter 4

Femtosecond cellular transfection using a “non-diffracting” light beam

Introduction

This chapter explores a different approach for performing optical transfection of CHO cells to the use of a focused Gaussian laser beam. Herein, I present photoporation and transfection of cells by means of a quasi-Bessel beam. The quasi-BB, with its characteristic “non-diffracting” profile during propagation, acts like an optical syringe that retains an elongated “non-spreading” bright line of light over long distances. Such a “non-spreading” light beam was generated using a conical lens called an axicon and was subsequently used to target CHO cells in the presence of plasmid DNA encoding for a mitochondrially targeted DS-Red fluorescent protein. The transfection efficiency (the number of red fluorescent cells over the total number of the targeted cells) was monitored as a function of the position of the cell membrane along the propagation direction of the beam.

This study revealed the available axial beam range over which successful transfection can be achieved. These results were compared with those for Gaussian beam photoporation. Such comparison highlighted the merits of a “non-spreading” beam for photoporation of cells by showing that the given quasi-BB gives us over 20 times the axial transfection length compared to the Gaussian beam of equivalent spot size. The use of a quasi-BB is

the first step towards “alignment-free” optical transfection as it significantly simplifies the delivery of the laser dose when moving from one cell to the next within the sample.

The last part of the chapter is a continuation of the above work as it describes the experimental steps towards automating the transfection process. This work involves using an axicon generated “point and click” quasi-BB for laser-assisted cell transfection. By means of an SLM, the position of the quasi-BB with respect to the cells was controlled in 3D. The SLM was LabView driven and interfaced with a computer mouse for ease of positioning the beam within the cell sample.

This chapter begins with an introduction on the propagation properties of the zeroth order BBs before detailing the experimental work and results on quasi-BB transfection of CHO cells.

4.1 Propagation properties of a Bessel beam

Diffraction is a phenomenon that is closely related to the wave nature of light. When light is partially obstructed or passes through an aperture or obstructive element, it will bend around the edges of this element due to diffraction. The concept of light “bending” implies the change in phase or/and amplitude of the propagating wavelets around the edges of the obstructive object. Diffraction is also apparent in the spreading of Gaussian beams as they propagate in space. As discussed in the introduction, in the context of photoporation, the rapid spreading of a tightly focused Gaussian beam results in strict requirements of positioning the laser focus on the cell membrane. The low refractive index difference between the intra-cellular and extra-cellular environment, makes the cell

membrane difficult to identify and therefore successfully target during Gaussian photoporation. A way to circumvent this problem was to implement a special type of light beam, the BB, which exhibits a degree of immunity to diffraction effects.

From a mathematical point of view, BBs are particular solutions to the time-independent Helmholtz wave equation in cylindrical coordinates[1, 2]. Such solutions can be described by the formula:

$$E(r,\phi,z) = A_0 \exp(i(k_z z \pm n\phi))J_n(k_r r),\ n = 0,\pm1,\pm2,\ldots \qquad (4.1)$$

where $E(r,\phi,z)$ is the electric field of the nth order BB, J_n is nth order Bessel function of the first kind, n is the order of the Bessel function and is an integer number, k_z and k_r are the longitudinal and radial wavevector components that obey the following relation:

$$k = \sqrt{(k_r)^2 + (k_z)^2} = \frac{2\pi}{\lambda} \qquad (4.2)$$

λ being the wavelength of the incident laser beam constituting the BB, r, ϕ and z are the radial, azimuthal and longitudinal components of the cylindrical coordinates and A_0 is a constant.

This thesis will be concerned with Bessel functions of the first kind and in particular of the zeroth order that describe “non-diffracting” BBs that exhibit a sharp peak intensity at their origin. Figure 1(a) shows a plot of the zeroth, first and second order Bessel functions of the first kind as a function of the Cartesian coordinate x. Bessel functions of

the first kind are finite in the origin (x=0), with the zeroth order displaying an intensity maximum at the origin whereas higher order solutions have a zero on-axis intensity. For n=0, the equation (4.1) reduces to:

$$E(r,\phi,z) = A_0 \exp(i(k_z z))J_0(k_r r) \tag{4.3}$$

which corresponds to the electric field of the ideal, zeroth order BB. The transverse intensity distribution of a BB can be obtained from the above equation (4.3) as follows:

$$I(r,\phi,z) = \left|A_0\right|^2 J_0{}^2(k_r r) \tag{4.4}$$

From equation (4.4) it is evident that the intensity distribution of the ideal zeroth order BB is independent of z, in other words is propagation invariant. This is a particularly fascinating property that characterizes zeroth order BBs, as it implies that their cross-sectional intensity distribution at any given location along the beam axis z will not change, and therefore their transverse beam profile will not spread due to diffraction as the beam propagates. This becomes evident in figure 1(b) that shows the transverse intensity profile of the zeroth order BB as it propagates along the z axis. The width of the central maximum appears unchanged with propagation with the intensity profiles appearing almost identical at any transverse plane.

Theoretically, a zeroth order BB consists of a central, pencil-like bright core that propagates without diffraction as seen in figure 1(b) and is surrounded by an infinite number of rings which correspond to the small intensity lobes on either side of the central intensity peak.

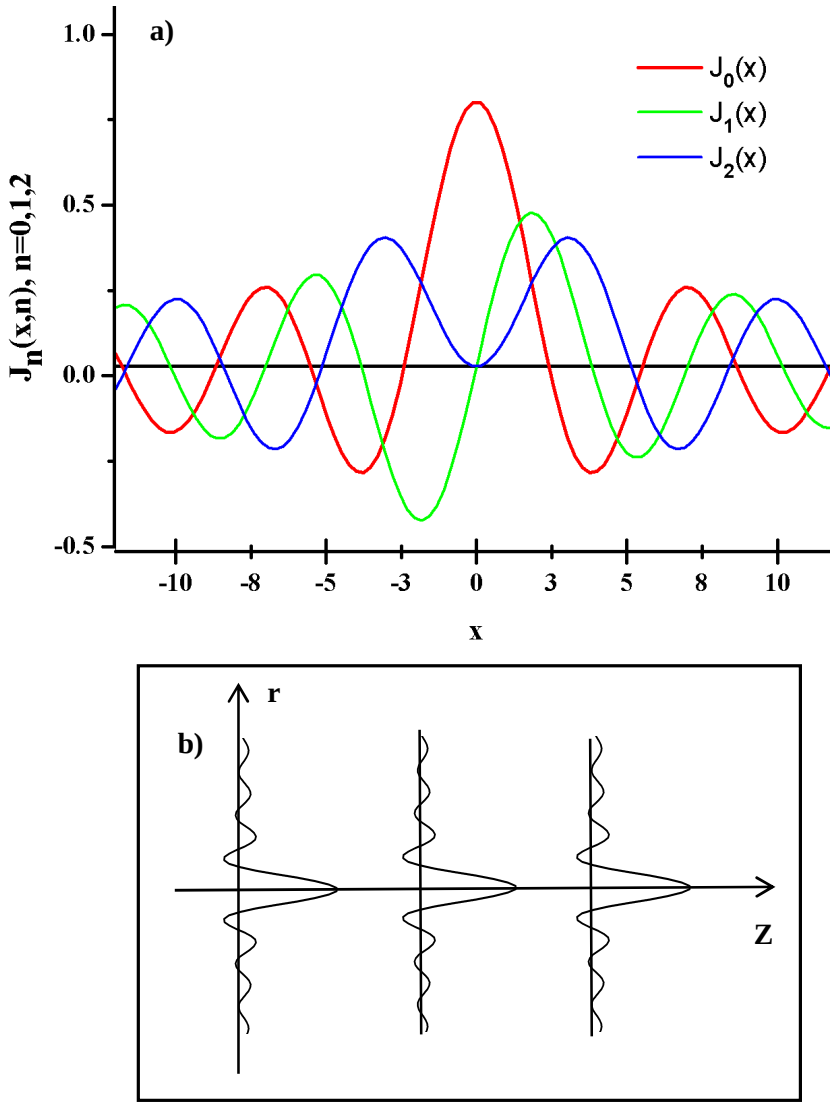

Figure 1: (a) Graphical representation of the zeroth, the first and second order Bessel functions of the first kind. Bessel functions of the first kind are finite in the origin x=0 and decay with increasing x to infinity. (b) The intensity distribution in various transverse planes along the propagation direction of an ideal zeroth order BB. Due to the "non-diffracting" character of the ideal BB, the intensity distribution will be propagation invariant, therefore it will retain its non-spreading central core to infinity.

This implies that a BB should carry infinite amount of energy. It is obvious, that in the laboratory, one deals with an approximation of a BB or a "quasi-BB", which carries the

properties of a mathematical BB, over a finite distance. Hence, a BB can be realized as a light beam that consists of a central core that propagates over a certain distance without significant spreading and it is surrounded by a certain number of rings.

Experimentally, there are a number of methods to generate a quasi-BB. A quasi-BB, as first demonstrated by Durnin *et al.* [3, 4] can be generated by illuminating an annular aperture located at the back focal plane of a lens. The resulting Fourier transform of this annulus will provide a quasi-BB. This approach is an inefficient method as most of the incident power is obstructed by the opaque part of the annular slit.

The most power efficient method for generating a quasi-BB is by means of a conical lens, known as the axicon [5-7]. As shown in figure 2(a), a collimated Gaussian laser beam illuminates an axicon of opening angle γ. The light rays emerging from the axicon will travel along a cone of opening angle θ:

$$\theta = (n_{ax} - 1)\gamma \tag{4.5}$$

where n_{ax} the refractive index of the axicon, and these rays subsequently interfere to produce the quasi-BB. In other words the axicon will impose a phase shift on the incident Gaussian beam by an amount of $\phi = k(n_{ax} - 1)\gamma$, where k is the wavevector of the constituent plane waves given as:

$$\kappa = \sqrt{\kappa_r^{\,2} + k_z^{\,2}} \tag{4.6}$$

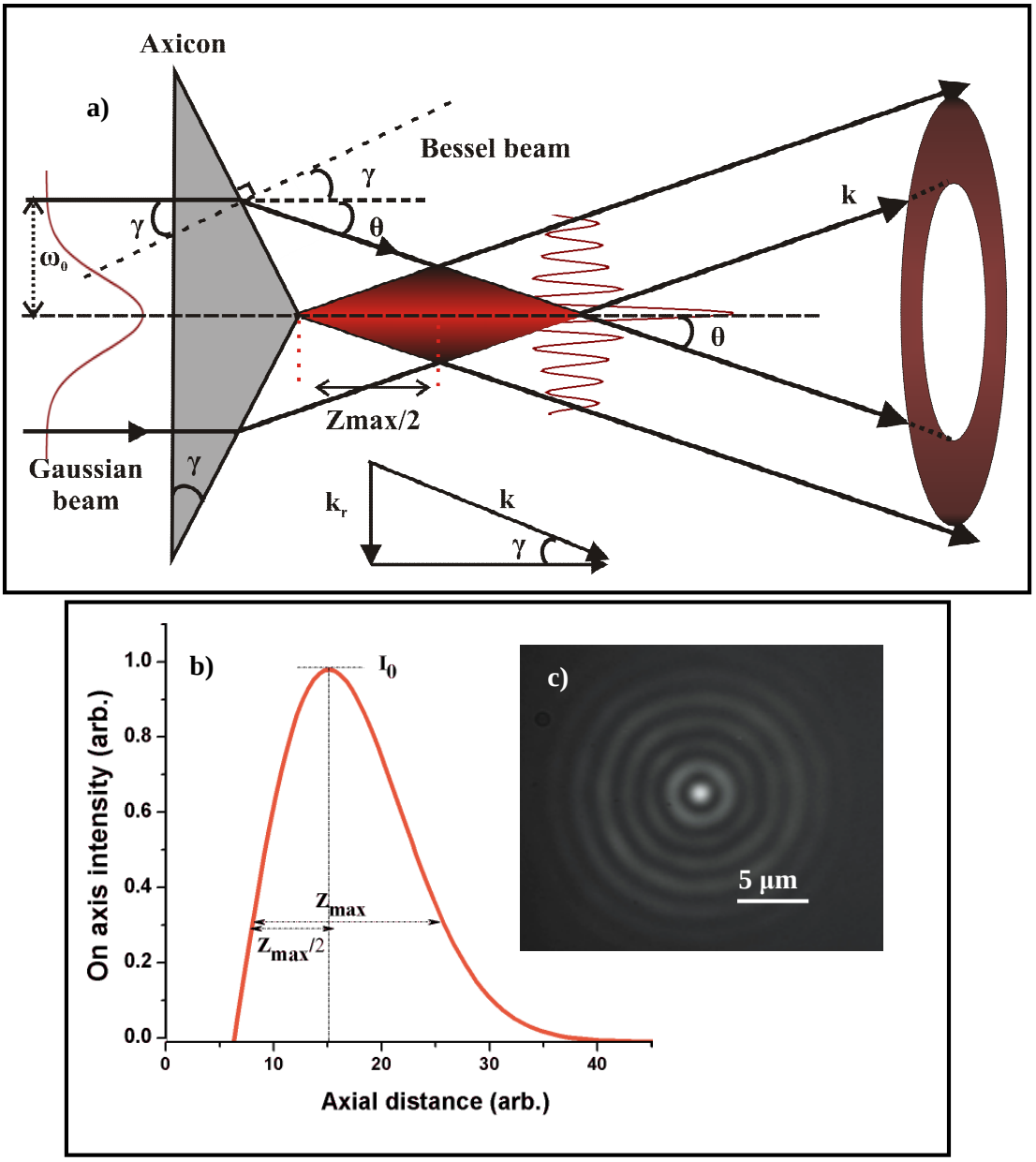

Figure 2: (a) The generation of a quasi-BB by means of a conical lens element, the axicon. The axicon, of opening angle γ and refractive index n_{ax} is illuminated by a Gaussian beam. The axicon refracts the incident rays in such a way that their wavevectors will travel on a cone of opening angle $\theta = (n_{ax} - 1)\gamma$ upon leaving the axicon. The generated interference pattern consists of a central core that propagates without significant spreading over distance Z_{max}, surrounded by a number of rings. The propagation distance and the number of rings are proportional to the incident Gaussian beam waist. At sufficiently long distance behind the axicon, we obtain the

Fourier transform of the quasi-BB which is a ring at the Fourier domain. (b) The on-axis intensity distribution of a quasi-BB. Although the central core propagates without significant spreading and retains its diameter over the propagation distance Z_{max}, the on-axis intensity will vary as a function of z, obtaining its maximum value at $z= Z_{max}/2$. (c) The cross-sectional profile of an axicon generated quasi-BB. In the case of the quasi-BB used for my photoporation experiments, the central core was surrounded by 8 concentric rings and propagated without appreciable spreading over distance 140 μm. The number of rings as well as the propagation distance is proportional to the Gaussian beam waist illuminating the axicon. The power carried by the quasi-BB is distributed evenly between the rings and the central core; therefore there is a trade-off between power obtained at the core and the length of the propagation distance.

The central core radius of the quasi-BB is inversely proportional to the opening angle of the axicon and is given by the formula [5]:

$$r_0 = \frac{2.405\lambda}{2\pi(n_{ax}\sin\theta)} \tag{4.7}$$

This implies that the steeper the axicon is, the smaller the central core diameter of the resulting quasi-BB becomes. At sufficiently long distance d behind the axicon, the quasi-BB reduces to a light ring which is the Fraunhofer diffraction pattern resulting from the axicon. The ring formation is shown in figure 2(a).

Another important property of the beam is the propagation distance. This is defined as the axial range Z_{max} over which the quasi-BB propagates whilst maintaining its cross-section. At this axial length the on axis intensity will be the 32.27% of its peak value observed at half the propagation distance $Z_{max}/2$. The on-axis intensity profile of the beam's central core is shown in figure 2(b). Figure 2(c) shows the transverse profile of

the quasi-BB at $Z_{max}/2$. The axicon generated quasi-BB used for the photoporation experiments described here, was composed of a central core and was surrounded by 8 rings. The propagation distance and the number of rings surrounding the central core are proportional to the Gaussian beam waist ω_0. The propagation distance is given by the formula (considering the paraxial approximation):

$$Z_{max} \cong \frac{\omega_0}{\theta} \tag{4.8}$$

It is important to emphasize that a comparison between quasi-BB and a Gaussian beam is referring to the comparison between the central core diameter of the former and the beam spot size $2\omega_0$ of the latter [8]. Although it is possible to generate a very long "non-diffracting" central core of a quasi-BB, this comes at the expense of power loss in the central region of the quasi-BB as the power is dissipated equally to the rings and the central maximum.

In the recent years, a very popular route towards generating a quasi-BB in a laboratory environment is the use of holograms which are generated by SLMs or through microfabrication [9-12]. SLMs have become very powerful tools for generating BBs and in general a variety of light patterns. This method will be described in more detail in following sections.

Another important property of the quasi-BB is the property of self-reconstruction [13]. When the centre of the beam is partially obstructed by an opaque object of width a, the light rays move around the obstructive object and restore the non-diffracting profile of

the beam at a certain distance behind the object. This distance is denoted as z_{min} and is given by the equation:

$$z_{min} = \frac{ak}{2k_z} \tag{4.9}$$

The width "a" of the obstructing object is measured from the beam center. This exact property of the quasi-BB has enabled us, as it will be discussed in a following section, to perform successful photoporation of CHO cells through an obstructive layer of silica particles.

Please note that in the sections and chapters that follow, the term "quasi-BB" will be quoted as "BB" for ease in typing and simplicity. However, the distinction between those two terms has become clear and should be considered throughout this thesis. In the following section, I describe the experimental procedure of fs transfection of CHO cells using a BB with details on the sample preparation protocol and a discussion on the obtained results.

4.2 Optical transfection using a Bessel beam

4.2.1 Experimental setup

I explored photoporation and transfection of CHO cells using an axicon generated BB. The experimental setup used here is shown in figure 3. A Gaussian beam with diameter approximately 2 mm was generated by a Ti: Sapphire laser and was subsequently directed through a x4 demagnifying telescope, which consisted of a set of two achromatic

doublet lenses F_1 = 200 mm and F_2 = 50 mm. This telescope decreases the Gaussian beam waist illuminating the axicon therefore giving rise to a BB of shorter propagation distance and hence smaller number of rings. This implies that the power delivered on the axicon will be distributed evenly to a smaller number of rings and therefore higher power will be confined in the central core which is required for photoporation. The demagnified Gaussian beam, of beam waist ω_0 =0.25 mm, was subsequently incident on an axicon of opening angle γ=5°, rendering a BB with theoretical central core diameter r_0 =14 μm and theoretical propagation distance Z_{max} =5.6 mm. The generated BB was subsequently passed through a x8 demagnifying telescope consisting of a set of two lenses; an achromatic doublet lens of focal length F_3=34 mm and an aspheric lens of focal length F_4=4.25 mm. This telescope renders a BB with theoretical central core diameter of $1.75\,\mu m$, given by the formula:

$$r_0' = \frac{1}{8} r_0 \tag{4.10}$$

where r_0' is the central core diameter of the demagnified BB. Experimentally, the $1/e^2$ central core diameter upon the final telescope was estimated to be 1.8 ± 0.3 μm which compares favorably with the theoretical calculations.

Figure 4 (a) shows part of the BB photoporation optical setup as built in the laboratory. The image displays the axicon, the demagnifying telescope following the axicon, the sample stage and the imaging microscope objective.

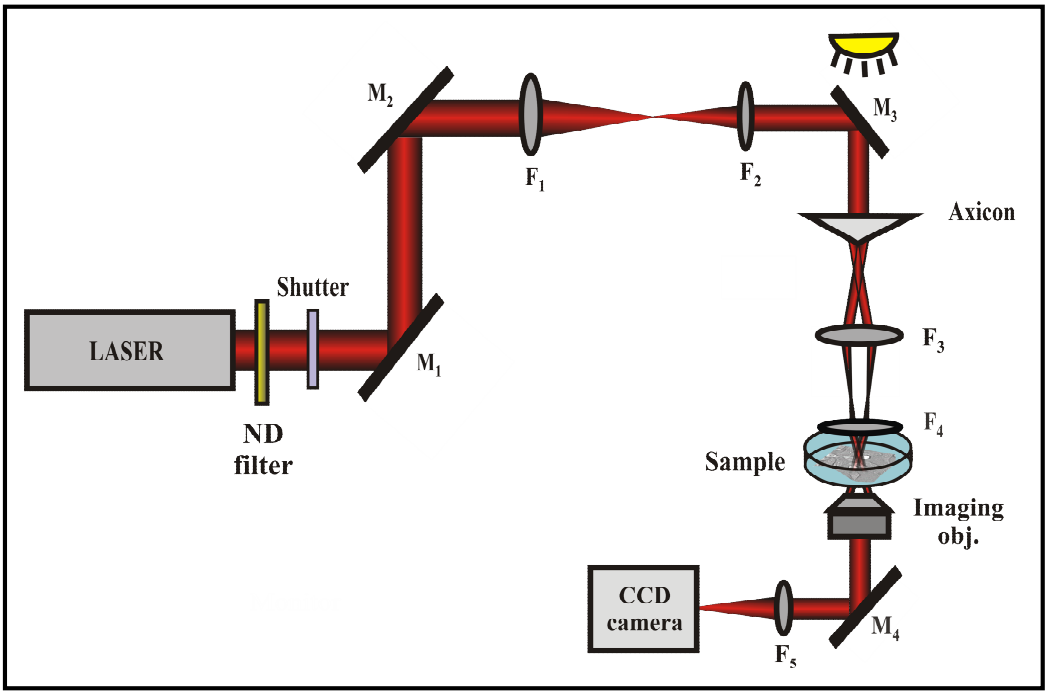

Figure 3: BB transfection apparatus. A laser beam was directed through a neutral density filter (ND filter) and a mechanical shutter that controlled the input power and the duration of the laser dose respectively. The beam was subsequently directed by a periscope (M_1 and M_2) through a x4 demagnified telescope. The latter consisted of two achromatic doublet lenses F_1 =200 mm and F_2 =50 mm and served the purpose of decreasing the Gaussian beam waist in order to obtain a BB of shorter propagation distance and smaller number of rings. This would allow for higher power into the central core required for photoporation. The Gaussian beam, emerging from the telescope, was subsequently reflected off the M_3 mirror and illuminated the axicon which generated the BB. The BB was then demagnified using a x8 telescope consisting of an achromatic doublet lens F_3 =34 mm and an achromatic lens F_4 =4.25 mm. This reduced the central core diameter of the generated BB as well as shortening the propagation distance. Bright field illumination was provided from above whereas imaging of the sample and the laser beam was provided by a microscope objective (Mitutoyo, x100, NA=0.7) that collected and directed the transmitted rays through a mirror M_4 and the F_5 =100 mm tube lens on a CCD camera.

In figure 4(b), the axicon is illuminated by the Gaussian laser beam and renders the BB which is directed to the cell sample. The demagnifying telescope that follows behind the axicon was omitted from the image for clarity. The transverse intensity profile of the beam's central core appears unchanged over the propagation distance.

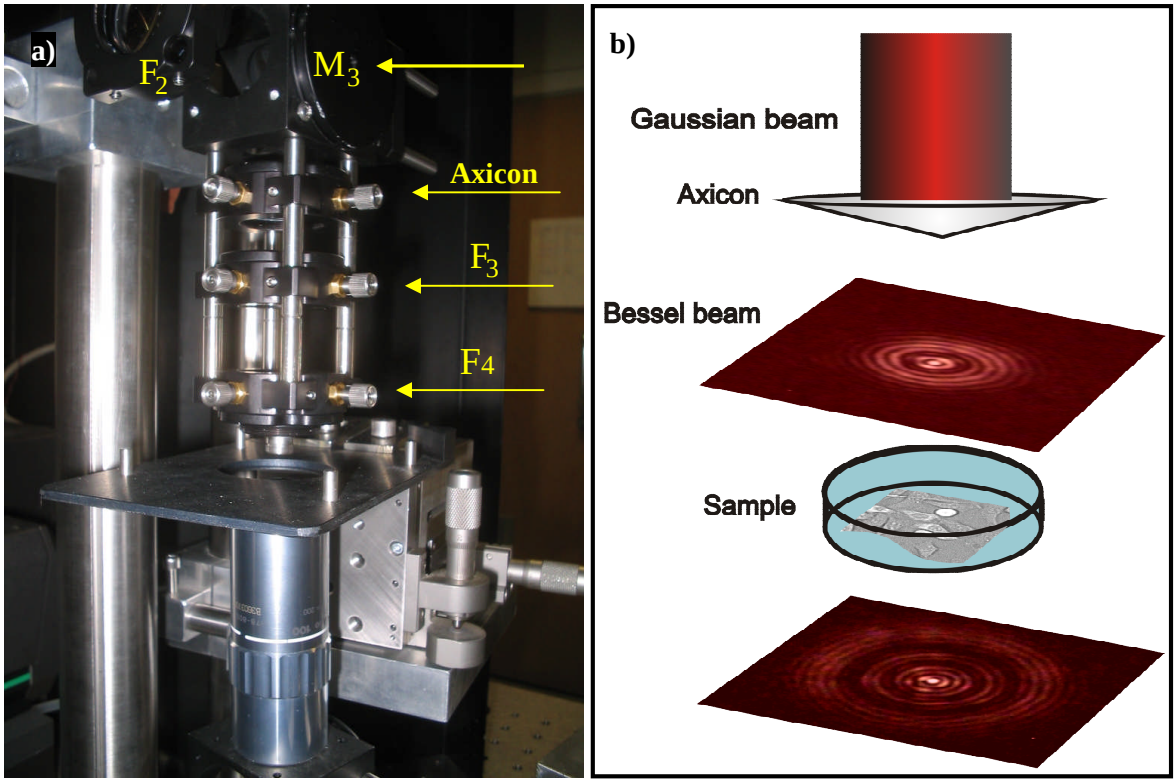

Figure 4: (a) Part of the BB photoporation setup illustrating the arrangement of the axicon with respect to the second demagnifying telescope (F_3 and F_4) and the sample stage. The mirror M_3 is mounted on a cage cube at 45° with respect to the horizontal direction. The second lens, F_2, of the telescope prior the axicon, can also be discerned in the image. The imaging objective collected the transmitted light rays from the sample, which was subsequently directed on a CCD camera through a mirror and the tube lens. The final lens of the telescope F_2 prior the axicon can also be distinguished in the image. The rest of the setup is omitted for clarity purposes. (b) Image of the axicon generated BB incident upon the sample. The central core of the beam appears to retain its diameter with increasing axial distance.

Thus, photoporation of cells becomes possible over a long axial range. The theoretical propagation distance was estimated to be $90\,\mu m$ according to the formula:

$$Z_{max}' = \frac{1}{64} Z_{max} \tag{4.11}$$

Experimentally, the beam appears to propagate without visible spreading over a distance of 180 ± 10 μm. However, if we consider the propagation distance to be the axial distance at which the on-axis intensity decreases to 32.27% of its peak value, then the estimated propagation distance is 140 μm.

This can be verified from figure 10, in the following section 4.2.3, which relates the measured on-axis intensity of the BB and the transfection efficiency obtained as a function of the axial distance. The mismatch between the theoretical and experimental value of the beam's propagation distance, may have been due to unavoidable experimental inaccuracy in the positioning of the lenses F_3 and F_4 following the axicon.

The purpose of the final demagnifying telescope was to reduce the propagation distance of the BB as well as to decrease the central core width. As a result of the demagnifying telescope, the energy that was previously contained within a wide central core is now confined within the minute area of the demagnified beam core. In addition, more power is now available within the beam's central lobe, therefore the on-axis peak intensity will significantly increase as evident from figure 5.

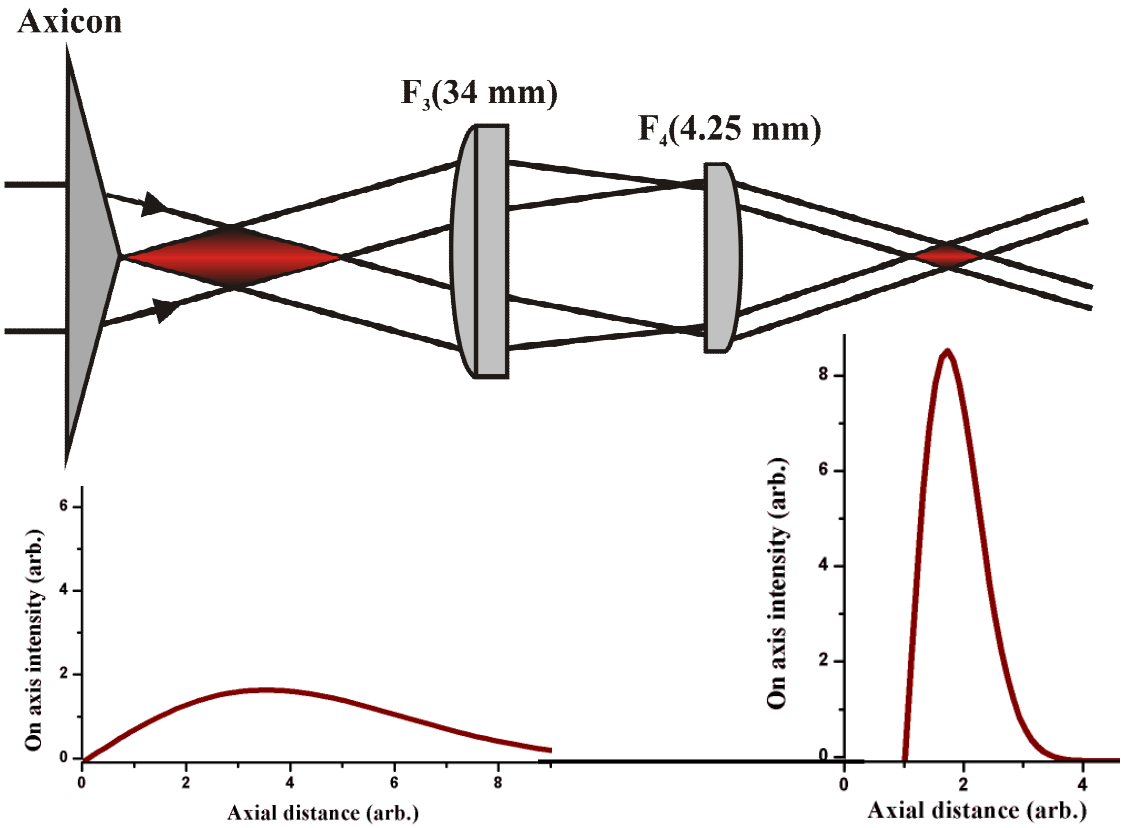

Figure 5: The axicon generated BB is directed through a x8 demagnifying telescope consisting of two lenses F_3=34 mm and F_4=4.25 mm. The telescope will cause reduction in the central core width as well as shortening of the propagation distance. The energy, which prior to the demagnifying telescope was distributed over a greater area within the central core, will now be confined within a significantly smaller area within the central core. In addition, due to the shortening of the propagation distance, the energy dissipated within the central core as opposed to the rings will be considerably higher resulting in an increase in the on-axis peak intensity.

Thus, the photon flux in the central core region will also be enhanced which is a prerequisite for the multiphoton plasma formation during photoporation.

The optical system had a 78% power transmission efficiency yielding a BB of power approximately 630 ± 1 mW entering the sample, corresponding to a mean power of 70 ± 1

mW in the central core. Figure 6(a) shows the side view of the CHO cell sample in the presence of the BB during photoporation and figure 6(b) shows the lateral view of the CHO sample in the presence of the BB at axial distance z=60 µm along its propagation direction.

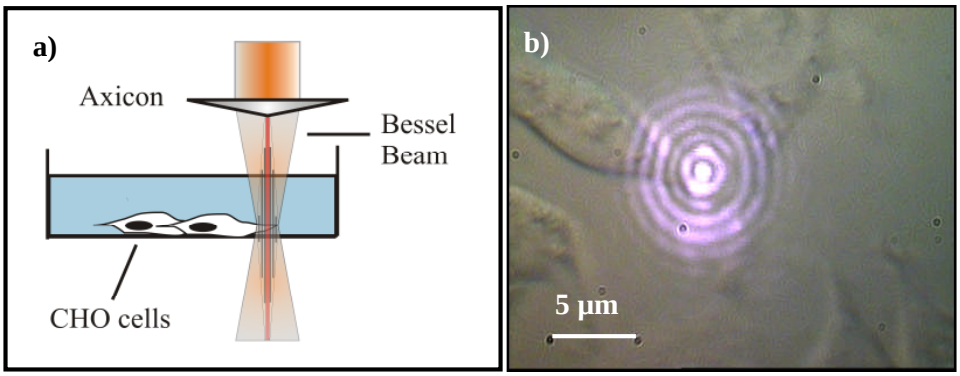

Figure 6: (a) BB transfection of CHO cells. The "non-diffracting" nature of the beam offers "focus-free", alignment free photoporation over long axial distances. (b) BB profile at axial distance z= 60 µm on the CHO sample.

4.2.2. Sample preparation protocol

The cell preparation for this set of experiments follows the same protocol as the one described in section 3.2.3 of the previous chapter. Each cell was treated with three laser doses, each of 40 ms duration. The total number of cells photoporated per dish was fifty and at each axial position, six to seven dishes were treated, giving a total number of three hundred to three hundred and fifty cells photoporated at each axial position. As in the case of Gaussian photoporation experiments, each photoporated dish was accompanied by a control dish. The average number of spontaneously transfected cells in the control dishes varied between zero and five. Upon laser irradiation, the sample was returned to

the incubator where it was kept for 48 h. Upon this time, fluorescent microscopy showed that transient red fluorescent protein (RFP) expression was achieved and that cells expressing RFP were viable and displayed normal morphology, thereby confirming that successful optical transfection had occurred. Figure 7(a) shows the CHO cells in the presence of BB prior to photoporation and in figure 7(b) the cells are shown expressing RFP after laser treatment.

The next section details the comparison between Gaussian beam and BB photoporation and transfection of CHO cells. This comparison is aiming to illustrate the merits of using a “non-diffracting” beam for laser assisted transfection as opposed to a highly divergent Gaussian beam.

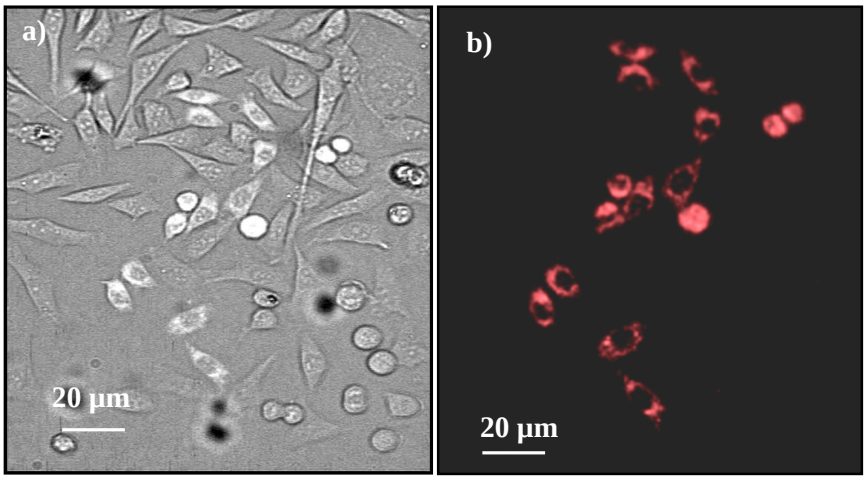

Figure 7: (a) Chinese hamster ovary (CHO) cells 48 h upon photoporation in the presence of DS-Red encoding plasmid DNA. (b) CHO cells expressing the red fluorescent protein after photoporation using a BB.

4.2.3 Gaussian vs. Bessel beam transfection

For the purpose of comparing the transfection rate of CHO cells using a Gaussian and a

Bessel beam, the spot sizes of the beams were matched equal to 1.8 µm. However, the BB propagated without appreciable spreading over axial distance 140 µm which was more than twenty times greater than the confocal parameter of the Gaussian beam. The transfection efficiency/viability data as a function of axial distance, collected using the Bessel and Gaussian beams, are summarized in table 1. As shown in figure 8, the transfection rate obtained using both beams was monitored as a function of the position of the cell membrane along the axial beam propagation direction. Figure 9 displays the obtained transfection efficiency versus axial distance for both Gaussian and Bessel beams. If we define a threshold for transfection of 20% (dashed red line), for example, from these data it becomes obvious that the given BB gives us transfection over twenty times the axial transfection length compared to the Gaussian beam.

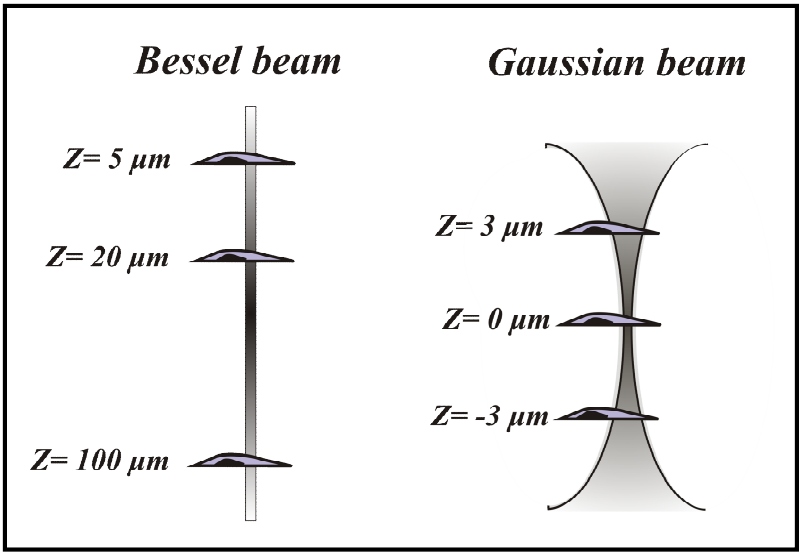

Figure 8: The generated BB exhibits an elongated depth of focus which was more than twenty times longer than the confocal parameter of the equal in spot size Gaussian beam. Transfection efficiency was monitored as a function of the position of the cell membrane at various axial locations along the propagation direction.

Transfection efficiency/Viability (%) using a BB									
N	**Z=-40 µm**	**Z=-20 µm**	**Z=0**	**Z=20 µm**	**Z=40 µm**	**Z=60 µm**	**Z=80 µm**	**Z=100 µm**	**Z=120 µm**
1	10	20	55	42	26	19	8	18	0
2	14	8	75	20	20	25	27	27	33
3	27	20	60	28	20	30	20	25	25
4	4	16	35	30	25	20	30	30	9
5	15	27	15	60	28	18	12	12	10
6	0	9	40	18	11	19	40	40	12
7	8	38	65	20	20	15	20	20	0
Ave-rage	**11**	**20**	**49**	**31**	**21**	**22**	**22**	**25**	**13**

Transfection efficiency/Viability (%) using a Gaussian beam							
N	**Z=-10 µm**	**Z=-6 µm**	**Z=-3 µm**	**Z=0 µm**	**Z=3 µm**	**Z=6 µm**	**Z=10 µm**
1	22	34	38	84	16	26	0
2	4	20	10	62	36	20	0
3	0	2	4	50	15	0	8
4	0	0	4	24	2	0	7
5	0	20	20	70	38	3	0
6	5	8	12	31	18	5	8
7	10	16	11	40	20	15	4
Average	**6**	**14**	**15**	**52**	**21**	**10**	**4**

Table 1: CHO cell transfection efficiency/viability (%) as a function of the axial distance (z) using a BB and a Gaussian beam. At each axial distance z, at least 7 sample dishes were prepared and used. Within each dish 50 cells were photoporated. The transfection efficiency percentage was calculated as the number of cells photoporated (t=0) over the number of red fluorescent cells (t=48 hours). The errors are not included in this table.

The transfection efficiency obtained using the BB, appears to follow the axial intensity profile of the beam, with the intensity maximum observed at axial distance z=40 μm, as shown in figure 10. Maximum transfection rate of cells is observed at the plane of maximum intensity.

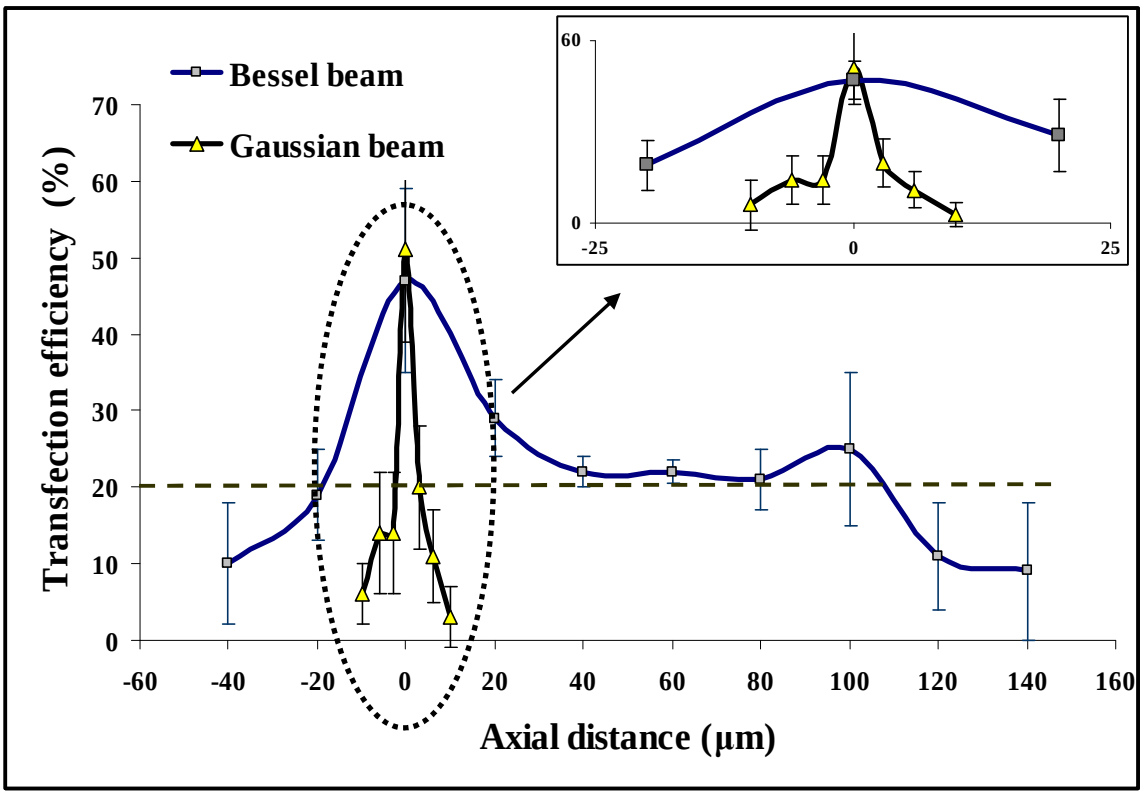

Figure 9: BB transfection vs. Gaussian beam transfection. BB transfection of CHO cells was observed over twenty times the axial transfection range compared to the Gaussian beam, assuming an efficiency threshold of 20%. Each data point corresponds to the average transfection efficiencies obtained at a specific axial position and includes the number of spontaneously transfected cells, which varies between 0 and 5 for each sample dish. The magnified image of the area around z=0 which is assumed to be the point of maximum intensity for both beams can be viewed on the top right part of the main graph. When moving axially away from the point of peak intensity, the use of a BB for photoporation can provide sufficient transfection as opposed to the Gaussian beam, which provides transfection only at very close proximity to the beam waist.

Small intensity fluctuations occur along the axial direction of the beam, which may contribute towards the fluctuations observed in the transfection rate along the axial direction of propagation. These fluctuations have been reported by Brzobohaty *et al.* and have been attributed to the slightly convex shape of the axicon tip [14]. These intensity oscillations can be eliminated by introducing an opaque circular aperture between the BB demagnifying telescope (figure 3) with radius that is determined by the inner diameter of the BB ring. In this case, the aperture would be positioned at distance F_3 behind the first lens of the telescope and at distance F_4 before the aspheric lens.

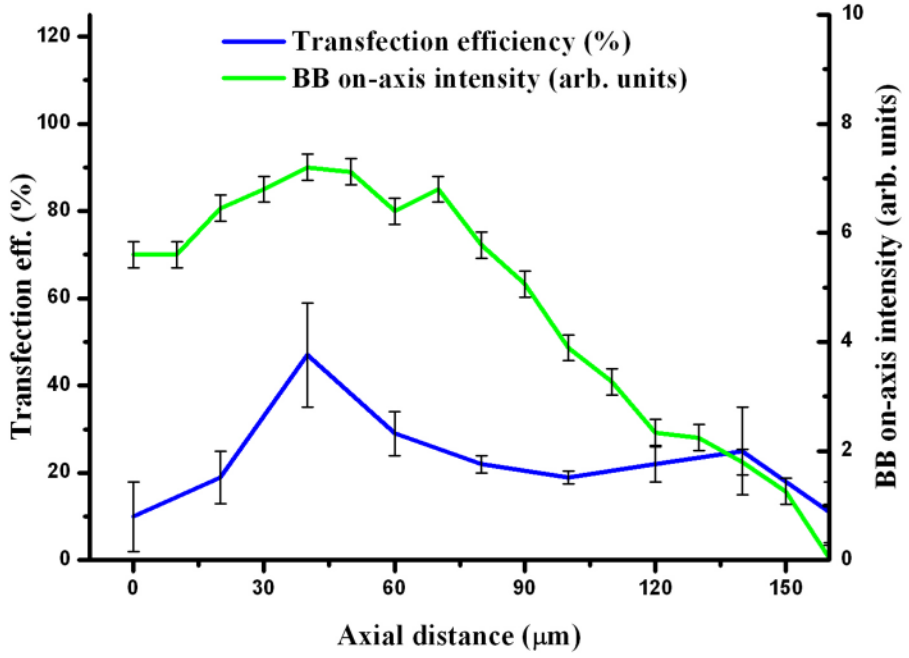

Figure 10: BB axial intensity profile and transfection rate of CHO cells vs. axial distance. At constant power at focus, the rate of transfection follows the axial intensity of the beam. Intensity fluctuations due to the oblate tip of the axicon can also be observed that may be related to fluctuations in the transfection rate using a BB.

This spatial filtering method should be introduced whenever an axicon generated BB is experimentally employed, as it corrects for the any aberrations introduced by the axicon and recovers the “non-diffracting” profile of the beam over a long distance. In previous work [15], the expression of green fluorescent protein has been used as a marker for transfection. However, in this case we chose to use a plasmid which encodes for the mitochondrially targeted *Discoideum* red fluorescent protein. This additionally proved that the cells were unharmed by the laser as the RFP protein after synthesis was targeted correctly to the mitochondria.

I believe that BB photoporation provides a significant advancement which will be very beneficial for many biological applications. By implementing the BB for cellular transfection, the need for exact focusing of the laser beam upon the cell membrane has been alleviated, enabling the automation of a sterile and ultra-precise technique, as exact determination of the cell surface position will no longer be required. However, what is gained in focal length when using a BB is lost in power as each lobe (the area between two successive zeros) of the BB carries the same energy as the central core. For example, in the case of the BB with 8 lobes as the one used for the photoporation experiments, only 11 % of the total input power was carried in the central core as opposed to its equivalent in spot size Gaussian beam that carried 50% of the total power within its FWHM area.

The comparison between the transfection efficiency range using a Gaussian beam and a BB is only valid when referring to beams of those particular propagation parameters. However, the axial range over which transfection is successful will vary for beams of different propagation properties. For typical photoporation experiments, a BB of shorter

propagation distance (ideally no shorter than 60 to 80 μm) is also suitable however the diameter of the central core should be kept relatively small (ideally less than 3 μm) to ensure multiphoton excitation at low average powers. The use of SLMs or the combination of an axicon and an SLM, as reported in the next section, are ideal tools for providing a BB that is tailored for photoporation applications.

4.3 Optical transfection using a reconstructed Bessel beam

In this section, I present how the self-healing property of the BB [13] was exploited in order to provide transfection of CHO cells through a "turbid" medium. The "turbid" medium used, was a 23 mm diameter type-0 coverslip covered with a layer of polymer colloids. This obstructing layer was fabricated in the cleanroom, by covering the glass coverslip with a concentrated polymer colloid solution and was subsequently spun at 5000 rpm on a photoresist spinner before being baked at 100 °C on a hot plate for 4 min. The diameter of the colloids was 1.0 ± 1 μm. This provided a thin layer of randomly distributed dried colloids lightly adhered across the coverslip surface. Following this, I subsequently autoclaved the coverslip at 120º to provide sterility. The cell sample preparation for photoporation experiments was performed as described in section 3.2.3. Figures 11(a)-11(c) show the experimental process and the reconstruction of the BB upon encountering the obstructive layer.

The BB passed through a coverslip covered in colloids and as a result its profile became partially distorted. By adjusting the XYZ translation stage along the axial direction, the gradual self-reconstruction of the beam was observed. Initially, the lateral plane of the

BB at z=10 μm (arbitrarily chosen) was positioned on the obstructing coverslip. At that location the BB profile appeared distorted. By adjusting the imaging objective lens within the axial range of 50 to 80 μm along the beam's propagation direction, it was observed that the beam profile was restored. The beam was subsequently positioned on the cell membrane and successful transfection was initiated.

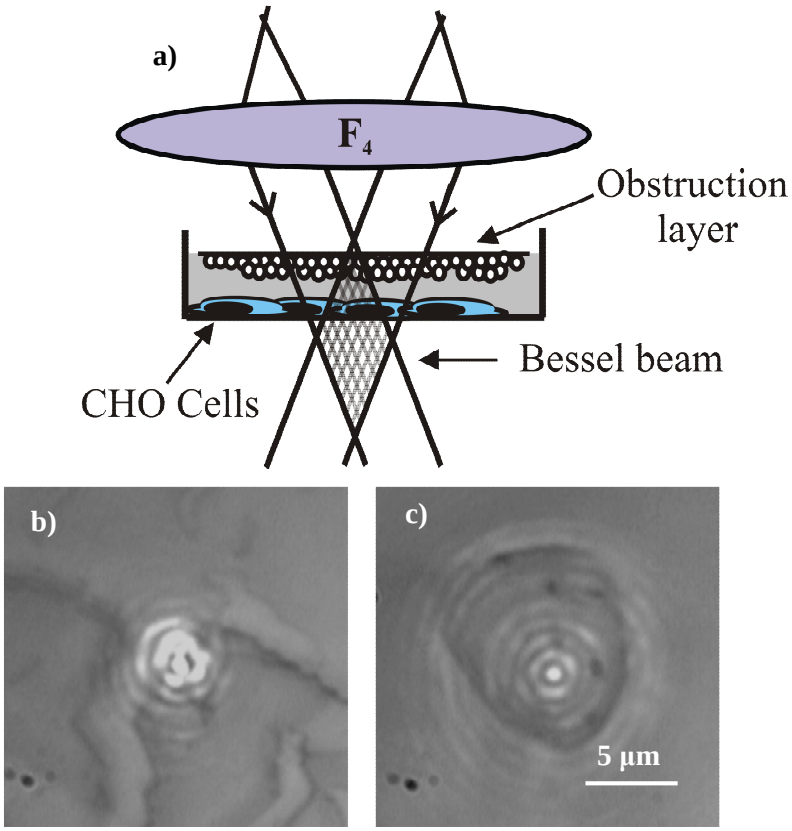

Figure 11: (a) The BB passed through the obstructive layer of microspheres which caused its profile to become distorted. Due to the self-healing property of the BB, at 50 to 80 μm behind the colloid layer the beam profile is reformed and reaches the cell plane where photoporation will occur. (b) The BB profile was distorted after passing through the colloid obstructive layer. (c) The BB was reconstructed after 50 to 80 μm (depending on the sample), was subsequently imaged on the cell membrane and photoporation took place.

Equation (4.6) gives us the reconstruction distance of a partially obstructed ideal BB as a function of the axicon cone angle and the width of the obstructive object. In the case described herein, the obstruction is not an opaque object of a certain width from the center of the beam. Instead it is a glass coverslip coated with 1 μm polymer spheres through which the BB is travelling prior to reaching and dosing the cells. The reconstruction distance of the beam is difficult to calculate due to the different shape and size of the obstruction used compared to that quoted in theory. Experimentally, the observed beam reconstruction distance varied as expected from sample to sample. This is due the obstructive layers varying in thickness from one another and the random distribution of the microspheres over the coverslip surface. In addition, the amount of solution surrounding the cells may vary slightly from one sample to the other due to solution displacement whilst floating the coverslip on the solution surface as well as the gradual evaporation of the extracellular solution in the course of the photoporation experiments.

A total number of eighty cells (four sample dishes, twenty cells per dish) were photoporated using the reconstructed BB and four control dishes were also examined for spontaneous transfection using the obstructing coverslips. The transfection efficiency obtained was 24± (1%) and no spontaneously fluorescent cells were observed. The reduction in transfection efficiency obtained can be associated with power loss in the beam central core due to the beam passage through the obstructing layer and to the expected intensity reduction away from the axial position where the beam's peak intensity is observed. By increasing the power fed into the photoporation system, one can compensate for this power dissipation and therefore increase the transfection efficiency.

However, in this case, the amount of laser power available was not sufficient to further increase the input power on the cell sample.

Successful optical transfection of cells using a BB through reconstruction is an important result that holds promise for future attempts of photoporating through turbid media such as cell monolayers or specific tissue parts. Selective delivery of DNA or therapeutic agents in tissue is of great interest for studying tissue properties and cell signaling within the tissue complex environment.

The next section describes BB photoporation using a combination of an axicon generated BB and an SLM. This arrangement provided a “point and click” BB whose 3D positioning was computer controlled. This experiment was the first successful attempt towards automating the photoporation process.

4.4 Femtosecond transfection of CHO cells using a “point and click” BB

Optical transfection of cells by means of a BB is a powerful tool in the hands of life scientists, as it eliminates any alignment difficulties associated with the precise positioning of the laser focus to the cell membrane; a prerequisite linked to Gaussian beams. This “focus-free” approach for photoporation could lead to automation of the technique, enabling users from a variety of disciplines to perform standard photoporation experiments with minimal requirements for optimization of the optics. In this section, I will describe the generation and implementation of a computer controlled, point and click BB that provides the first steps towards an automated and alignment free optical

transfection. In this method, a BB was generated using an axicon and its spatial spectrum was subjected to phase modulation using an SLM [16]. Control and modification of the spatial spectrum of a BB provides with a variety of capabilities such as control over the axial and lateral positioning of the beam within the sample as well as the generation of multiple sub-BBs for simultaneous photoporation of cells.

4.4.1 Experimental setup and cell preparation protocol

SLMs are powerful devices for dynamically reconfiguring the intensity and phase of light beams. Typically, they consist of a two dimensional array of liquid crystal pixels that can be electrically addressed. Due to the birefringent properties of the liquid crystal molecules, the polarization of the incoming light can be altered by electrically changing the orientation of the liquid crystals. This results in intensity or/and spectral phase modulation of the output (normally reflected) light. SLMs have been directly used to generate a variety of optical landscapes and patterns in the context of optical trapping as well as for laser beam shaping and generation of novel beams such as BBs or Airy beams [17].

In order to generate an array of “non-diffracting” beams, a number of methodologies have been employed. By separating the SLM chip in regions and applying an axicon phase modulation over each one of them [18] or alternatively imprint several annular sub-domains on the SLM chip followed by a lens element, a desired array of BBs could be generated. By using these methods, 3D positioning of the generated beams is limited whilst avoiding spatial overlap and undesired aberrations due to interference between the

rings of adjacent sub-BBs. Direct use of micro-fabricated holograms [9] has also been reported however this approach does not allow for dynamic reconfiguring of the generated array of beams.

Our approach was to use an SLM to dynamically reconfigure the spatial spectrum of an axicon generated BB. In particular, the SLM is providing phase modulation at the annular spatial spectrum (far field) of the BB, at the Fourier plane within a magnifying telescope located behind the axicon. This approach allows us to exploit the whole area of the SLM chip instead of the limited size sub-domains, allowing for greater power efficiency and improved quality of the generated beams. By appropriately phase modulating the BB ring, we can control the position of the generated BB in the lateral and axial direction or generate a number of parallel BBs that could be accurately and independently positioned.

The ability to accurately position the BB along the lateral and axial direction with respect to the cell sample, opens up new prospects in the way photoporation is performed. This approach allows for a “focus-free” photoporation, whereby the laser dose is delivered on the chosen cell by simply clicking the computer mouse.

Figure 12 shows the optical setup used for optical transfection of CHO cells using an SLM modulated BB. The implemented laser beam had a Gaussian profile of waist size 530 μm. Using an axicon with apex angle 178.6º, we generated a BB of propagation distance 89 mm and cone angle θ=0.35º. The spatial spectrum modulation was provided by the SLM which was positioned between a lens telescope consisting of two lenses L1 (F_1=100 cm) and L2 (F_2=40 cm). The SLM was located at a distance F_1 behind the L1

lens and at a distance F_2 prior to the lens L2. The focal length of the L1 was selected so that the spatial spectrum ring of the BB, of radius 6.1 mm, could be as large as possible to fit into the SLM chip. This would ensure optimum modulation efficiency. A small beam blocker was introduced at the back focal plane of the L2 lens to remove the undesirable zero order diffraction from the SLM where no phase modulation was applied. The beam is subsequently passed through a demagnifying telescope consisting of two lenses L3 (F_3 =150 mm) and L4 (F_4 =8 mm) that deliver a BB of propagation distance 40 μm and cone angle 16.4º.

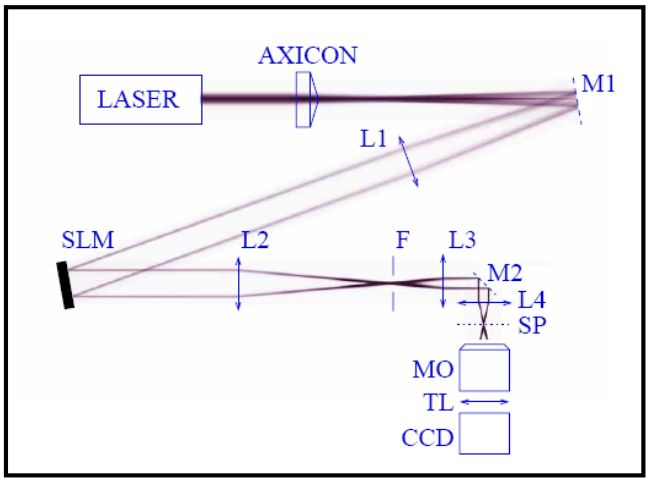

Figure 12: Optical setup for spectrally modulated BB. The phase modulation is provided by positioning the SLM at the Fourier plane of the L2 lens within the telescope consisting of L1 and L2 lenses. Further demagnification of the resulting BB was possible by introducing another telescope consisting of L3 and L4 lenses, in order to ensure the beam was of suitable size and carried sufficient power for photoporation. Spatial filtration (F), by means of a circular aperture, was also introduced to ensure good beam quality. (M1, M2: mirrors, L1, L2, L3 and L4: lenses, SP: sample plane, MO: microscope objective, TL: tube lens)

In this matter, we obtain a beam of suitable size and power efficiency for photoporation. The imaging system comprised of a long working distance microscope objective

(Mitutoyo M Plan Apo 80x) and a 200 mm tube lens onto a CCD camera (BASLER piA640-210gm). The cell sample was accommodated on an XYZ translation stage that provided positioning of the cells in three directions.

Due to the slightly convex shape of the axicon tip, as a result of fabrication imperfections, the quality of the beam was compromised by periodic modulations of the on-axis intensity profile of the beam. In order to compensate for these periodic modulations, (phase) modulation was applied only in the ring area not in the enclosed area inside the ring. This played the role of low-pass filtering of unwanted parts of the spectrum, which was originally proposed in the form of a circular annulus [14]. Figure 13 shows the spatial filtering applied.

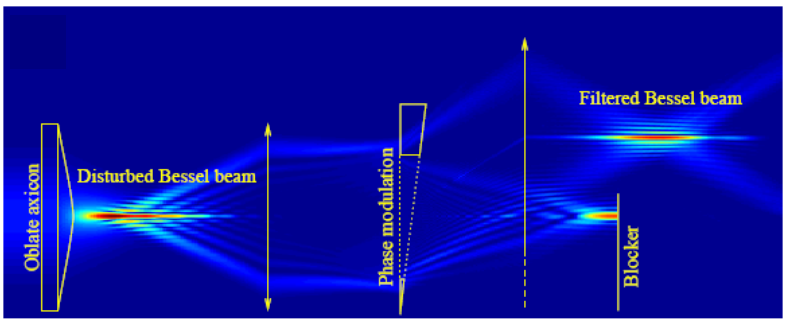

Figure 13: Linear modulation of the spatial spectrum of the BB in conjunction with phase modulation acting as a low-pass filter eliminates the on axis intensity modulations resulting from the convex tip of the axicon.

The diameter of the non-modulated annular area was determined to be slightly larger than the size of the spatial spectrum ring of the BB. As the thickness of the ring-like spatial spectrum of beam is proportional to $1/\omega$ and therefore to$1/z_{max}$, the spatial spectrum filtration resulted in a slight increase of the propagation distance of the beam to up to 55

μm. The additional advantage of this approach was also the faster computational time required for calculating and applying the linear phase on the ring area as opposed to the whole of the SLM area.

Figure 14 shows the simulation of various phase modulations applied to the spatial spectrum of the axicon generated BB. In figure 14(a), no phase modulation is applied, whereas in figures 14(b) and 14(c) linear phase masks are imprinted on the SLM chip allowing for positioning the BB in the lateral plane. In figures 14(d) and 14(e), quadratic phase functions are applied, providing axial control of the beam with respect to the sample. In Figure 14(f), a binary modulation is applied. The SLM acts as a binary diffraction grating, providing several parallel sub-BBs, each corresponding to a different diffraction order that can be positioned independently in 3D.

For controlling the SLM a mouse-driven interface was developed using LabView. When clicking on the camera image downloaded into the interface, the program calculates the phase modulation and applies it to the SLM chip. This way the center of the BB appears in the position of the mouse. Revolving the mouse wheel controls the quadratic phase on the SLM thereby resulting in axial positioning of the beam.

For the purposes of photoporation, no binary phase modulation was provided as that would significantly decrease the amount of power on the central core of each daughter beam. However, it was possible to control the position of the resulting BB with respect to the sample plane in 3D. The cell sample was prepared as described in section 3.2.3 of chapter 3. Each cell in the sample dish was treated with three laser exposures, each of 40 ms duration, at a power level of 30 mW in the central core.

4.4.2 Results and discussion

48 hours after laser treatment, the cells were observed under a microscope for red fluorescent protein (RFP) expression showing that successful photoporation was achieved. The total number of cells photoporated was 150, and four control sample dishes were also monitored showing zero to three spontaneously transfected cells. The power on the central core of the BB was 30 mW which was lower than the power used for the initial experiments using a BB as described in chapter 2. This was due to the low power efficiency of the SLM (~50%) as well as power loss due to spatial filtering, the various optical elements as well as dissipation in the rings of the BB.

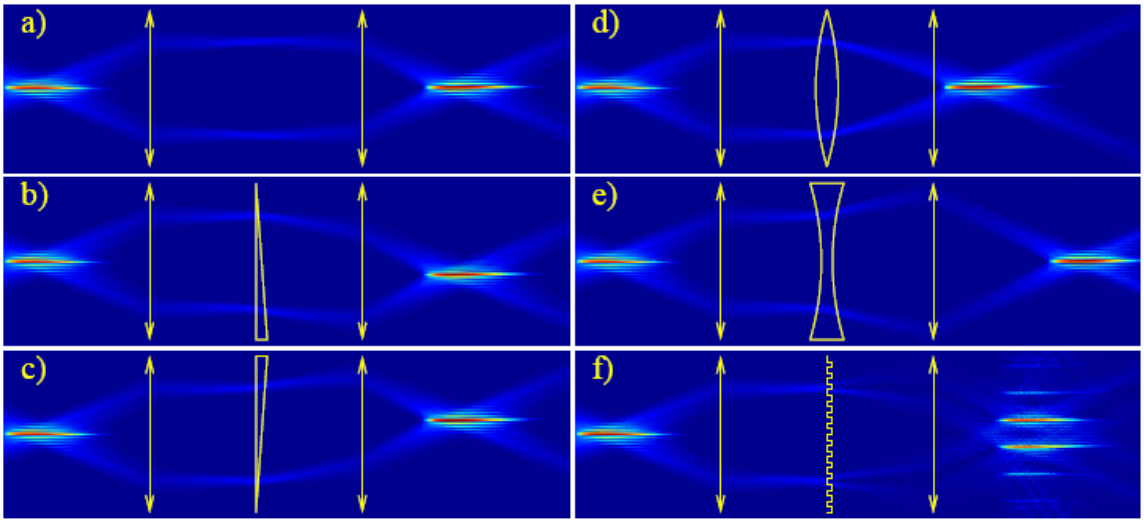

Figure 15: Phase modulation of the spatial spectrum of the axicon generated BB. (a) No phase modulation is applied. (b)-(c) A linear phase function is applied allowing for positioning the beam along the lateral direction. (d)-(e) A quadratic phase function is applied providing axial positioning of the beam. (f) A binary phase mask is applied allowing for generation of a number of sub-BBs.

This resulted in 35% transfection efficiency. During photoporation, as described herein,

the plane of maximum axial intensity of the BB was aligned with the cell membrane. It is worth noting that once the cell membrane of the first cell was optimally aligned for maximum power delivery, no further care was taken in alignment when moving from cell to the next during photoporation.

The lack of continuous alignment during photoporation illustrates the fact that a high degree of automation has been achieved resulting to a focus and alignment free photoporation. This point and click scheme opens up new prospects in the way we perform optical transfection rendering a user-friendly, non-invasive and highly selective alternative to current cell transfection methodologies.

4.5 Conclusion

The strict requirements for precisely matching the laser focus to the cell membrane during photoporation have compelled us to explore alternatives routes to the highly divergent focused Gaussian beams. Such a route involves the generation of a “non-diffracting” BB for optical transfection. A BB exhibits an elongated focus which has the ability to induce multiphoton effects over a long axial range as opposed to the short and highly confined focal area of a focused Gaussian beam. However, due to the power limitations imposed when using a BB as a result of the dissipation of total power within its off axis lobes, significantly higher input power is required to initiate membrane perforation as opposed to its equivalent in size Gaussian beam.

In this chapter, I introduced the concept of the “focus-free” optical transfection by means of a “non-diffracting” light beam, the BB. An approximation of the ideal “diffraction-

free” BB was experimentally generated by means of an axicon lens which was illuminated by a collimated Gaussian beam. Fs photoporation and optical transfection of CHO cells was performed by means of a BB which propagated without appreciable spreading over twenty times greater distance compared to the Rayleigh range of its corresponding in size Gaussian beam [19]. A comparison of those two approaches was provided in terms of transfection rate, obtained at various locations of the cell membrane along the axial direction of beam propagation. It became evident that Gaussian transfection introduces strict requirements in the positioning the laser focus on the cell membrane due to the multiphoton nature of the pore creation. This results in demanding alignment when delivering a laser dose to each cell in the sample during photoporation. Contrary to the highly divergent nature of a Gaussian beam, a BB acts as an optical syringe retaining its non-spreading profile over a long distance, hence showing the potential of the BB to induce multiphoton processes with minimal alignment requirements. I showed that by using the given BB, optical transfection was achieved over 20 times the axial transfection length compared to the Gaussian beam. By implementing the reconstruction property of the BB, it was also proved that optical transfection of CHO cells was possible through an obstructive layer. This capability paves the way for selective optical transfection through multiple cell layers, turbid media and potentially tissues.

By means of an SLM, the first steps towards automation of the transfection process have been achieved, rendering a very user-friendly tool for life scientists. This work involved generating a BB by means of an axicon lens and subsequently providing phase modulation in the far field spatial spectrum of the BB using an SLM. This arrangement

offered 3D control in the positioning of the BB with respect to the cells. The SLM was LabView driven and interfaced with the computer mouse. With a click of the mouse, the computer controlled BB was appointed on the target cell and the laser dose was delivered. By releasing the mouse key, the laser beam shutter was activated and the beam was blocked. The alignment requirements involved using this approach was truly minimal, allowing for easier and quicker photoporation runs.

This work has proved to be an important step forward, to the way optical transfection of cells is performed. For the first time, a novel light beam such as a BB was implemented for advanced biological studies such as the genetic modification of cells. This novelty for “focus-free” photoporation opens up new prospects for high cell throughput photoporation, with cells being adhered or suspended in a microfluidic environment, as well as photoporation within tissue and turbid biological media. The versatile and alignment free character of the technique, offers the possibility for integration with other optical techniques for more elaborate biological or biomedical studies, all in one microscope based workstation.

References

[1] C.A. McQueen, et al., "*An experiment to study a "nondiffracting" light beam,"* American Journal of Physics **67**(10), p. 912, 1999.

[2] Z. Liu and D. Fan, "*Propagation of pulsed zeroth-order bessel beams,"* Journal of Modern Optics **45**(1), p. 17 1998.

[3] J. Durnin, et al., "*Diffraction-free beams,"* Physical Review Letters **58**(15), p. 1499, 1987.

[4] J. Durnin, "*Exact solutions for nondiffracting beams. I. The scalar theory,"* Journal of Optical Society of America A **4**(4), p. 651, 1987.

[5] D. McGloin and K. Dholakia, "*Bessel beams: diffraction in a new light,"* Contemporary Physics **46**(1), p. 15, 2005.

[6] J.H. McLeod, "*The Axicon: A New Type of Optical Element,"* J. Opt. Soc. Am. **44**(8), p. 592, 1954.

[7] J. Arlt, et al., "*Optical micromanipulation using a Bessel light beam,"* Optics Communications **197**(4-6), p. 239, 2001.

[8] J. Durnin, et al., "*Comparison of Bessel and Gaussian beams,"* Optics Letters **13**(2), p. 79, 1988.

[9] B.P.S. Ahluwalia, et al., "*Microfabricated-composite-hologram-enabled multiple channel longitudinal optical guiding of microparticles in nondiffracting core of a Bessel beam array,"* Applied Physics Letters **87**(8), p. 084104, 2005.

[10] S.H. Tao, et al., "*The generation of an array of nondiffracting beams by a single composite computer generated hologram,"* Journal of Optics A: Pure and Applied Optics 1), p. 40, 2004.

[11] A. Vasara, et al., "*Realization of general nondiffracting beams with computer-generated holograms,"* Journal of Optical Society of America A **6**(11), p. 1748, 1989.

[12] J. Turunen, et al., "*Holographic generation of diffraction-free beams,"* Applied Optics **27**(19), p. 3959, 1988.

[13] V. Garces-Chavez, et al., "*Simultaneous micromanipulation in multiple planes using a self-reconstructing light beam,"* Nature **419**(6903), p. 145, 2002.

[14] O. Brzobohaty, et al., "*High quality quasi-Bessel beam generated by round-tip axicon,"* Optics Express **16**(17), p. 12688, 2008.

[15] D. Stevenson, et al., "*Femtosecond optical transfection of cells: viability and efficiency,"* Optics Express **14**(16), p. 7125, 2006.

[16] T. Cizmar, et al., "*Generation of multiple Bessel beams for a biophotonics workstation,"* Optics Express **16**(18), p. 14024, 2008.

[17] J. Baumgartl, et al., "*Optically mediated particle clearing using Airy wavepackets,"* Nature Photonics **2**(11), p. 675, 2008.

[18] S.H. Tao, et al., "*The generation of an array of nondiffracting beams by a single composite computer generated hologram,"* Journal of Optics A: Pure and Applied Optics 1), p. 40, 2005.

[19] C.T.A. Brown, et al., "*Enhanced operation of femtosecond lasers and applications in cell transfection,"* Journal of Biophotonics **1**(3), p. 1, 2008

Chapter 5

Cellular transfection using an axicon tipped optical fibre

Introduction

In chapters 3 and 4, fs cellular transfection was successfully demonstrated using a tightly focused Gaussian laser beam, as well as implementing a non-spreading BB. The "non-diffracting" character of the BB eliminates the need for precisely locating the cell membrane, essentially offering alignment-free photoporation. However, both of these methods have been restricted to free-space beam propagation whilst using elaborate optical setups and expensive opto-electronic devices such as SLMs.

A novel and simpler alternative to current laser based transfection techniques is the use of an optical fibre for photoporation which will be detailed in this chapter. The fibre based photoporation retains the advantages of the free-space approach such as high spatial selectivity and sterility, whilst decouples from complicated and rather expensive optics thus significantly simplifying the alignment process. For the purposes of photoporation, the optical fibre can be accommodated in any commercially available microscope, potentially eliminating the need for homebuilt imaging and beam focusing systems. Fibre based cellular transfection is a significant step forward with real advantages over standard methodologies, especially the relatively high efficiency and spatial selectivity to be used in vivo. In contrast, viral transfection and electroporation will very likely remain standard

techniques in vitro, due to their ease of use and high throughput.

Fibre based gene delivery comes with considerable advantages over the free space techniques, however a number of challenging issues still remain. These issues are associated with the poor power coupling into a single mode fibre as well as ultra short pulse broadening due to fibre induced phenomena such as group velocity dispersion and self-phase modulation. It would be a challenge to address and truly resolve these issues in particular the latter by means of dispersion compensation.

The use of an optical fibre for photoporation offers a simpler route to the current free space methodologies, opening up prospects for integrating photoporation with endoscopic technology, potentially in a versatile module that could be accommodated in any commercial microscope.

5.1 Axicon tipped fibre fabrication

Optical fibres have become valuable tools in various research areas of Biophotonics. They can be integrated in complex microfluidic environments [1] and substitute complicated and expensive optical systems and potentially be combined with current optical techniques such as for example optical trapping [2], optical sorting and electrophysiology.

Light that exits the cleaved facet of an optical fibre will be naturally divergent. This introduces significant limitations to the utility of optical fibres when a tightly focused beam is required to initiate non-linear processes such as photoporation. A way to

circumvent this problem is to use a microlensed fibre which is a type of fibre specially fabricated to possess a microscopic lens on the cleaved top of its facet. This microscopic lens will act as a focusing lens on the incident laser beam, producing a tight focus in the proximity of the fibre facet [3]. Various techniques have been employed in order to fabricate a lens tipped fibre, such as mechanical polishing[2], heating and drawing the fibre in an electric arc [4] and lithographic techniques that proved laborious and complicated.

As has been discussed already, photoporation requires a tightly focused laser beam to be accurately positioned on the cell membrane. Herein, I will define the distance between the lens tip of the fibre and the cell membrane as the "working distance" of the optical fibre. This distance does not correspond to the peak intensity of the fibre output or any other physical or propagation characteristic of the fibre. It does, however, imply the distance from the cell we wish to work at, as dictated by the given application.

Due to the highly divergent output of the cleaved and some of the conventional lens tipped fibres, it is expected that maximum power intensity will be observed near the fibre facet. Therefore, the optical fibre should be positioned in close proximity to the cells for successful photoporation. This could potentially lead to undesirable physical contact between the cell and the fibre, causing stress on the cell surface and potentially jeopardizing the cell viability. By using an axicon tipped fibre, we are able to position the irradiated cells at a wide range of distances from the fibre tip depending on the experimental requirements. This is possible by simply changing the axicon cone angle through fabrication, in response to how far, or close, we wish to hold the fibre from the

cells.

An inexpensive and simple fabrication process followed during our experiments was selective chemical etching [5, 6]. By chemically etching a commercially available single mode fibre, a conical microlens is formed on its facet, giving rise to a special class of fibre, the axicon tipped fibre [7-9]. Optical fibres consist of silica material that can be chemically etched by a solution that consists of hydrofluoric acid (HF, 48%-51%) and ammonium fluoride (NH_4F, 40%). The fabrication of the axicon tip on the core facet relies on the different etching rate of the cladding and the core of the fibre. The etching rate of the fibre core will be faster or slower than that of the cladding, depending on the volume ratio of the chemicals used, resulting in an inverted or a protruded cone respectively [10]. In our case, the fibre core was etched at a higher rate as opposed to the cladding, therefore giving rise to an inverted cone at the fibre core facet. Figure 1(a) and 1(b) show the chemical etching process of a single mode optical fibre and the side view image of the resulting axicon tipped fibre using an SEM. The base of the resulting axicon cone has the same cross-section area with the fibre core, however the height of the cone and so the apex angle will vary depending on the volume of the chemicals, the etching rate and the temperature of the chemical compound.

The fibre used in this experiment was a commercially available single mode fibre of mode field diameter 5.6 μm, cladding diameter 125 μm, and an operating wavelength of 830 nm (Thorlabs, P1-830A-FC-2). The volume ratio of NH_4F to HF used was 2.1:1 which provides an axicon cone angle of approximately 118 ± 2 °. The cleaved end of the fibre was vertically immersed in the etching solution for 60 minutes at 23° room

temperature and subsequently rinsed with water for 1 minute. The final cladding diameter was measured to be 65.8 ± 1 μm which proved to be sufficient for achieving fibre stability inside the liquid environment of the cell sample.

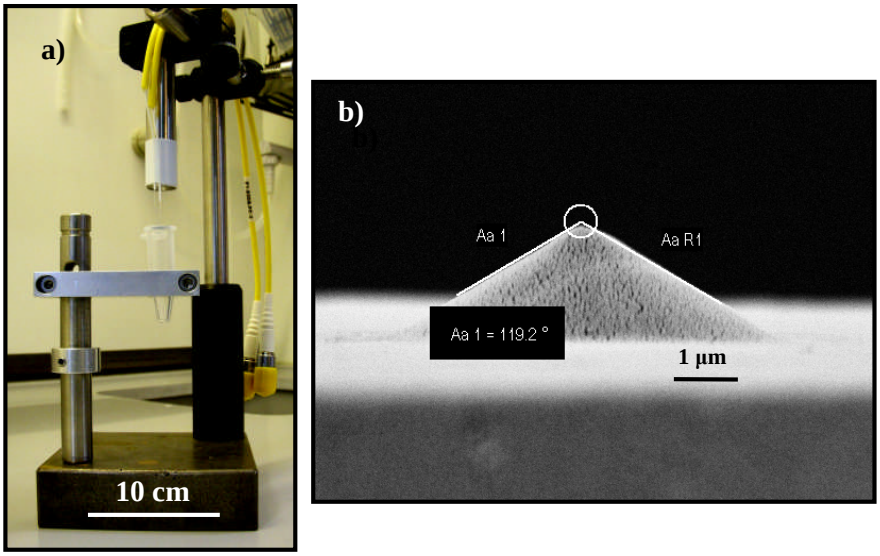

Figure 1: (a) During the chemical etching process, a standard optical fibre is immersed inside a solution comprising NH_4F and HF, in 2.1:1 ratio, for 60 minutes at room temperature 23º. This results in the formation of an inverted cone on the fibre core facet. The fibre cladding will also be etched but a slower rate than the core. (b) The SEM side-view image of the axicon tip of the etched optical fibre, known as the axicon tipped fibre. The conical shape of the tip can be associated with an axicon; however the resulting optical field is far from being a BB.

Although the conical shape of the etched fibre core may be associated and named after the axicon conical lens, the optical field emerging from the fibre tip is far from being a BB. The presence of an axicon on the fibre facet modifies the output such that the subsequent enhanced intensity is sufficient for multiphoton excitation. Considering the very small diameter of the Gaussian beam (~5 μm) illuminating the axicon tip, the axicon tipped fibre does not produce a Bessel mode, rather just an “elongated” focus. This

results in successful cell transfection using the fibre at a relatively remote position to the cell sample, thereby obviating any potential physical contact between the tip and cell sample.

5.2 Theoretical and experimental characterisation of the axicon tipped fibre

The output of the axicon tipped fibre was analysed from a series of images corresponding to its lateral cross-sections obtained in both air and water by means of a long-working distance (Mitutoyo, x100, NA=0.7) and a water immersion objective (Olympus, x60, NA=0.85) respectively, in conjunction with a CCD camera (Basler piA640-210gm). Using a motorized actuator (Newport CMA-12) the fibre facet was displaced from the objective lens in steps of 1.25 μm and at each position an image of the beam cross-section was captured.

In order to compare the experimental findings of the fibre output with those dictated by theory, a mathematical algorithm was developed by my colleague T. Cizmar that predicted the propagation properties of the axicon tipped fibre output. This algorithm was based on the scalar and paraxial free-space propagation approach, where the field in the initial plane on the fibre facet (the fibre mode) is decomposed into a spectrum of plane-waves by FT. The spatial spectrum for any plane behind the fibre is obtained by assigning a correct phase shift to each of the plane wave components and the field is retrieved by IFT. The field evolution inside the axicon tip was monitored in a sequence of small axial steps. In each of these steps, the optical field was split in two components, one

propagating inside and one outside the axicon tip. The composition of those two field components was used as the starting field of the next step. The step size was set to be λ/20. This step size apparently offers a good balance between a good step approximation and minimal accumulative numerical errors rising from large amount of steps during computation.

Figures 2(a) and 2(b) show the theoretical and experimental results of the azimuthally averaged intensity profiles of the beam as a function of the axial distance from the fibre facet, in air and water respectively. The y axis corresponds to the cylindrical coordinate ρ denoting the radial distance from the z axis. The intensity of the fibre field is also depicted, with the parts of highest intensity (on axis) appearing red and the low intensity parts appearing blue. According to the theoretical model, the propagation distance of axicon tipped fibre output with 118º cone angle is approximately 60 μm and the beam radius will increase with axial distance. At a certain axial position within the propagation direction of the beam, an intensity maximum is observed that declines away from that optimum position. The propagation properties of the output field change within water. Both the beam diameter and the propagation distance will increase, as evident by figure 2. The experimental findings are in good agreement with the theoretical predictions.

Through fabrication, we can selectively vary the axicon tip cone angle. This will have a direct impact to the propagation properties of the fibre output and hence to the axial position of the observed intensity maximum.

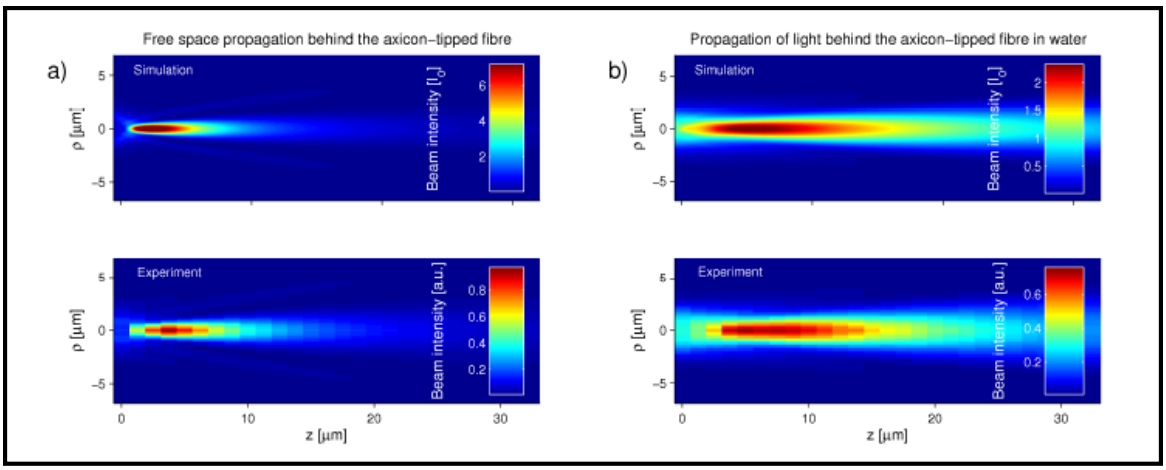

Figure 2: The theoretical and experimental (a) free-space and (b) in water propagation of the optical field emerging from axicon tipped fibre. The y axis corresponds to cylindrical coordinate ρ denoting the radial distance from the z axis, and z corresponds to the axial distance along the z axis. The coloured column on the right hand side of each image indicates the beam intensity, with I_0 being the on-axis intensity of the fibre output. It can be clearly seen that the propagation distance of the fibre output in water is elongated compared to its free-space counterpart. Experimental and theoretical findings are in good agreement.

In other words by varying the cone angle, we are able to control how far or close to the axicon tip, and therefore to the irradiated cells, we will be able to operate during photoporation.

For the purposes of photoporation, we are interested in using an optical fibre which offers a good compromise between power delivery and working distance. In order to ascertain the ideal parameters, in terms of working distance and intensity maximum for the optimum axicon tipped fibre, we used the above described algorithm and varied the cone angle of the simulated axicon tipped fibre. The cone angle of the axicon tip is the only parameter we can vary in the model, considering the fixed parameters of a single mode

optical fibre.

Figure 3(a) shows the variation in working distance with the cone angle of the axicon tipped fibre. For each axicon tipped fibre, of a certain cone angle, there is an associated working distance at which the intensity is higher than that achieved by any other axicon fibre of different cone angle. If it is required, for example, that the sample is to be held at distance approximately 30 μm away from the fibre, then the optimum (intensity wise) axicon tipped fibre should have apex tip angle of 100º. An axicon tipped fibre of 118º cone angle would be the optimum (intensity wise) axicon tipped fibre to work at approximately 45 μm from the cells *compared to any of the other axicon tipped fibres*, however, that distance does not correspond to the peak intensity of the fibre output, therefore during this experiment the working distance of the fibre was shorter.

The next step in the quest for the optimum axicon tipped fibre for photoporation is to investigate the relation between the axicon cone angle and peak intensity. Figure 3(b) shows the variation in peak intensity obtained at a range of working distances which are optimum at a given cone angle. From this graph, it becomes evident that an increase in working distance, in response to an increase in cone angle, is accompanied by an exponential decrease in the attainable peak intensity. This implies that in order to achieve high intensity at the irradiation site during photoporation, an axicon tipped fibre of a very short working distance should be fabricated, however, that will be at the expense of the safety margin between fibre tip and cell membrane. By decreasing this safety margin, undesirable physical contact between fibre and cells may occur, leading to erroneous transfection efficiencies due to accidental membrane injection, or even

irreversible cell damage.

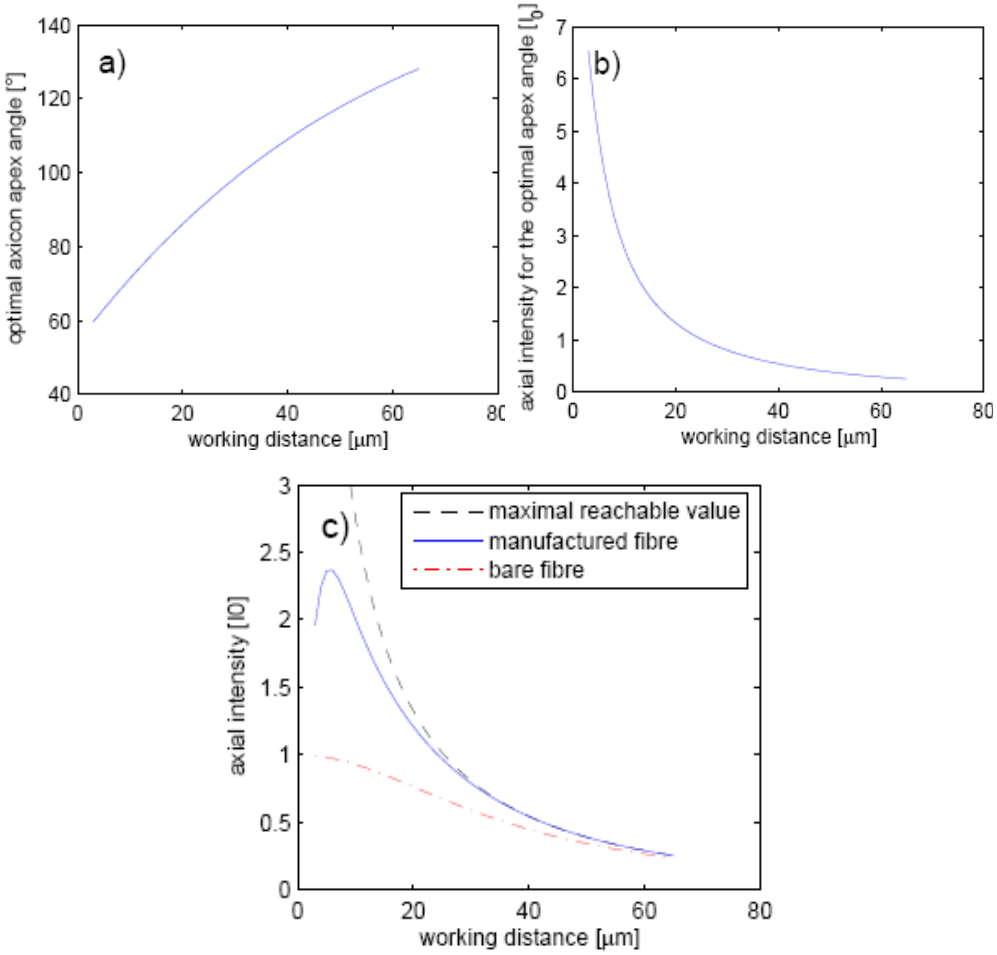

Figure 3: (a) Working distance variation of an axicon tipped fibre with cone angle. The wider the apex angle of the conical tip, the longer the attainable working distance. (b) The peak axial intensity at each of the working distances (which correspond to a different cone angle). An axicon tipped fibre of working distance below 5 µm will give the highest peak intensity at the irradiation site; however such a short working distance will have significant implications to the cell viability during experiments. (c) Comparison of the on-axis intensity of the fabricated fibre with the maximal achievable intensity for the optimal fibre (Fig. 2(b)) and the bare-tipped fibre.

Figure 3(c) compares the axial intensity achieved by the axicon tipped fibre used in our experiments and a standard bare tip fibre as well as the maximum attainable axial

intensity as dictated by figure 3(b). In the case of a bare tip fibre, the available working distance is approximately 60 μm as well as in the case of the fabricated axicon tipped fibre of cone angle 118º. However the maximum attainable intensity achieved by the bare tip fibre is significantly lower than that of the fabricated fibre. As shown in figure 3(c), the maximum attainable intensity of the fabricated fibre is obtained at 13 μm from the axicon tip, with the overall intensity tailing off away from that position.

According to figures 3(b) and 3(c), an axicon tipped fibre of 75º apex angle would have been the optimum fibre to use at 13 μm working distance in terms of intensity, since the peak intensity is higher than that obtained using the fabricated fibre at that axial distance. However, the intensity tails off much quicker decreasing the overall working distance available for photoporation. By choosing an axicon tipped fibre of cone angle 118º, we achieve good balance between working distance and peak intensity. In addition, it should be remarked that the choice of a 118º offers ease in fabrication and better reproducibility as opposed to other cone angles.

This chapter section gives a good insight into the properties of an axicon tipped fibre as well as the restrictions imposed by the photoporation experiment to its use. In the following section, I am detailing the experimental procedure of fibre based photoporation and the cell preparation protocol.

5.3 Experimental process

5.3.1 Experimental setup

As in the case of photoporation studies using the free space Gaussian and Bessel beams, the laser source used herein was the Ti: Sapphire oscillator, with parameters discussed in chapter 3 and 4. Phenomena such as GVD and SPM occurring inside the optical fibre in the presence of ultra-short pulses resulted in stretching of the temporal and spectral profile of the laser pulses at the fibre exit. The pulse duration was measured using two methods. The first method involved using the home built intensity autocorrelator as mentioned in chapter 3. At the time of the autocorrelation measurement, the pulse duration of the laser pulses before entering and upon exiting the axicon tipped fibre was determined in the absence of an optical isolator in the beam path.

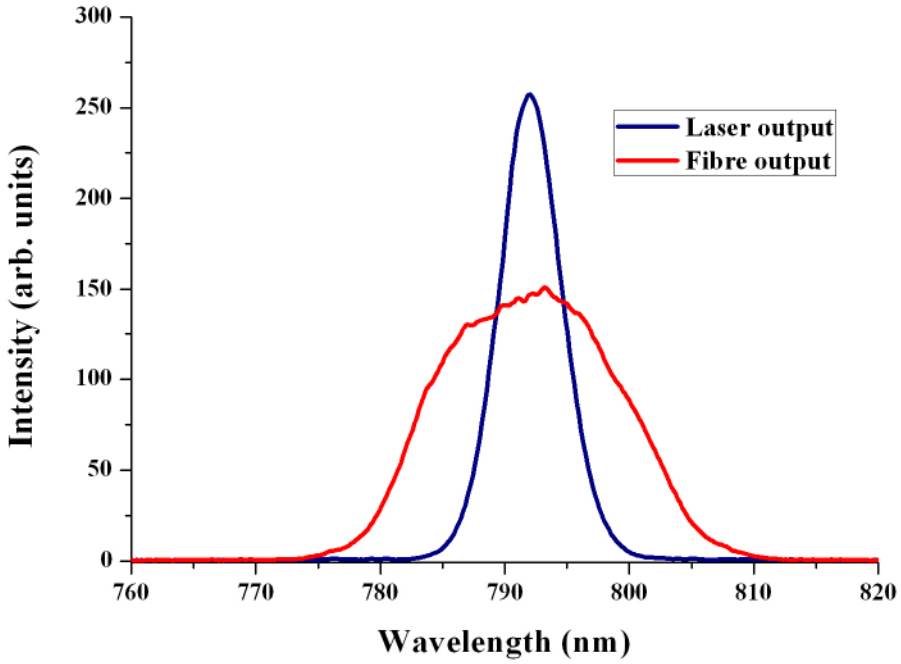

Figure 4: The spectrum of the Ti: Sapphire generated laser pulses before entering and upon exiting the axicon tipped fibre. Due to GVD and non-linear effects such as SPM the spectrum of the 141 fs duration laser pulses is significantly affected upon traversing the 35 cm fibre. This results into broadening of the spectrum as well as an associated temporal stretching in the pulse duration approximately by a factor of 9.

However, over the course of the experiment, an optical isolator was used to eliminate disruption of the mode-locking laser operation due to back-reflections from the optical fibre.

The pulse duration of the pulses entering the optical fibre was determined to be 113 ± 10fs and upon travelling through the 35 cm long axicon tipped fibre was measured to be 800 ± 10 fs assuming sech^2 shape pulses. The same measurement was repeated using a commercially available intensity autocorrelator, in the presence of an optical isolator in the beam path (Femtochrome). The pulse duration of the incident laser pulses passing through the fibre was measured to be 141 ± 10 fs. The fibre output was collimated using an aspheric lens of 4.25 mm focal length and was subsequently directed to the Femtochrome intensity autocorrelator. The measured pulse duration was now determined to be 1.29 ± 0.15 ps, assuming sech^2 shape pulses. The spectrum of the laser pulses before and after the passage through the fibre is shown in figure 4.

The experimental setup used was built around a NIKON microscope (model TE-2000U) as shown in figure 5(a). A 1.6x magnifying telescope, consisting of two planoconvex lenses F_1 and F_2 of focal lengths 100 mm and 160 mm, expanded the incoming laser beam which was subsequently coupled to the 35 cm long axicon tipped fibre, using a fibre collimator (THORLABS, F810FC-780). The mirrors M_1, M_2 and M_3, which were used to redirect the laser beam, were dielectric mirrors layered with coating to minimize NIR reflections. The coupling efficiency of the fibre collimator-optical fibre system was measured to be 27%. The fibre output power was adjusted by means of an ND filter

wheel appropriately placed in the beam path. During photoporation the average power of the beam was kept equal to 110 mW, with peak power per pulse equal to 1.06 ± 0.38 kW.

A mechanical shutter (Newport, 845HP-02) was also positioned close to the laser output and controlled the time duration of the laser dosage on the cell membrane. Each cell was irradiated with three laser doses. The duration of each dose was experimentally determined to be 80 ms. The number of the laser doses was experimentally determined to be the most successful number of doses in conjunction with the dose duration of 80 ms. While irradiating the cells, a slight adjustment ($\pm 1\mu m$) of the laser focus took place to ensure that we achieve maximum power delivery on the cell membrane. Three laser doses were used ensuring consistency of irradiation for all cells and indeed this is aligned with the number of doses used in previous work [11].

The fibre was mounted on a three axis, XYZ translation stage and was carefully inserted into the medium, as shown in figure 5(b). Due to restrictions imposed by the geometry of the hosting microscope, the fibre could not be accommodated vertically between the sample stage and the microscope condenser, as the imaging path was disrupted. A protractor enabled the adjustment of the fibre orientation with respect to the lateral plane. Figure 6 shows part of the experimental setup whereby the axicon tipped fibre has been supported on an XYZ translation stage and inserted into the cell sample. The cell culture dish is located on the microscope sample stage.

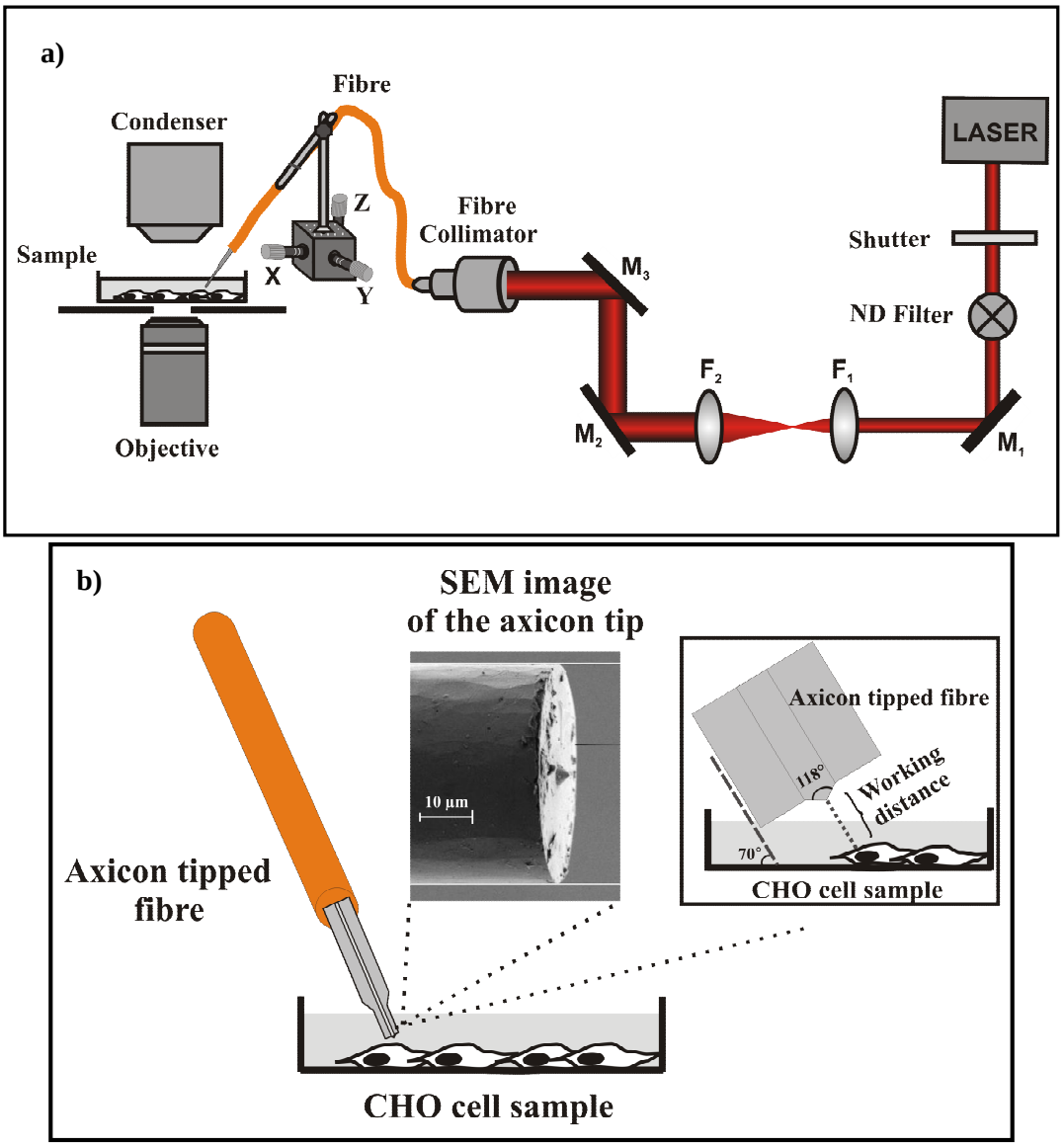

Figure 5: (a) Optical setup for axicon tipped fibre photoporation. The laser beam coming out of the Ti: sapphire oscillator is expanded upon passing through a 1.6x magnifying telescope, consisting of two lenses F_1 and F_2 of focal lengths 100mm and 160mm respectively, and is subsequently illuminating the fibre collimator. The light is then coupled into the axicon fibre which is hosted into a NIKON microscope. (b) The fibre is inserted at an angle of 70º into the cell sample dish and photoporation takes place. The side SEM image of the etched axicon tip and fibre cladding is also presented. The fibre is positioned at approximately 13 µm from the cell membrane. The fibre is inserted into the cell sample at 70º with respect to the sample dish.

When the fibre was positioned at angles below 50° with respect to the lateral plane, the beam could not reach the cell membrane and permit successful transfection. At a 60° angle, the laser beam could only reach and perforate the most rounded shaped cells, whereas the cells which appeared more flat remained out of reach. At angles of 80° and 90° the fibre obstructed the imaging path, hence preventing the direct observation of the photoporation process.

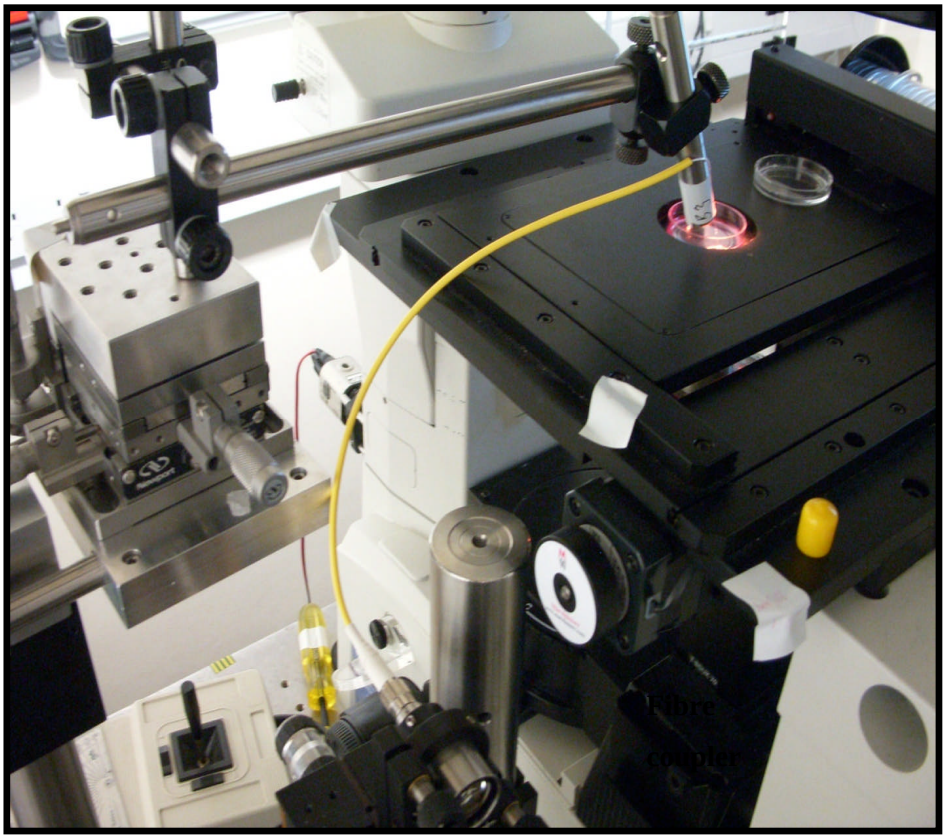

Figure 6: Image of the axicon tipped fibre supported on an XYZ translation stage. During photoporation, the optical fibre is inserted into the sampe dish which is located on the NIKON microscope sample stage.

The optimum angle for photoporation using an axicon tipped fibre was established to be 70° for all cells regardless of their shape. The experimental error associated with the

measurement of the angles was $\pm 1^{o}$. The minimum distance that was physically achieved between the fibre and the cells, without the fibre cladding coming in contact with the sample dish bottom was 13 ± 0.2 μm. It should be noted that the reduction in the fibre cladding diameter as a result of chemical etching, brings a significant benefit here, since such a short working distance would not be achievable with the original bare fibre considering the current geometry.

Considering the limitations emerging from the positioning of the beam at 70^{o} with respect to the bottom of the dish, the calculated axial distance between the axicon tip and the dish surface is approximately 13 ± 1 μm. For a round cell we assume thickness of approximately (4 ± 1) μm so we adjusted the z-actuator of the XYZ translation stage by approximately 4 μm, in order to position the cell at 13 μm with respect to the fibre tip. When the cell is flat and we photoporate near the edge and assume a thickness of approximately (2 ± 1) μm and as such we adjusted the z-actuator by (2 ± 1) μm from its initial position.

5.3.2 Sample preparation protocol

The cell preparation was performed according to the protocol described in chapter 3, section 3.2.3. During this set of experiments, no coverslip was floated on the liquid environment of the cell sample as that would have prevented the fibre entrance to the sample. During laser irradiation, no visible response of the cells to the laser irradiation was noticed i.e. no long-lasting bubble formation occurred upon laser irradiation.

In order to take into account any spontaneous transfection occurring within the irradiated cell sample, two different types of control dishes were prepared. The first set of controls involved six cell dishes, prepared according to the photoporation protocol i.e. cells exposed to plasmid DNA but not laser irradiation, and were kept in the cell culture hood whilst photoporation was taking place. The number of spontaneously transfected cells observed was between 0 and 3. The second set of controls involved also six control dishes, prepared according to the photoporation protocol i.e. cells exposed to plasmid DNA, in the absence of laser exposure, but this time in the presence of an axicon tipped fibre. This way, I could ascertain whether the physical presence of the optical fibre would have any impact on the viability as well as on the spontaneous transfection rate. No spontaneously transfected cells observed in this set of controls.

In the next section, I am presenting the results obtained using the axicon tipped fibre for photoporation of CHO cells, followed by a discussion concerning these results and the importance of the work reported herein.

5.4 Results

In the course of this experiment, a total number of six sample dishes were laser treated (N=6) and in each dish 25 cells were photoporated giving a total number of 150 CHO cells photoporated. Figure 7(a) shows the axicon tipped fibre in the presence of CHO cells during photoporation. The fibre was inserted into the cell sample, at an angle of approximately 70º with respect to the dish bottom. For alignment purposes, first I made sure the fibre cladding was in contact with the dish bottom, with care taken not to bend

the fragile fibre. Depending on the shape (round or flat cell edges) of the targeted cell, I increased the height of the fibre by approximately 4 μm or 1 μm respectively. Figure 7(b) shows the successfully transfected cells which expressed the red fluorescent protein, DS-Red. As in our previous studies, the transfection rate was defined to be the number of successfully transfected cells observed 48h upon laser irradiation over the total number of photoporated cells at 0 h (during the experiment). The transfection rate observed between the irradiated dishes varied between 25% and 57%. Herein, the transfection rate coincides with the viability percentage as all fluorescent cells observed were viable.

It should be noted that the transfection rate is expected to vary between dishes, as there are a number of unavoidable factors that may vary and influence each experimental run.

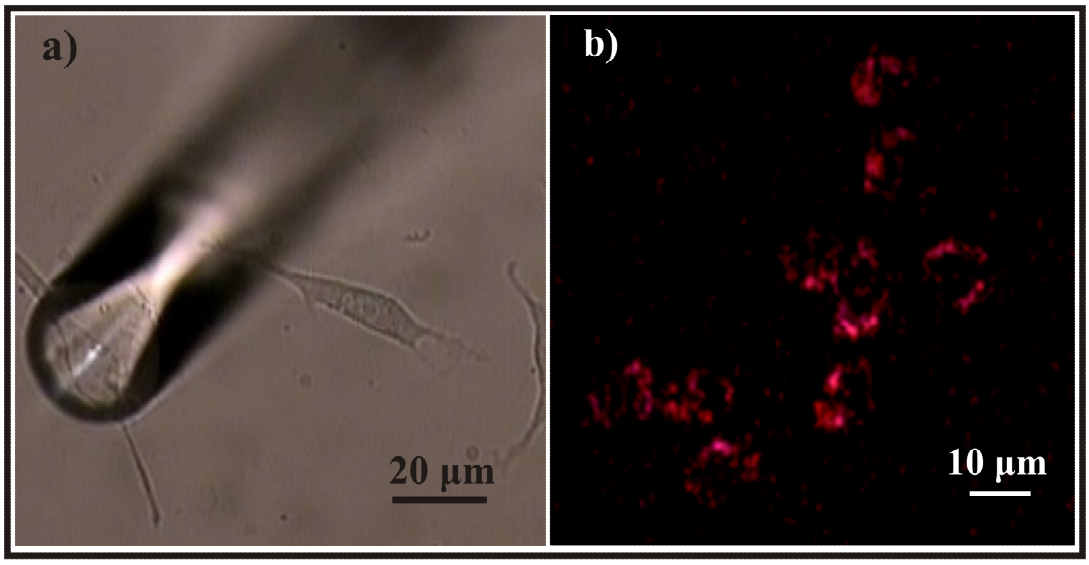

Figure 7: Photoporation and transfection of CHO cells using an axicon tipped optical fibre. (a) The fibre is inserted into the cell sample at a 70º angle with respect to the dish bottom. Each cell is exposed to three laser doses of 40 ms duration. The total number of cells per dish was 25. (b) Fibre transfected CHO cells expressing the red fluorescent protein DS-Red. The transfection rate observed varied from 25% to 57% between the treated dishes.

These factors include the fibre quality degrading with experimental runs, the small variation in the cone angle (2º - 3º) amongst the fabricated axicon tipped fibres, the status of the cultured cells as well as the experimental errors associated with positioning the fibre with respect to the cell membrane.

5.5 Conclusion

In this chapter, I have shown successful photoporation and transfection of CHO cells by means of an axicon tipped fibre at transfection rates that compare favourably to the free-space approaches. This can be considered an important piece of work as it offers a new perspective to the way cell photoporation has been performed so far. Such methodology has the potential to be applied in tissue transfection, whereby cells of different type and topography within the tissue can be irradiated by means of a single optical fibre hosted on a microscope. Phenomena such as GVD and SPM which affect the temporal and spectral profile of the fibre delivered laser pulses have not been addressed during this study. However, the attempt to compensate for the induced pulse broadening is part of ongoing work which will be discussed in chapter 7. It would be a considerable advance to perform dispersion compensation of the axicon tipped fibre and subsequently perform photoporation of cells or tissue.

In terms of future work, it would be of great interest to fabricate other types of lensed optical fibres such as parabolic tipped or pencil shaped optical fibres [4, 5] and draw a comparison between those and the axicon tipped fibre, in terms of photoporation. This study would allow assessing suitability of each optical fibre for photoporation in terms of

the output field profile, efficiency in power delivery versus working distance and transfection efficiency.

As a significant step forward, one could envisage the development of an optical endoscope composed of multiple fibres for simultaneous sample illumination, light delivery for photoporation and multiphoton fluorescence detection for advanced in vivo transfection studies. This could be potentially proved particularly useful for studying the function and behaviour of neurons within a remote living specimen, by selectively targeting individual neurons within a large cell population. The optical fibre approach for photoporation could potentially become commercially available module that could be integrated into any commercially available microscope for routine optical transfection studies in cells and tissues.

References

[1] K. Metzger, "PhD thesis: Longitudinal optical binding", Supervisor: K. Dholakia, (2008), School of Physics & Astronomy, University of St Andrews

[2] K. Taguchi, et al., "*Optical trapping of dielectric particle and biological cell using optical fibre,"* Electronics Letters **33**(5), p. 413, 1997.

[3] G. Knoner, et al., "*Optical force field mapping in microdevices,"* Lab on a Chip **6**(12), p. 1545, 2006.

[4] Z.H. Liu, et al., "*Tapered fiber optical tweezers for microscopic particle trapping: fabrication and application,"* Optics Express **14**(25), p. 12510, 2006.

[5] S. Mononobe and M. Ohtsu, "*Fabrication of a pencil-shaped fiber probe for near-field optics by selective chemical etching,"* Journal of Lightwave Technology

14(10), p. 2231, 1996.

[6] Y.J. Yu, et al., "*Focusing characteristics of optical fiber axicon microlens for near-field spectroscopy: Dependence of tip apex angle,"* Optics Communications **267**(1), p. 264, 2006.

[7] T. Grosjean, et al., "*Fiber microaxicons fabricated by a polishing technique for the generation of Bessel-like beams,"* Applied Optics **46**(33), p. 8061, 2007.

[8] S.K. Eah, et al., "*Nearly diffraction-limited focusing of a fiber axicon microlens,"* Review of Scientific Instruments **74**(11), p. 4969, 2003.

[9] S.K. Eah, et al., "*Plasmon scattering from a single gold nanoparticle collected through an optical fiber,"* Applied Physics Letters **86**(3), 2005.

[10] G. Eisenstein and D. Vitello, "*Chemically etched conical microlenses for coupling single-mode lasers into single-mode fibers,"* Appl. Opt. **21**(19), p. 3470, 1982.

[11] X. Tsampoula, et al., "*Femtosecond cellular transfection using a non-diffracting light beam,"* Applied Physics Letters **91**(5), p. 52007, 2007.

Chapter 6

Towards dispersion measurement and pre-compensation in photoporation optical systems using Multiphoton Intrapulse Interference Phase Scan (MIIPS)

Introduction

In the work described so far, optical transfection of cells was described in terms of delivering 100 fs laser pulses to cells through free space microscope optics and an axicon tipped optical fibre, neglecting the effects of dispersion induced by the various optical elements on the propagating pulses. In this chapter, I explore the idea of implementing ultra-short pulses of sub-20 fs duration in order to perform photoporation. The very short time bandwidth of these pulses, allows for significantly higher peak power to be obtained per pulse, even at low average power. This may prove particularly beneficial when performing photoporation as the required average power to initiate pore formation on the cell membrane is expected to be significantly reduced limiting the risk of cell damage. In addition, by operating with low average power, accumulating heating effects may be prevented and the spatial extend of the laser-induced pore may be decreased further. This could ultimately lead to higher transfection efficiencies through a minimally invasive photoporation process. However, sub-20 fs laser pulses come with a very broad spectral

range and are therefore particularly prone to dispersive effects. It thus becomes evident that the ability to measure and subsequently cancel the dispersive phenomena that affect sub-20 fs pulses traversing microscope optics would be advantageous for biological studies.

This section will be devoted to preliminary results obtained as part of my ongoing work on dispersion measurement and pre-compensation in microscope systems and optical fibres. In this chapter, I discuss the propagation of 12 fs laser pulses through a state-of-the-art pulse shaper and subsequently through the optics of a Gaussian photoporation setup, and the dispersion measurements and compensation performed. Dispersion measurement and pre-compensation in an axicon tipped fibre was also achieved. In both cases, the duration of the compensated laser pulses obtained was below 20 fs. Measurements and pre-compensation of phase distortions induced by the microscope optics and optical fibre were achieved by means of a pulse shaper which was based on an SLM that measures and cancels all orders of dispersion through a method known as MIIPS.

The first attempt towards sub-20 fs photoporation of cells has been reported using a set of dispersive mirrors within the laser cavity to provide dispersion pre-compensation in combination with autocorrelation techniques to measure the pulse duration at the cell sample [1]. Contrary to this, the MIIPS pulse shaper is a single beam technique that does not require overlapping of beams and interferometry, is highly reproducible and accurate. Most importantly, it can be used for dynamically tailoring the spectral phase of ultra-short pulses by phase modulating ultra-short pulses, thus tailoring at will their spectral

and temporal properties according to the specific application.

In the context of biomedical imaging, the merits of broadband, phase shaped ultra-short pulses are also apparent. Phase shaping of sub-20 fs pulses can allow selective two-photon activation of chromophores or fluorescent nanoparticles embedded in a biological sample in the absence of photobleaching and sample damage [2-4]. In addition, by controlling the spectral phase of an ultra-short pulse, coherent control can be achieved in molecular systems. For example, the use of a broadband laser pulse of particular spectral phase can induce highly efficient population transfer between electronic energy states within a molecular system [5].

The section that follows describes in brief the most important dispersive effects affecting ultra-short pulses upon travelling through optical glass elements and optical fibres.

6.1 Dispersive phenomena in microscope systems and optical fibres

In recent years rapid progress has been witnessed in the design and development of ultra-fast laser systems capable of emitting light pulses of durations as short as a few attoseconds [6]. Ultra-fast lasers with pulse durations as low as 10 fs are commercially available, however their potential is difficult to be realised due to the effects of dispersion.

The time bandwidth, τ_{TL}, of an ultra-short pulse can be correlated to its FWHM frequency bandwidth, Δv, by using the following expression:

$$\Delta\nu = 0.44 / \tau_{TL} \tag{6.1}$$

According to the above equation, the shorter the pulse in time, the higher the number of frequencies it carries [7]. A TL pulse is known to have the minimum attainable pulse duration for a given bandwidth and envelope shape. A typical Ti: Sapphire oscillator emitting 100 fs Gaussian pulses has a frequency bandwidth of several THz. However, in the case of a Ti: Sapphire oscillator emitting sub-20 fs pulses, such as the one used here, the frequency bandwidth increases to 80-100 THz.

When an ultra-short pulse propagates through a dispersive medium, various linear and non-linear dispersive phenomena will influence its temporal and spectral profile. Most commonly, second order chromatic dispersion in the form of GVD has severe impact on the temporal profile of the pulse resulting in temporal broadening also known as the chirp of the pulse. In response to the dispersion induced temporal broadening, the peak intensity of the pulse will decrease, since the total pulse energy is now distributed over a longer temporal range. Such behaviour is depicted in figure 1. For the calculations in figure 1, maximum peak intensity corresponded to a TL pulse of 12 fs duration. Upon exposure to second order GVD, of various chirp parameters "a" (measured in fs^2), the corresponding peak intensity of the chirped pulse was calculated and it can be shown that is inversely proportional to its broadened FWHM time bandwidth.

In the absence of GVD, a TL Gaussian pulse can be described by a Gaussian shaped envelope with phase that is constant and does not vary with time. Such a pulse can be described as [7]:

$$E(t) = E_0 \exp(-t^2 / \tau^2) \tag{6.2}$$

where $I_0 = |E_0|^2$ corresponds to the peak intensity of the Gaussian intensity profile of the pulse and τ is a constant that can be shown (using equation (6.2)) to be equal to $0.85\,\tau_{TL}$, where τ_{TL} corresponds to the FWHM pulse duration of a TL pulse. By obtaining the FT of the equation (6.2), a TL pulse can be described in terms of its angular frequency ω:

$$E(\omega) \propto \exp(-\frac{\omega^2\tau^2}{4}) \tag{6.3}$$

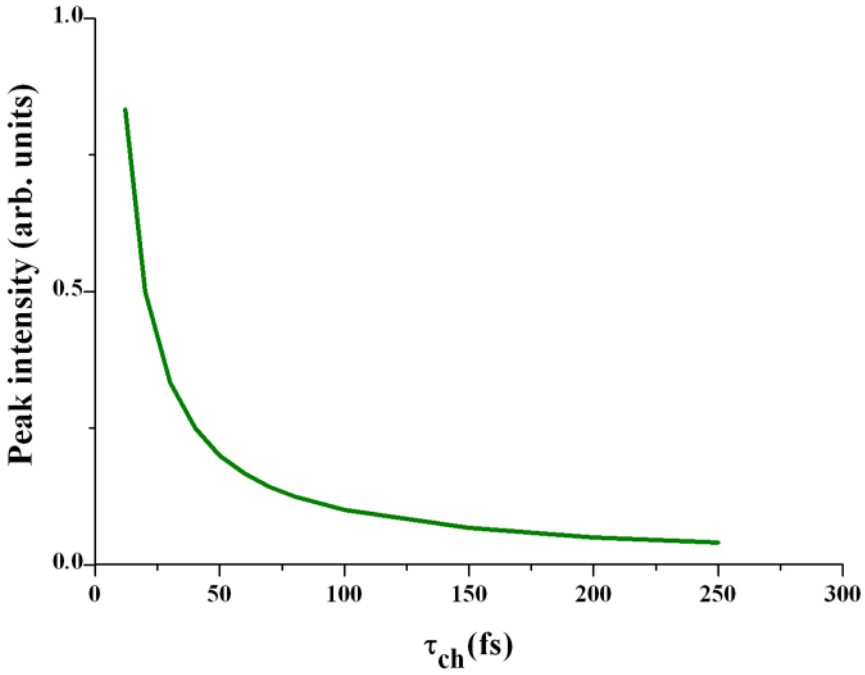

Figure 1: Peak intensity versus FWHM time bandwidth of a TL chirped pulse for various chirp parameters "a". As evident, the peak intensity is maximum for TL pulses (12 fs). However, a chirped pulse is significantly broadened and the peak intensity rapidly decreases for pulse durations up to 70-100 fs. For pulses longer than 70 fs the effect of chirp does not cause significant decrease in the peak intensity. For pulses, with duration greater than 100 fs, the variation in peak intensity is trivial.

When the pulse interacts with dispersive media such as glass optical elements (and to a

lesser extent air and water) equation (6.3) can be expressed as:

$$E(\omega) \propto \exp(\frac{-\omega^2\tau^2}{4})\exp(ia\omega^2) \tag{6.4}$$

The IFT of the above equation will yield the time dependent electric field that describes a chirped Gaussian pulse as follows:

$$E(t) \propto \exp(-\frac{it^2}{4a+i\tau^2}) = \exp(-\frac{t^2\tau^2}{16a^2+\tau^4} - i\frac{4at^2}{16a^2+\tau^4}) \tag{6.5}$$

The phase of the chirped pulse is a quadratic function of time, $\frac{4at^2}{16a^2+\tau^4}$, where a is the chirp parameter in fs^2. The instantaneous angular frequency within the pulse envelope is given as:

$$\omega_i = \frac{d\varphi}{dt} = \omega_0 + \frac{8at}{16a^2+\tau^4} \tag{6.6}$$

where ω_0 is the central angular frequency of the pulse. The frequency appears to be a linear function of time and the pulse is therefore termed linearly-chirped as opposed to a quadratic chirped pulse where the frequency is a cubic function of time.

The effect of GVD is more pronounced for ultra-short pulses (10's of fs) as opposed to longer pulses, due to their increased spectral bandwidth. The FWHM time bandwidth of a TL pulse, τ_{TL}, can be correlated with the FWHM time bandwidth of a chirped pulse, τ_{ch} (using the equation (6.5)) as:

$$\tau_{ch} = \tau_{TL}\sqrt{1+\frac{16a^2}{\tau_{TL}{}^4}} \tag{6.7}$$

Figure 2 shows the effect of second order dispersion on TL pulses for different values of the chirp parameter a= $1000\,fs^2$, $5000\ fs^2$ and $7000\,fs^2$. It is evident that for very short pulses (below 30 fs) and for a given "a", the temporal broadening is very dramatic as opposed to longer duration pulses, for which the effect of GVD is not that significant. The more optical elements the pulse travels through, i.e. high values of the chirp parameter "a", the greater the temporal stretching of the shorter pulses, which is in contrast to longer pulses that are not considerably affected.

In the normal dispersion regime, the speed of the longer (red) wavelength components is greater than the speed of those with shorter (blue) wavelength, giving rise to a positively chirped pulse. As discussed above, assuming a Gaussian pulse envelope, the shape of this envelope is normally unchanged upon second order GVD.

In the presence of third order or higher order GVD, the temporal shape of the pulses will change in a way that the pulse width becomes asymmetric and normally oscillatory around its edges [8]. Figure 3 shows the effects of a GVD and TOD in a TL pulse. Dispersion induced temporal broadening, due to the frequency dependent refractive index n(ω), is also present inside non-linear media such as optical fibres. The frequency dependent refractive index can be expressed by the Sellmeier equation:

$$n^2(\omega) = 1+\sum_{j=1}^{m}\frac{B_j\omega^2{}_j}{\omega_j^2-\omega^2} \tag{6.8}$$

where ω_j is the characteristic resonance frequency at which the bound electrons of a material absorb the electromagnetic energy upon their interaction with the input pulse and oscillate. B_j corresponds to the strength of the jth resonance, with m being the total number of material resonances in response to the light frequencies [8].

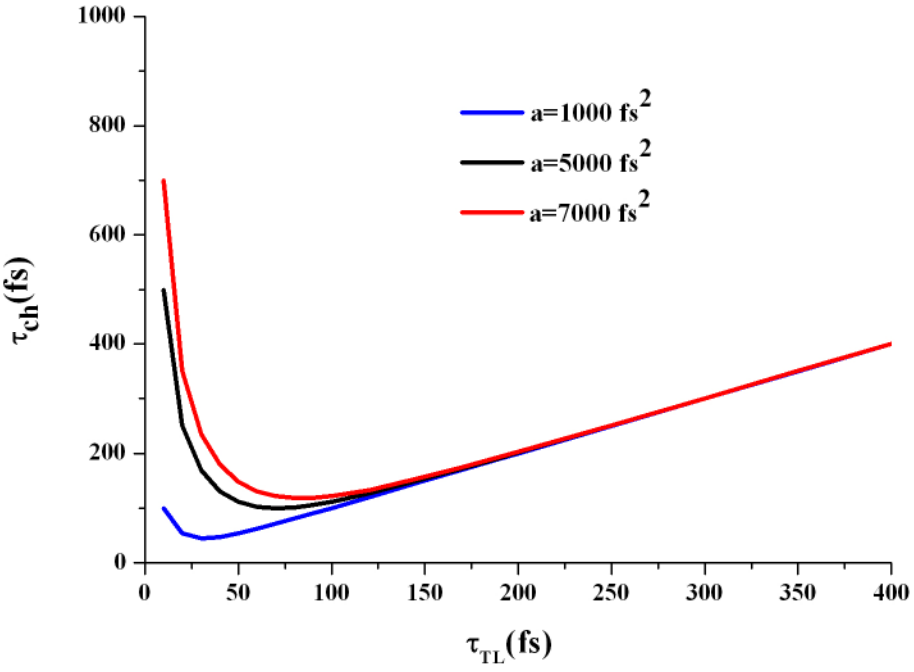

Figure 2: Output pulse duration as a function of input pulse duration, as a result of the influence of GVD on ultra-short pulses traversing an optical element of chirp coefficient a=1000, 5000, and 7000 fs^2. It is evident that as the amount of second order GVD increases, pulses of shorter duration (below 30 fs) will broaden drastically as opposed to longer pulses (above 100 fs), where the temporal broadening is relatively insignificant. At a given GVD value, the effect of dispersion to the time bandwidth of the pulse is far more dramatic than for the longer pulses.

Material dispersion within optical fibres can be expressed in terms of the Taylor expansion of the mode-propagation constant β within an optical fibre core as:

$$\beta(\omega) = n(\omega)\frac{\omega}{c} = \beta_0 + \beta_1(\omega - \omega_0) + \frac{1}{2!}\beta_2(\omega - \omega_0)^2 + \ldots \qquad (6.9)$$

where β_0 is a constant phase shift and β_1 is given as:

$$\beta_1 = \frac{1}{\upsilon_g} = \left(\frac{d\beta}{d\omega}\right)_{\omega_0} = \frac{1}{c}\left(n + \omega\frac{dn}{d\omega}\right) \qquad (6.10)$$

which is the first order derivative of the propagation constant and corresponds to the inverse of the group velocity, the speed at which the pulse envelope propagates within the fibre. The second order derivative of the propagation constant can be expressed as:

$$\beta_2 = \frac{1}{c}\left(2\frac{dn}{d\omega} + \omega\frac{d^2n}{d\omega^2}\right) \qquad (6.11)$$

which gives an expression for the GVD and accounts for the pulse temporal broadening upon its propagation through an optical fibre of a certain length. In addition to material dispersion, waveguide and polarisation dispersion may contribute to the total chromatic dispersion within the fibre.

Apart from linear dispersive effects, the high peak powers exhibited by ultra-short pulses may result in a number of intensity dependent, non-linear dispersive phenomena, the most important of all being the intensity dependent refractive index. Upon the propagation of an intense optical field such as the one that describes ultra-short pulses

through a medium, the pulse itself will induce intensity dependent changes in the refractive index of the medium; a phenomenon known as the optical Kerr effect.

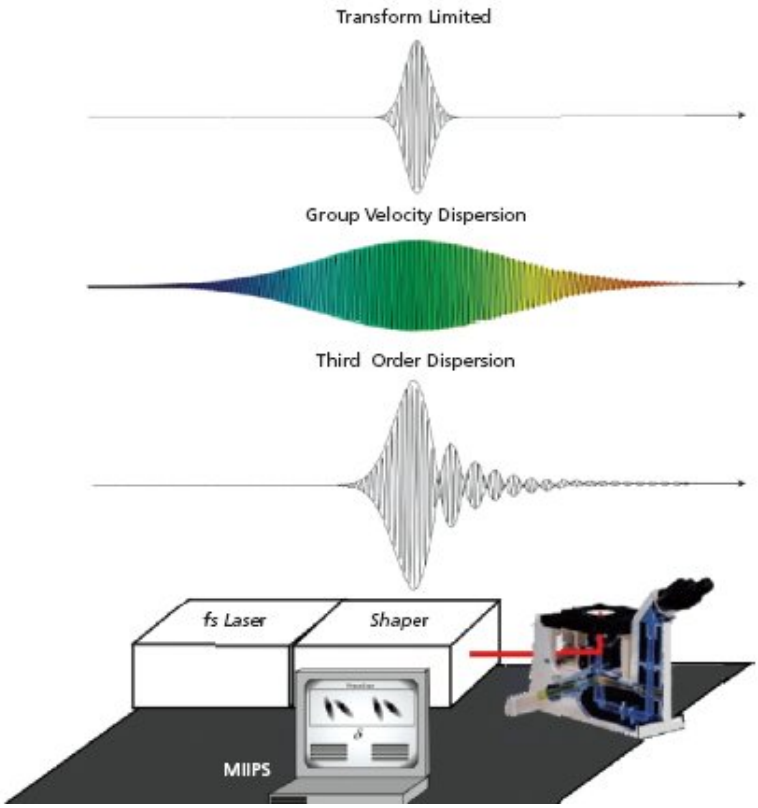

Figure 3: A TL ultra-short pulse is temporally broadened whilst maintaining its shape due to GVD whereby its lower frequency components traverse faster through a normally dispersive medium as opposed to its higher frequency components that are time delayed. TOD results in both temporal stretching and shape distortions. In order to recover the TL pulse, a pulse shaper is accommodated between the microscope optics and the laser source. The former is an SLM based shaper and by means of the MIIPS method, measures and subsequently adds the opposite phase function to deliver TL pulses at the sample [9].

The refractive index will then be described as:

$$n = n_0 + n_k I \tag{6.12}$$

where n_0 is the first order refractive index of the medium in the absence of strong optical fields and n_k is the Kerr coefficient given as:

$$n_k = \frac{6\chi_3}{8\varepsilon_0 c n_0} \tag{6.13}$$

where χ_3 is the third order electric susceptibility of the medium, ε_0 and c are the permittivity and speed of light in vacuum respectively [10]. One of the results of this effect is SPM, during which different parts of the pulse will experience different refractive indices in response to the variation in intensity when moving across the time profile of the pulse. Such an intensity variation will give rise to a time varying refractive index. In response to this, each of the frequencies of the pulse will undergo a positive phase shift whereby the leading edge of the pulse will shift towards the lower (red) frequencies and the trailing edge of the pulse will shift towards the higher (blue) frequencies. SPM results in the generation of more frequencies hence in a broader spectrum. Such phase shifts can be expressed as:

$$\varphi(t) = \omega_0 t - \frac{2\pi}{\lambda_0} n(I(t))L \tag{6.14}$$

where ω_0 is the central angular frequency of the pulse, L is the length of the material that the pulse travels, I(t) is the instantaneous intensity profile of the pulse (herein is assumed to be Gaussian) and λ is the wavelength of light in vacuum. Such a phase shift will induce an angular frequency shift within the pulse given as:

$$\Delta\omega(t) \propto -\frac{8\pi n_{\kappa} L}{\lambda_0 \tau^2} t \exp(-\frac{2t^2}{\tau^2}) \qquad (6.15)$$

Figure 4 shows the variation in angular frequency as a function of time in response to the intensity varying refractive index.

In the presence of both GVD and SPM within an optical fibre, the temporal profile of the pulse will be affected in a different way than what is anticipated when either of these phenomena act independently. Specifically, due to SPM new frequencies will be generated, shifted to lower frequencies near the leading edge of the pulse and towards higher frequencies near the trailing edge of the pulse.

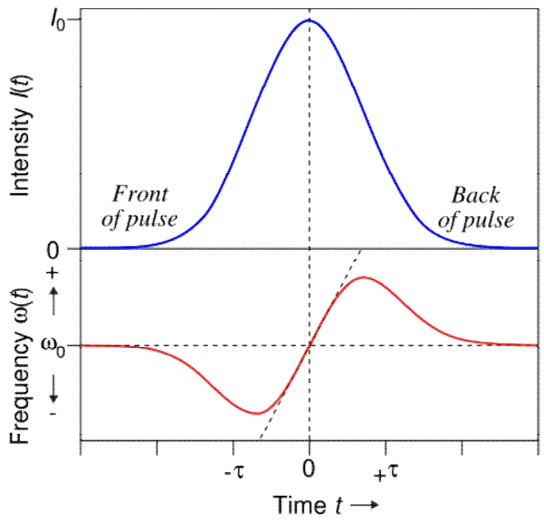

Figure 4: A Gaussian intensity ultra-short pulse (top figure) upon its propagation through non-linear media such an optical fibre may undergo self phase modulation due to the intensity dependent refractive index. This will cause an instantaneous increase in frequency, which around the central frequency is approximately linear as shown in the lower figure. The leading edge (in time) of the pulse is frequency shifted towards the lower (red) frequencies whereas the trailing edge is shifted towards the higher (blue) frequencies, resulting in the generation of more frequencies, and hence a broader spectrum [11].

Normal GVD will now act upon these frequencies, whereby the red frequency components will travel faster and the blue components will travel shower, stretching in time even further the profile of the pulse than what is expected by GVD alone. In addition, the amount of SPM phase shift will decrease since the peak intensity of the pulse progressively drops due to the GVD-induced temporal broadening [8]. The interplay of such phenomena can assist in the generation of ultra-short laser pulses of even shorter pulse durations when proper compensation schemes are employed [12].

SPM is more prominent in single mode fibres, which exhibit a small central core and therefore the presence of high intensities is more favoured.

6.2 Dispersion compensation and measurement

6.2.1 Prism/grating pairs

A number of techniques have been employed to pre-compensate the effects of dispersion within optical systems. Pairs of prisms or gratings placed at a certain distance from each other is one of the most commonly used techniques for pre-compensating particularly large amounts of GVD. In a set of four prisms, as shown in figure 5, the first set of prisms (located at distance L from one another) acts to spread the incoming pulse into its frequency components and allowing them to propagate parallel to one another prior reaching the second prism pair, where the frequency components are refracted and spatially recombine to give the negatively dispersed pulse [13].

By adjusting the distance between the prisms or gratings, the amount of negative GVD introduced will cancel the existing positive GVD caused by the lenses, coated mirrors and microscope objectives in a given optical arrangement.

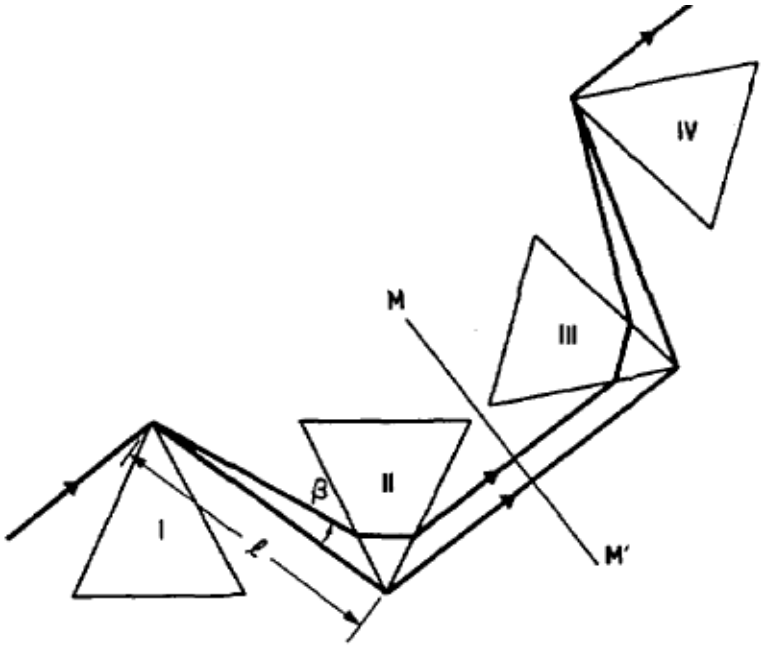

Figure 5: Optical arrangement of four prisms used to induce negative dispersion on the incident ultra-short pulses as part of a positive dispersion compensation scheme. The separation l between the first (I and II) and second (III and IV) prism pair determines the amount of positive chirp that will be introduced to the incident pulses. The prisms are also positioned in such a way that the incident beam finds their surface at Brewster angle [13].

The use of chirped mirrors is another common technique, for pre-compensating the positive GVD produced within a laser cavity. The chirped mirrors are normally used in pairs and are specifically coated to impart a certain amount of phase delay at each reflected wavelength. By adjusting the number of times the beam will bounce off the mirror pair, the amount of negative GVD introduced can be controlled, although

geometry limitations will ultimately set an upper limit to the amount of GVD that can be pre-compensated [14].

6.2.2. SLM based pulse shapers

For dynamically modifying and pre-compensating all orders of dispersion, SLM based pulse shapers are particularly popular. A number of pulse shaper geometries have been implemented for pre-compensation of phase distortions. However, the idea behind them is the same and is illustrated in figure 6. An incoming pulse is spread into its spectral components by means of a grating and is subsequently focused into a thin line on a phase mask (herein generated by an SLM) by means of a cylindrical lens.

Each of the computer-controlled SLM pixels is responsible for imprinting a certain phase delay on a thin range of wavelengths. The pulse exits the SLM which is located at the Fourier plane of the cylindrical lenses, is re-collimated and its spectrum is reconstructed upon encountering another grating [15]. Hardware limitations and the introduction of some degree of dispersion in the system are some of the disadvantages of the SLM based pulse shapers. Power loss is also another disadvantage due to the SLM itself as well as the diffraction gratings.

All the above mentioned methodologies for pre-compensating dispersion and phase distortions in optical systems depend on the fact that dispersion is known or close to known in advance. Therefore, pulse characterisation techniques need to be employed in addition to the pre-compensation methods in order to provide a full distortion

characterisation and compensation of the pulses at a certain location in the beam path.

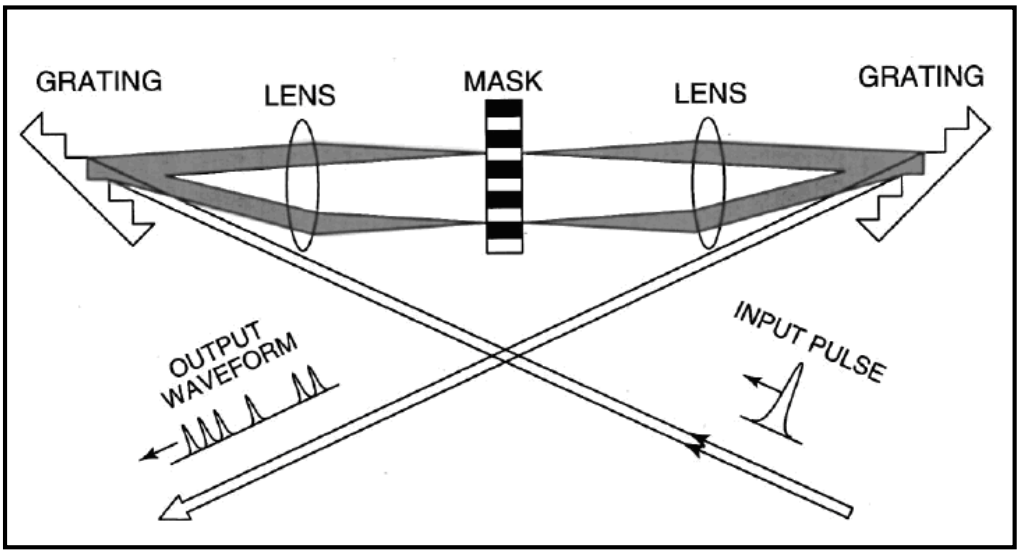

Figure 6: A typical pulse shaper. A laser pulse is incident on a diffraction grating and is subsequently spread to its spectral components. The pulse spectrum is then focused onto an SLM (or a static phase mask as shown here), where the computer controlled pixels of the SLM will phase modulate individual short wavelength bands. Upon exiting from the SLM/phase mask, the beam is re-collimated, and its wavelengths are spatially recombined upon leaving the second grating [15].

6.2.3. Frequency resolved optical gating (FROG)

A very reliable pulse measurement and characterisation technique is the Frequency Resolved Optical Gating (FROG) [16]. As opposed to traditional autocorrelation techniques which, by assuming a pulse shape, provide information about the time bandwidth of the pulse, omitting any spectral information, FROG is sensitive to chirp. It extracts the pulse's spectral characteristics by experimentally recording the pulse spectrogram, given as:

$$SP_{FROG} = \left| \int_{-\infty}^{\infty} E(t)G(t-\tau)\exp(-i\omega t)dt \right|^2 \tag{6.16}$$

The spectrogram is simply a set of spectra corresponding to the gated autocorrelation signal as the delay τ is varied. $G(t-\tau)$ is the varying time delay gate function and $E(t)$ is the electric filed amplitude of the pulse of angular frequency ω. Through this spectrogram it can be determined which frequencies arrive earliest in time [10]. There are many variations in the FROG geometries one of which is the second harmonic generation FROG (SHG-FROG). The basic SHG-FROG geometry relies on the SHG-autocorrelator geometry, however in SHG-FROG the photomultiplier is substituted with a spectrometer and a CCD camera. This method captures the second harmonic autocorrelation signal produced as a function of delay and spectrally resolves it. Mathematically, the spectrally resolved signal can be described as:

$$I_{SHG-FROG} = \left| \int_{-\infty}^{\infty} E(t)E(t-\tau)\exp(-i\omega t)dt \right|^2 \tag{6.17}$$

where the gating function is now the delayed replica of the original pulse. A retrieval algorithm is subsequently implemented in order to extract the phase and amplitude characteristics from the pulse spectrogram.

Through FROG, the temporal and spectral characteristics of a pulse can be determined however the method itself can not be used for compensation. FROG has also been used in combination with computer controlled pulse shapers whereby an optimisation algorithm

uses the SHG as a feedback. In each iteration of the feedback loop, a random phase change is applied and the changes in the SHG-FROG signal are observed. At the end of each iteration it is decided whether these changes will be adopted or not [17]. Such approaches, involve random and only approximate estimation of the phase distortions within the optical system and the adaptation of interferometric geometries in a microscope arrangement is usually complex and tedious.

6.2.4. Spectral Phase Interferometry for Direct Electric Field Reconstruction (SPIDER)

Another popular technique for obtaining information on the amplitude and spectral phase of an ultra-short pulse is known as Spectral Phase Interferometry for Direct Electric Field Reconstruction, abbreviated as SPIDER. In SPIDER, the original pulse is split into three copies, a pair of two pulses delayed by τ with respect to each other and a third pulse replica that is heavily chirped. All three pulses recombine in a frequency mixing non-linear crystal and two optically sheared pulses are generated and subsequently enter the spectrometer where their interferogram or Spidergram is captured. The interferogram of the two spectrally sheared pulses can be described as:

$$I_{SPIDER} = I(\omega + \Omega) + I(\omega) + 2\sqrt{I(\omega+\Omega)I(\omega)}\cos\{\phi(\omega+\Omega)-\phi(\omega)+\omega\tau\} \qquad (6.18)$$

where Ω is the difference in the central frequency between the two spectrally sheared pulses [10]. By obtaining experimentally the spectrum (spectral amplitude) of the pulse

and combining it with the spectral phase information extracted from the SPIDER interferogram, the temporal profile of the input pulse can be constructed [18]. Despite the fact that SPIDER is free of demanding computational algorithms for extracting the spectral information of the pulse, it is prone to noise and experimental errors and requires knowledge of the pulse to be measured in order to correctly design the SPIDER setup (i.e. in order to set the chirp parameter and delay) [10].

6.2.5. Multiphoton Intrapulse Interference Phase Scan (MIIPS) pulse shaper

A recently developed method that can provide dispersion measurements through pulse characterisation in combination with dynamic pre-compensation of dispersion is MIIPS. This technique is based on the concept of Multiphoton Intrapulse Interference (MII) [19]. This is a phenomenon that occurs during non-linear processes in response to the broad bandwidth of an ultra-short pulse. Due to the broad range of frequencies, multiple pairs of frequencies within the pulse bandwidth combine (interfere) constructively or destructively to contribute towards a non-linear process of a certain frequency i.e. frequency doubling in a non-linear crystal or two-photon excitation in an atomic system at twice the central pulse frequency $2\omega_0$ [19]. The phase relationship between the intrapulse frequency pairs will determine whether the interference will be constructive or destructive. Therefore by appropriately tuning the phase relationship between the pulse frequencies, the probability of a non-linear process and hence its efficiency can be controlled. For example, by controlling the spectral phase of the pulse, the temporal duration of the pulse can be significantly decreased to minimise unwanted photo-

bleaching during non-linear imaging due to the lower peak intensity of the resulting pulse. In addition, appropriate phase tuning can result in the activation of a broad range of fluorophores without the need for laser tuning or multiple laser sources [3, 20].

The process of MIIPS relies on the effect that phase modulation has on non-linear phenomena at certain frequencies such as frequency doubling in a non-linear crystal. During MIIPS, the SHG signal is obtained and the changes in the SHG spectrum are monitored, in response to a number of reference phase functions imprinted on the original pulse by the shaper. These functions are then used to identify the spectral phase of these pulses. The SHG signal $S^{(2)}(\Delta)$ at a frequency $2(\omega_0 + \Delta)$, where Δ is the detuning from the central pulse frequency ω_0 can be expressed as:

$$S^{(2)}(\Delta) = \left| \int \left| E(\Delta + \Omega) \right| \left| E(\Delta - \Omega) \right| \exp\left\{ i\left[\varphi(\Delta + \Omega) + \varphi(\Delta - \Omega) \right] \right\} d\Omega \right|^2 \qquad (6.19)$$

where $\left|E(\Delta \pm \Omega)\right|$ is the electric field amplitude as a function of frequency, Ω corresponds to the angular frequency component and $\varphi(\Delta \pm \Omega)$ is the spectral phase [21]. In the case of TL pulses in the absence of dispersion, the generated SHG signal is maximised and the exponential (oscillatory) component of the equation (6.19) is cancelled, i.e.

$$\varphi(\Omega + \Delta) = -\varphi(\Omega - \Delta) \qquad (6.20)$$

By implementing Taylor series, the spectral phase $\varphi(\omega)$ as a result of all non-linear phenomena can be expressed as:

$$\varphi(\omega) = \varphi(\Omega + \Delta) + \varphi(\Omega - \Delta) = \varphi^{(0)} + \varphi^{(1)}(\omega - \omega_0) + \frac{1}{2!}\varphi^{(2)}(\omega - \omega_0)^2 + \frac{1}{3!}\varphi^{(3)}(\omega - \omega_0)^3 \ldots \tag{6.21}$$

where $\varphi^{(0)}$ is the zero order spectral phase corresponding to the relative position of the pulse envelope (assume a Gaussian for our applications) and the carrier wave [22]. The first order spectral phase $\varphi^{(1)}$ corresponds to a linearly varying phase with ω that in the time domain causes a translation, τ, of the pulse in time, i.e. $E(t) \rightarrow E(t + \tau)$ [19]. In the first approximation, by neglecting odd order terms in equation (6.21) it becomes obvious that for the equation (6.20) to be satisfied, the second derivative of the phase needs to be locally (at a certain frequency ω) zero. MIIPS measures this unknown spectral phase $\varphi(\omega)$ of the pulse, by superimposing a set of reference functions parameterised as $-f(\omega, \delta(\omega))$, and the resulting SHG spectrum is recorded. These functions are scanned across the fundamental laser spectrum and the SHG signal is maximised locally at ω when:

$$\varphi''(\omega) = f''(\omega, \delta(\omega)) \tag{6.22}$$

i.e. when the reference function intersects the unknown spectral phase and the parameter $\delta_{max}(\omega)$ is noted. Note that:

$$\varphi''(\omega) \equiv \varphi^{(2)}(\omega) \cong \frac{d^2\varphi(\omega)}{d\omega^2} \tag{6.23}$$

The unknown spectral phase information can be obtained by combining $\delta_{max}(\omega)$ and equation (6.22). The most common reference functions utilized are the quadratic function or the sinusoidal function of the form:

$$f(\omega,\delta) = a\sin\left[\gamma(\omega-\omega_0)-\delta\right] \tag{6.24}$$

where a (in rad) and γ (in fs) are fixed constants and δ is the phase shift scanned from 0 to 4π [23].

The basic operation principle of MIIPS is illustrated in figure 7. As seen in the right hand side set of figures, during MIIPS a set of parameterised (with parameter δ) reference functions are scanned across the laser spectrum or in other words the reference spectral phase is superimposed to the unknown spectral phase of the input pulse. When the reference intersects the unknown phase, any distortions are locally cancelled, the SHG signal is maximised (a peak appears) and the parameter $\delta(\omega)$ is noted. The middle set of figures represents the two dimensional representation of the SHG signal as a function of frequency ω and reference phase shift δ.

These MIIPS traces appear as diagonal thin lines separated by π rad and appear parallel in the absence of phase distortions as in the case of TL pulses. In the case of quadratic or cubic spectral phase functions, the induced chirp will change the orientation of these curves. An iterative measurement-compensation routine is also employed to increase the accuracy of the process. Upon calculation of the unknown quadratic spectral modulations, their double integration will yield the unknown spectral phase. The algorithm will then add the opposite phase function in order to perform compensation [24, 25].

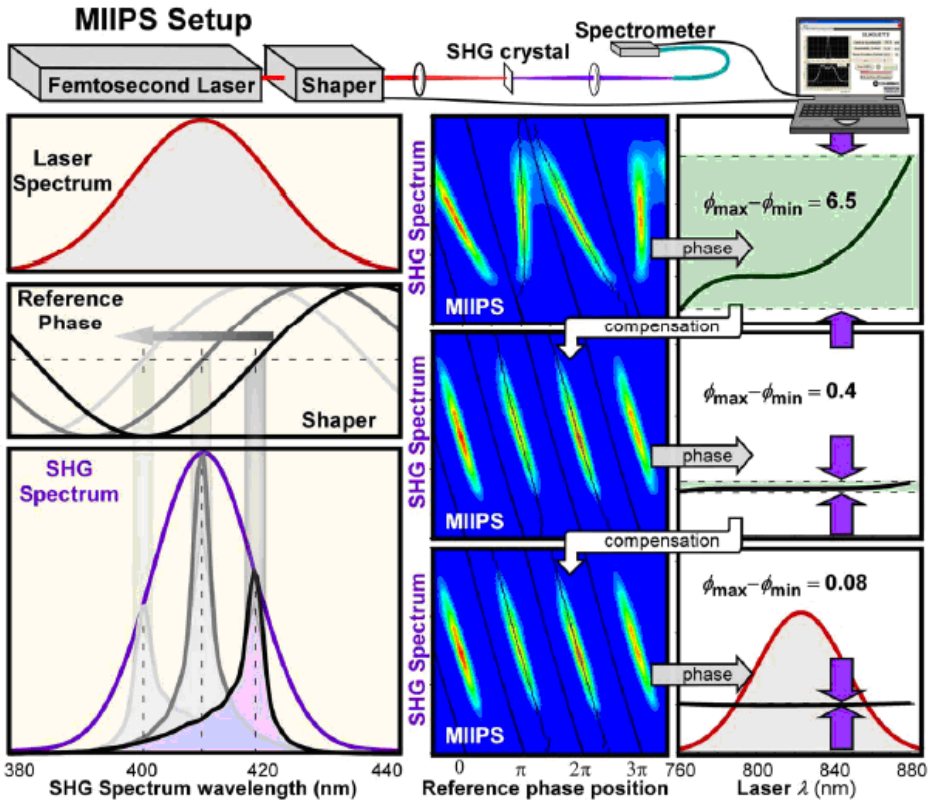

Figure 7: The MIIPS pulse shaper is based on a liquid crystal spatial light modulator which provides phase modulation in the spatial spectrum of the ultra-short pulses generated by a laser oscillator. The MIIPS is based on the phenomenon of multiphoton intrapulse interference between the frequencies of a broadband with well defined phase relationship. During MIIPS a known reference phase function is used to measure the unknown spectral phase imposed on the pulses due to dispersive effects introduced by an optical system. At each frequency that the reference function intersects the unknown function, the algorithm cancels locally any distortions and this is observed as a maximum in the SHG signal (far left plots). This can also be represented (middle plots) as diagonal traces which correspond to a plot of frequency as a function of the position of the reference phase (in rad). In the absence of any distortions, the MIIPS traces lie diagonally and parallel to each other however any distortions will force the traces to deviate from this orientation. By monitoring the changes in the SHG signal of the unshaped pulsed whilst the reference spectral phase is scanned across the laser spectrum, the unknown spectral phase corresponding to the pulse distortions is measured. The inverse phase function is imprinted on the pulses during pre-compensation. An iterative dispersion measurement routine can also be employed to improve the accuracy of the measured dispersion (far right plots) [24] .

The pulse shaper geometry based on MIIPS (Biophotonics Solutions) obeys the same principles as the SLM based pulse shaper shown in figure 6. However, in the case of the MIIPS pulse shaper used herein, the spectral broadening of the pulses is provided by a single grating and the cylindrical lenses are substituted by a cylindrical mirror that provided reflection and focusing of the pulses into a thin line onto the phase only, 640-pixel liquid crystal SLM.

6.3 Dispersion pre-compensation in a Gaussian photoporation setup using MIIPS

The laser source used for this set of experiments was a mode-locked Ti: Sapphire (Femtolasers, Femtochrome) oscillator generating 12fs laser pulses, at 800 nm and 80 MHz repetition rate. Two pairs of chirped mirrors were appropriately positioned in the cavity to provide pre-compensation for positive GVD induced by the laser optics and primarily the Ti: Sapphire crystal itself. The laser output power was approximately 550 mW during ML operation. The fundamental laser spectrum with bandwidth (FWHM) was calculated approximately to be 90 nm (assuming Gaussian shaped pulses) and is shown in figure 8.

The laser beam exiting the laser, was directed through a x1.6 magnifying telescope consisting of two planoconvex lenses of focal lengths F_1 =100 mm and F_2 = 160 mm and was subsequently directed into the pulse shaper where the pulses where spectrally modulated. Upon leaving the shaper, the laser pulses were directed through a Gaussian photoporation setup consisting of two silver coated mirrors as part of a periscope which

translated the beam horizontally upwards. The beam passed through a lens of focal length 160 mm which was positioned at 360 mm distance from the focusing microscope objective (Newport, x60, NA=0.85).

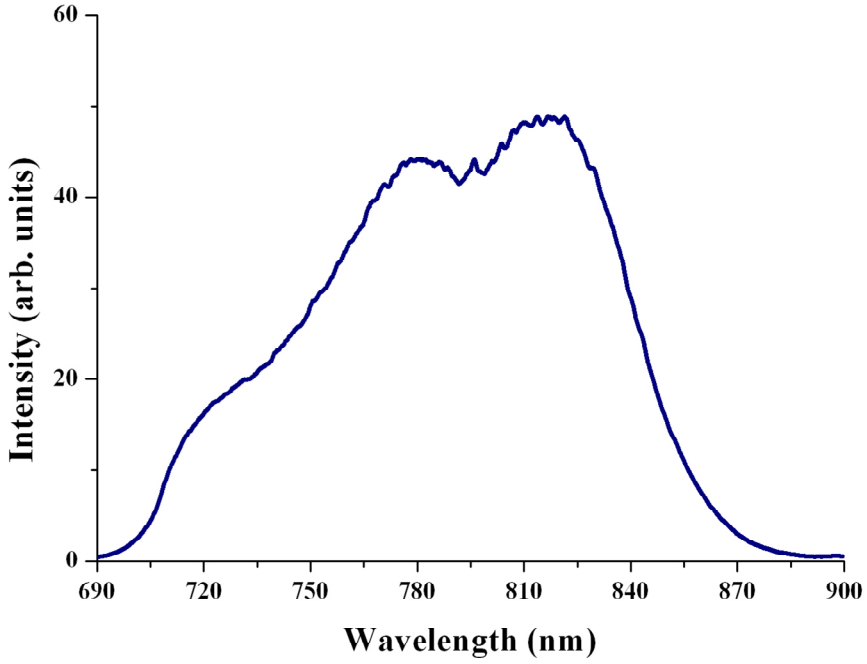

Figure 8: The fundamental spectrum of the laser obtained using a fibre spectrometer. The FWHM bandwidth of the laser spectrum was automatically calculated by the MIIPS software to be 90nm (the program assumes Gaussian shaped spectrum)

The overall setup is very similar to the Gaussian photoporation setup described in chapter 3. Figure 9 shows the image of the Gaussian photoporation setup used for dispersion measurements and compensation. For the purposes of dispersion compensation, a SHG detection unit was assembled using an aspheric lens of focal length F_3 = 4.25 mm that focused the divergent beam emerging from the microscope objective into a fibre spectrometer (Ocean Optics). A thin (100 μm), type I, BBO crystal was used to produce a SHG signal at the focus of the objective.

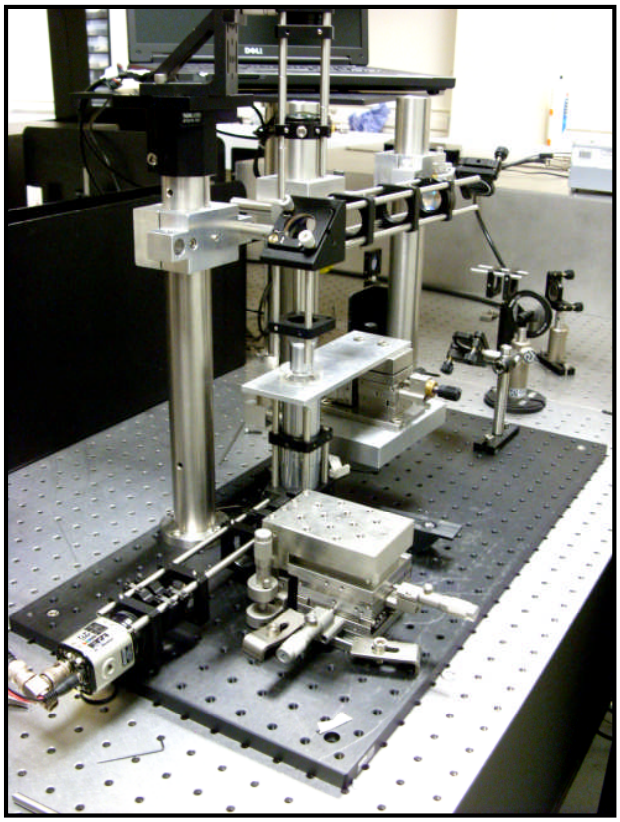

Figure 9: Image of the Gaussian photoporation setup which was used for dispersion measurement and PRE-compensation using the MIIPS pulse shaper.

With the use of a short pass filter, the fundamental (red) spectrum of the laser was blocked, allowing only the SHG signal to be collected by the spectrometer. The red spectrum was also collected, for purposes of calculating the TL pulses at the sample, by substituting the filter with a diffuser (scattering tissue) to prevent saturating the spectrometer. The spectrometer and the SLM of the pulse shaper communicated through two different USB ports with the computer which run the MIIPS algorithm.

The overall system dispersion, which includes that imposed by the photoporation system, the shaper and any residual from the laser was calculated by the MIIPS algorithm and is

shown in figure 10. The calculated spectral phase was approximately quadratic with some additional higher distortions present in the curve. The shape of the curve implies that linear chirp is the dominant dispersion phenomenon that governs the temporal broadening of the pulses, with the addition of small amounts of third or higher order dispersive effects. Upon this measurement and during pre-compensation, the shaper will add the inverse to the measured spectral phase to the modulated pulses.

Figure 11 shows the SHG signal before and after the measurement and pre-compensation process.

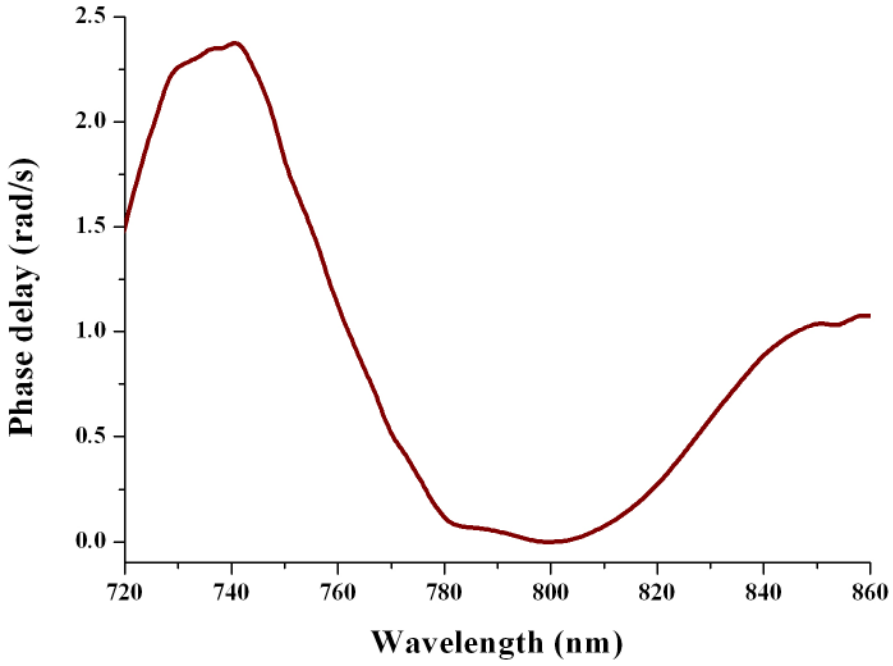

Figure 10: The calculated spectral phase (phase delay as a function of wavelength) imposed by the Gaussian photoporation optics, the shaper and the laser itself. From the shape of the curve, it can be deduced that the spectral phase is described approximately by a quadratic function and therefore the most prominent contribution comes from the GVD. Due to additional distortions apparent in the curve, higher order dispersion must be present.

It is evident that the SHG signal obtained by focusing uncompensated, chirped laser pulses on the BBO crystal is weak and appears distorted. This is the result of the random phase relationship between the intrapulse frequencies that contribute towards this non-linear process which is the heart of MIIPS.

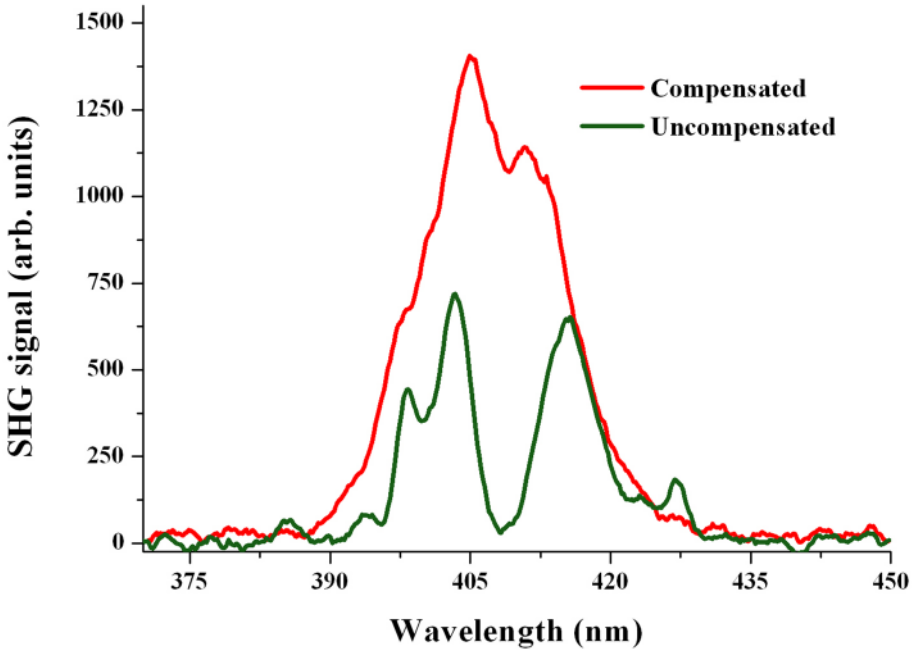

Figure 11: The SHG signal obtained at the microscope objective focus before and after compensation. The uncompensated signal appears weak and distorted as dispersion acts towards phase mismatching due to time varying phase relationship between the intrapulse frequencies. However, in the case of shaped (close to TL) pulses the intrapulse interference of frequencies allows for phase matching and hence more intense SHG signal.

Upon pre-compensation of second and higher orders of dispersion, the spectral phase of the pulses is shaped and in the absence of such phase distortions, optimum phase matching is achieved and maximum signal is obtained. Figure 12 shows the compensated ultra-short pulse at the objective focus. The calculated FWHM of the compensated pulse

at the plane of the sample was 12.1 ± 1 fs.

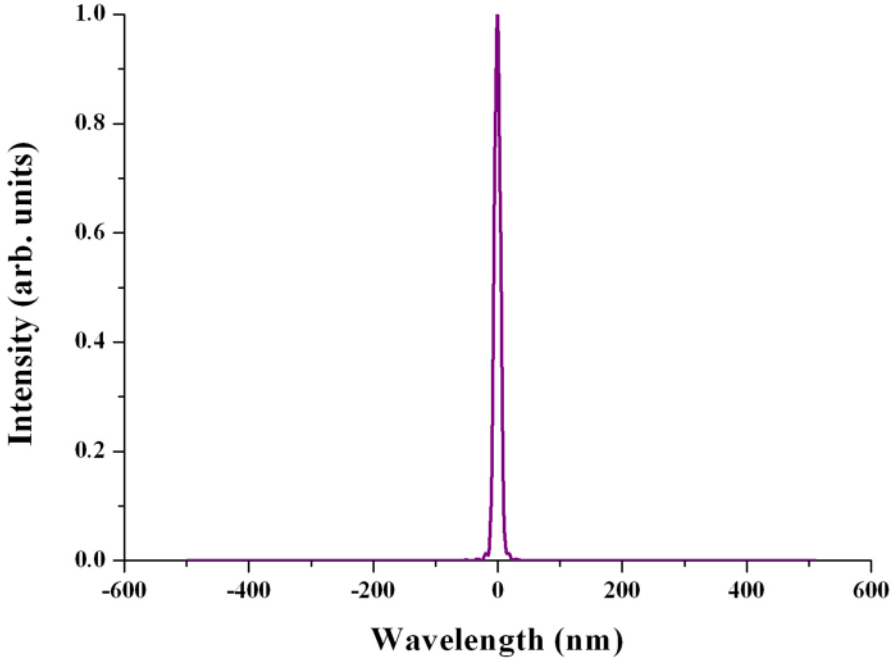

Figure 12: Temporal profile of the pulse at the sample upon dispersion measurement and compensation using the MIIPS pulse shaper. The calculated FWHM temporal width was 12.1 fs. The calculation of the pulse duration was performed by the algorithm using an inverse Fourier transformation given the laser fundamental spectrum and the measured spectral phase at the sample.

The calculation of the pulse duration is performed by IFT for the given fundamental laser spectrum and spectral phase at the objective focus. Some residue of dispersion still remains due to the weak signal obtained near the edges of the SHG signal. However, the ratio of the FWHM pulse duration, τ, of the (calculated) compensated pulses over the pulse duration of the corresponding theoretical TL pulses τ was satisfyingly low, equal to $\tau / \tau_{TL} = 1.002$.

6.4 Dispersion compensation in an axicon tipped fibre using MIIPS

Figure 13 shows the optical setup used for dispersion measurement and compensation in an axicon tipped optical fibre. The main body of the optical setup which included the laser oscillator, the magnifying telescope, the pulse shaper and the mirror M_6 was common for the dispersion measurement and compensation in the Gaussian photoporation setup and the axicon tipped fibre. The mirror M_7 was supported on a flip mirror mount that selected between the Gaussian photoporation setup located at the back of the optical table and the axicon tipped fibre setup. The output coupler consisted of a microscope objective (New focus, x16, NA=0.25) and a fibre mount that supported the fibre. The fibre coupler was mounted on an XYZ stage in order to provide accurate light coupling into the fibre core. The axicon tipped fibre used for the compensation was fabricated using the method described in chapter 5 and had the same parameters (in terms of cone angle and length) with the fibre used for cell photoporation. The divergent fibre output was refocused on a BBO crystal using an aspheric lens of focal length $F_3 = 4.25$ mm. The SHG signal was collected through an achromatic doublet lens of focal length $F_4 = 50$ mm, passed through a low pass filter and was subsequently focused onto the fibre spectrometer. The fundamental spectrum of the incident beam was also collected by removing the filter and inserting a diffuser in front of the spectrometer.

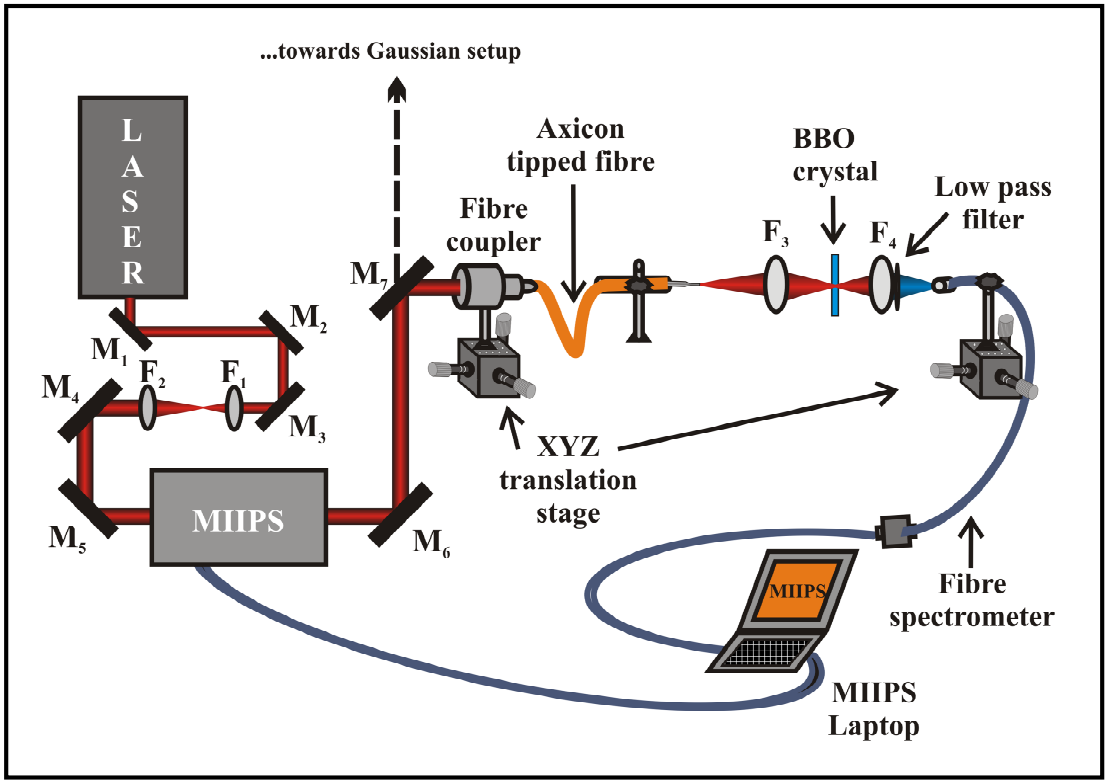

Figure 13: Diagram of the optical setup used for dispersion measurement and compensation in an axicon tipped optical fibre. A pulsed laser beam emitted by a Ti: Sapphire laser was passed through a magnifying x1.6 telescope (F_1 =100 mm, F_2 =160 mm) and was subsequently directed into the MIIPS pulse shaper. Upon exit, the spectrally shaped beam was directed via a set of two mirrors M_6 and M_7 (silver coated) into a fibre coupler consisting of a x20 microscope objective of NA=0.4 and a fibre mount into which the fibre was supported. Upon successful coupling, the divergent fibre output was collected by an aspheric lens of focal length F_3 =4.25 mm and the light was refocused on the BBO crystal. An achromatic doublet lens of focal length 50 mm focused the beam on the fibre spectrometer which was supported on an XYZ translation stage. Both the spectrometer and the pulse shaper were connected to the MIIPS computer via two independent USB ports. The mirrors M_1 - M_5 were silver coated.

Figure 14 shows the image of the axicon tipped fibre setup used for dispersion

measurement and compensation.

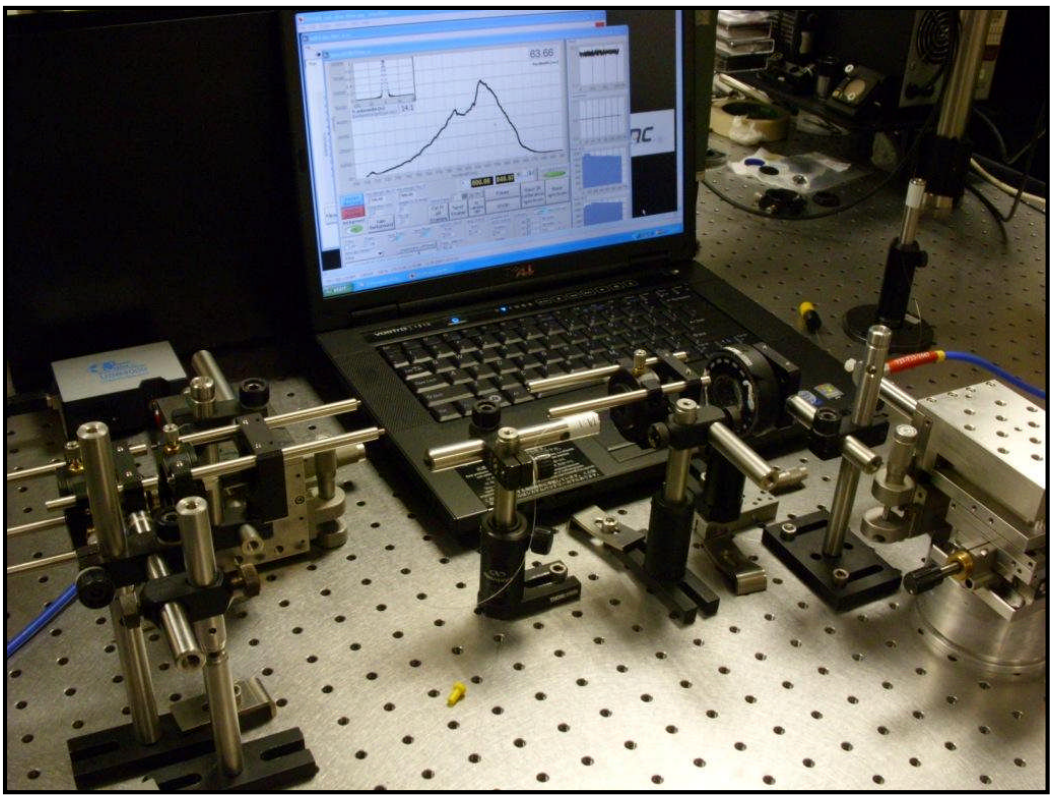

Figure 14: Image of the axicon tipped fibre setup used for dispersion measurement and compensation. The fibre coupler (on the left) launches the light into the axicon tipped fibre which is mounted horizontally on a post. The fibre output is collected and focused on a BBO crystal by means of an aspheric lens. The SHG and the fundamental spectrum of the laser are collected and focused on the fibre spectrometer (far right). The fibre spectrometer is supported on an XYZ stage for accuracy in its positioning with respect to the focus. The spectrometer, as well as the SLM of the pulse shaper, were connected to the laptop shown in the background which supports the algorithm that runs the MIIPS.

The laser pulses incident on the fibre coupler were pre-compensated and their pulse duration at the point of entry into the fibre coupler was 12.1 fs with an accuracy τ/τ_{TL} =1.027 with respect to the theoretical TL pulse duration. Figure 15 shows the

measured dispersion function imposed on the pulses upon their passage through the fibre coupler and the axicon tipped fibre. The phase delay of the intrapulse frequencies appears to be approximately a cubic function of the wavelength, as evident from the comparison of the blue and dashed orange curves which corresponds to a cubic function. A cubic spectral phase corresponds to a quadratic chirp which appears to be the dominant dispersion phenomenon imposed on the pulses traversing through the fibre.

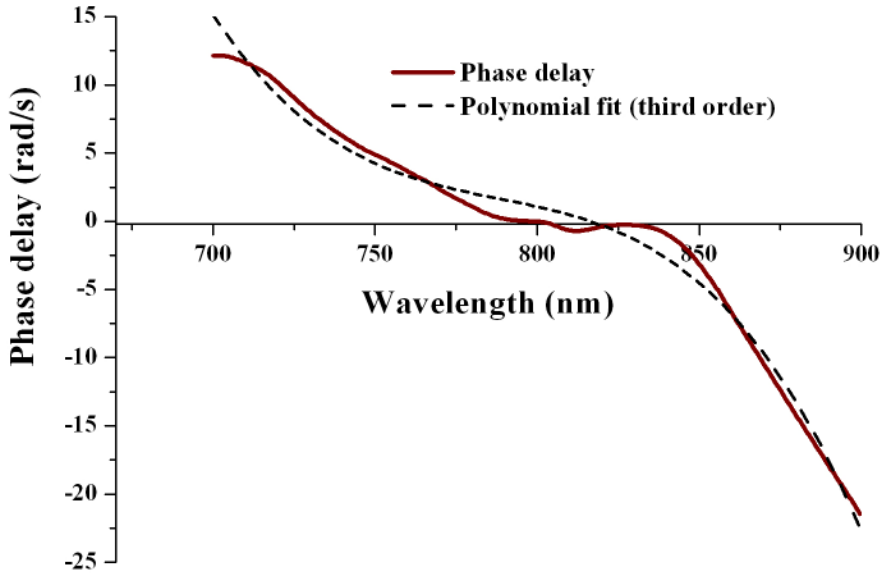

Figure 15: The measured spectral phase imposed on the pulses upon their propagation through the fibre coupler and the axicon tipped fibre. The relation between the phase delay and the wavelength is approximately cubic which appears to be almost dominant. Additional dispersion potentially of both linear and no-linear nature appears to be present judging from the distortions present in the curve. A cubic fit function is also plotted for comparison.

The SHG signal generated by the unshaped focused laser pulses on the BBO crystal is shown in figure 16.

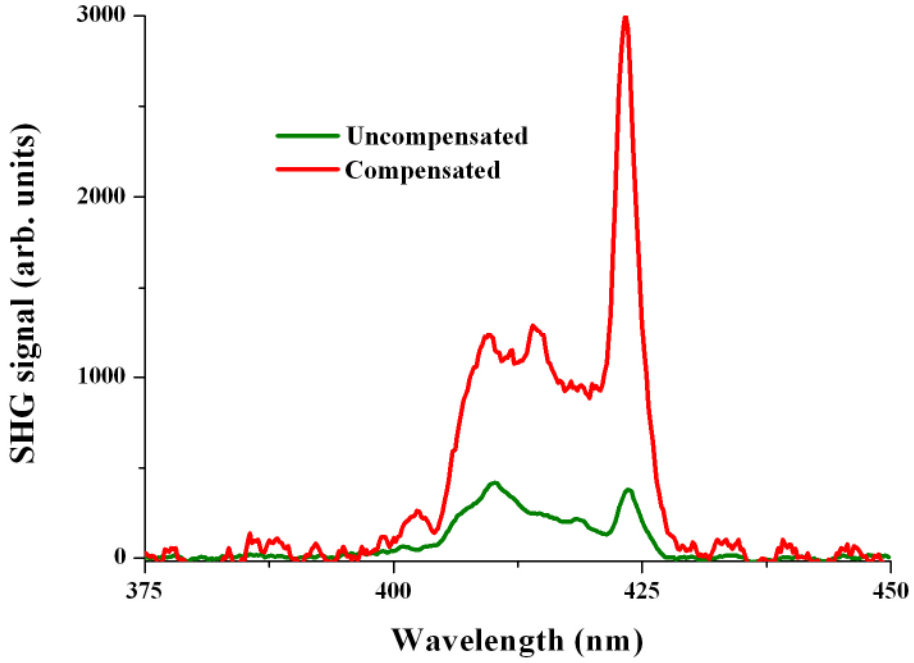

Figure 16: The blue curve corresponds to the amplitude of the SHG signal collected as a result of the focusing of the chirped laser pulses on the BBO crystal. The uncompensated signal appears to be weak as opposed to the compensated SHG signal collected upon dispersion measurement and compensation. The amplitude of the SHG signal is now increased however the overall shape of the signal is as smooth as expected probably due to residual uncompensated higher order dispersion especially at 350 nm where a strong peak is observed.

As evident from figure 16, the SHG signal induced by the chirped fibre output was very weak due to the random, time varying phase relationship of the frequencies within the pulse that contributed towards phase mismatching and therefore poor SHG signal. In addition, the input pulses coupled into the fibre were TL, therefore the non-linear phenomena affecting the pulses within the fibre were far more severe compared to those imposed on chirped pulses. The calculated pulse duration of the compensated laser pulses was 16 fs with deviation from the theoretical TL pulse duration given as τ/τ_{TL} =1.163. Figure 17 shows the calculated pulse duration of the compensated ultra-short pulses upon

travelling through the optics of the axicon tipped fibre setup.

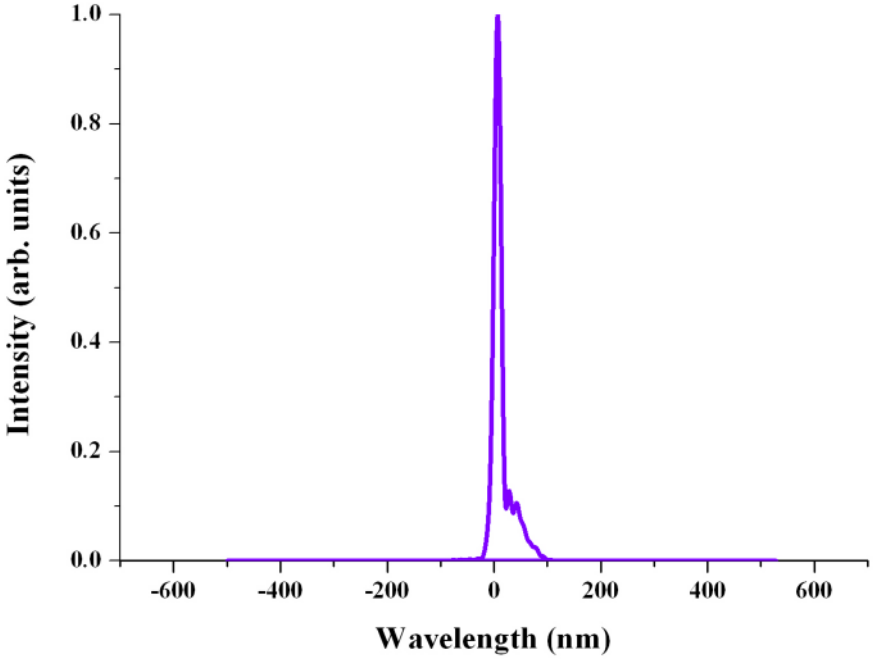

Figure 17: The graph represents the temporal profile of the pre-compensated pulses upon traversing the optics of the axicon tipped fibre setup. The calculated FWHM pulse duration of the laser pulses was 15 fs with deviation from the theoretical TL value being τ / τ_{TL} =1.163. As evident from the shape of the pulse's temporal profile, residual third order dispersion is present causing a small degree of distortion in the temporal profile of the pulses. Other orders of dispersion such third or higher may also be contributing.

The presence of residual uncompensated dispersion could be attributed to the low SHG signal obtained upon focusing the fibre output on the BBO crystal which was due to poor fibre coupling. In addition, the fundamental spectrum of the pulses appeared to be distorted upon their passage through the optical fibre due to SPM with an accompanying slight reduction in bandwidth in contrast to what is expected at the fibre output. This could also be attributed to the absorption of part of the UV spectrum emitted upon SHG

by the focusing optics behind the fibre. In order to amend this, quartz or UV fused silica lenses should be used to focus the light into the fibre spectrometer. These are the very first results obtained for dispersion pre-compensation in an optical fibre. Further investigation is required to improve this type of measurement with particular attention to the fibre coupling.

6.5 Conclusion

In this chapter I have shown the first steps towards successful dispersion measurement and pre-compensation in optical systems used for optical transfection of cells, such as the Gaussian photoporation setup and the axicon tipped fibre. In order to achieve this, I implemented a state of the art pulse shaper based on MIIPS, whereby an unknown spectral phase is used to measure the unknown distortions imprinted on the pulses due to dispersive phenomena. The MIIPS pulse shaper allowed for the measurement of all orders of dispersion and automatic pre-compensation of ultra-short pulses. This was achieved by dynamically phase modulating the spatial spectrum of the pulses by means of a spatial light modulator.

In the case of the Gaussian photoporation setup, any distortions affecting the temporal profile of the ultra-short pulses were primarily due to GVD, as evident by the approximate quadratic profile of the measured spectral phase. The opposite phase function was imprinted on the pulses via the SLM pixels, cancelling the undesired temporal spreading of the intrapulse frequencies as well as higher order dispersive phenomena. Via IFT of the compensated spectrum, the pulse duration of the shaped

pulses was found to be 12.1 ± 1 fs. The efficiency of the measurement was evident by the ratio of the compensated pulse duration over the TL pulse duration which was calculated to be 1.002. This result paves the way for exciting new studies on cellular photoporation using sub-20 fs laser pulses, which is a new and relatively unexplored area [1]. The high peak power of these pulses achieved at very low average powers (few mW), could allow for unprecedented precise membrane perforation, in the absence of collateral damage and without compromising the cell viability. Due to undesirable cell necrosis during irradiation, the ultimate efficiency of the technique may be even further improved.

In the case of the axicon tipped fibre, the imposed distortions on the laser pulses were primarily caused by quadratic chirp as evident from the measured spectral phase which was represented by approximately a cubic function. Pre-compensation was performed and the measured pulse duration of the shaped laser pulses was 16 ± 3 fs with efficiency in the measurement given as τ / τ_{TL} =1.163. According to the shape of the temporal profile of the shaped pulses, there is still a small amount of residual third order dispersion which was not compensated. This may be attributed to factors such as poor fibre coupling that contributed to a low SHG signal during dispersion measurement, as well as short SHG bandwidth that prevented compensation across the whole pulse spectrum. The former may be resolved by working on the fibre coupling whereas the latter may be tackled by changing the focusing lenses behind the fibre to those made of quartz or UV fused silica. This will allow maximum transmission of the generated SHG signal and maximum SHG bandwidth hence optimum compensation across the whole pulse spectrum. As these are preliminary results, such issues have not yet been addressed; however this will be the case as part of future work.

Future work also involves dispersion measurement and pre-compensation of chirped ultra-short pulses, followed by the addition of well defined phase functions that would allow us to tailor the spectral phase of the pulses so that any desired temporal bandwidth could be obtained. This could be of great advantage, as this could help us perform studies on cell photoporation as a function of the pulse duration and allow us to identify the optimum pulse duration that result in highest photoporation efficiency. The focus of current work is photoporation of cells whereby pulses as short as sub-20 fs are delivered on the cellular membrane in the presence of fluorescent dyes and nucleic acids encoding for fluorescent proteins. In the context of photoporation, the interaction of extremely short pulses with cells shows great potential as the low average powers of only a few mW at the focus may prevent any kind of local damage to the membrane, allowing for minimally invasive photodisruption of the cellular membrane. The low irradiance threshold required for membrane perforation, would thus allow the uptake of extracellular material by the cells without compromising the cell viability and with minimal input power requirements.

References

[1] A. Uchugonova, et al., "*Targeted transfection of stem cells with sub-20 femtosecond laser pulses,"* Optics Express **16**(13), p. 9357, 2008.

[2] L.T. Schelhas, et al., "*Advantages of ultrashort phase-shaped pulses for selective two-photon activation and biomedical imaging,"* Nanomedicine: Nanotechnology, Biology and Medicine **2**(3), p. 177, 2006.

[3] P. Xi, et al., "*Two-photon imaging using adaptive phase compensated ultrashort laser pulses,"* Journal of Biomedical Optics **14**(1), p. 014002, 2009.

[4] I. Pastirk, et al., "*Selective two-photon microscopy with shaped femtosecond pulses,"* Optics Express **11**(14), p. 1695, 2003.

[5] C.J. Bardeen, et al., "*Feedback quantum control of molecular electronic population transfer,"* Chemical Physics Letters **280**(1-2), p. 151, 1997.

[6] Y. Silberberg, "*Laser science: Physics at the attosecond frontier,"* Nature **414**(6863), p. 494, 2001.

[7] B. Saleh and M. Teich, "*Fundamentals of Photonics"*, 2nd ed. (2001), John Wiley & Sons,

[8] G. Agrawal, "*Nonlinear fibre optics"*, 3rd ed. (2001), Academic Press, Rochester, NY

[9] M. Dantus and Y. Andegeko, " *Biomedical Imaging Using Ultrashort Laser Pulses"*, in *PTB magazine*, NASA Tech briefs, NY.

[10] I. Cormack, "PhD thesis: Rapid techniques for ultrashort optical pulse characterisation", Supervisor: W. Sibbett, (2001), School of Physics & Astronomy, University of St Andrews

[11] Wikipedia and Contributors "*Self-phase modulation"* (2009), Web page: http://en.wikipedia.org/w/index.php?title=Selfphase_modulation&oldid=282968336.

[12] D.E. Spence, et al., "*60-fsec pulse generation from a self-mode-locked Ti:Sapphire laser,"* Optics Letters **16**(1), p. 42, 1991.

[13] R.L. Fork, et al., "*Negative dispersion using pairs of prisms,"* Optics Letters **9**(5), p. 150, 1984.

[14] R. Paschotta, et al., "*Double-chirped semiconductor mirror for dispersion*

compensation in femtosecond lasers," Applied Physics Letters **75**(15), p. 2166, 1999.

[15] A.M. Weiner, "*Femtosecond pulse shaping using spatial light modulators,"* Review of Scientific Instruments **71**(5), p. 1929, 2000.

[16] R. Trebino, "*Frequency-resolved optical gating: the measurement of ultrashort laser pulses",* 1st ed. (2000), Kluwer Academic Publications, Massachusetts, U.S.A.

[17] D. Yelin, et al., "*Adaptive femtosecond pulse compression,"* Optics Letters **22**(23), p. 1793, 1997.

[18] M.E. Anderson, et al., "*Gold-SPIDER: spectral phase interferometry for direct electric field reconstruction utilizing sum-frequency generation from a gold surface,"* Journal of Optical Society of America B **25**(6), p. A13, 2008.

[19] B. Broers, et al., "*Diffraction and focusing of spectral energy in multiphoton processes,"* Physical Review A **46**(5), p. 2749, 1992.

[20] P. Xi, et al., "*Greater signal, increased depth, and less photobleaching in two-photon microscopy with 10 fs pulses,"* Optics Communications **281**(7), p. 1841, 2008.

[21] V.V. Lozovoy, et al., "*Multiphoton intrapulse interference.IV.Ultrashort laserpulse spectral phase characterization and compensation,"* Optics Letters **29**(7), p. 775, 2004.

[22] Y. Coello, et al., "*Interference without an interferometer: a different approach to measuring, compressing, and shaping ultra-short laser pulses,"* Journal of Optical Society of America B. **25**(6), p. 140, 2008.

[23] B. Xu, et al., "*Quantitative investigation of the multiphoton intrapulse interference phase scan method for simultaneous phase measurement and compensation of femtosecond laser pulses,"* Journal of Optical Society of America

B **23**(4), p. 750, 2006.

[24] M. Dantus, et al., "*MIIPS characterizes and corrects femtosecond pulses,"* Laser Focus World **43**(5), p. 101, 2007.

[25] I. Pastirk, et al., "*Remote characterization and dispersioncompensation of amplified shaped femtosecondpulses using MIIPS,"* Optics Express **14**(19), p. 8885, 2006.

Chapter 7
Conclusion

This thesis began with a short introduction to the area of Biophotonics and the importance of combining knowledge from diverse disciplines in order to provide answers to complex biomedical problems. A brief discussion on the cell genome and the processes that administer protein expression was provided. Emphasis was placed on laser nanosurgery of cells and specifically on laser-assisted cell transfection, which has started establishing itself as a very powerful methodology within the areas of molecular biology, genetics and neuroscience.

In chapter two, I gave an overview of the main molecular biology concepts that concerned this thesis, more specifically the cell structure and the genome, with particular reference to how cells decode the genome and the mechanisms of protein expression. The chapter continued with a summary of the most established transfection techniques to date with particular reference to the advantages and disadvantages of each technique. Following this, I reported on optical transfection of cells using fs laser pulses as well as the physical mechanisms that underline the interaction between biological matter and fs laser pulses. At MHz repetition rates and irradiance levels well below the optical breakdown, the interaction of fs pulses with the cell gives rise to multiphoton ionization at the site of irradiation which progressively results in free electron plasma formation. No cumulative thermal effects appear to occur as the irradiance level is low and the time duration of the pulses is shorter than the time scale of any thermal effects. Photochemical

effects appear to be the dominant mechanism of membrane perforation, resulting in high resolution pore formation, with no evident collateral damage. These introductory chapters put the work presented herein into perspective, highlighting the importance of performing cellular transfection and the reasons why we are seaking an optical route for studying complex biological problems such as transfection.

The main body of my work was described in chapters three to five. In chapter three, fs photoporation and optical transfection of CHO cells was performed using a tightly focused Gaussian beam. The use of fs laser pulses for cell transfection results in a non-invasive, highly selective and ultra-precise method for perforating the cellular membrane. However, this approach comes along with demanding alignment, as careful adjustment of the laser focus on the cell membrane is normally required for each targeted cell. In order to prove this, I monitored transfection efficiency as a function of the axial position of the cell membrane with respect to the laser focus. At the laser focus, one out of two targeted cells was successfully transfected with plasmid DNA and expressed the encoded DS-Red fluorescent protein. At axial displacements greater than 3 μm the transfection rate dropped significantly. This implies that mismatching between the focus plane and the cell membrane can affect dramatically the efficiency of the method, particularly when using high NA objectives. In the last part of this chapter, I presented the results of my investigation on the topography of the photoporated cells as a function of the power at the laser focus. At power levels below the threshold for safe transfection, the induced pore appeared circular and of sub-micron diameter. The high resolution pore formation supports the fact that fs transfection is a highly localised effect with no associated collateral damage that could jeopardize the viability of the cells. Above this threshold,

interplay between photochemical and cumulative thermal effects takes place, resulting in large size pore formation and progressively to collateral damage and irreversible cell necrosis at higher powers.

In chapter four, I presented an alternative route to the highly divergent Gaussian beam for performing photoporation. This route involved generating and implementing a "non-diffracting" BB beam for delivering the laser doses on the target cell. A conical lens, the axicon, was illuminated by a Gaussian beam and the resulting interference of the rays emerging from it gave rise to the BB. With the introduction of appropriate telescopes before and after the axicon, I engineered a beam with the right parameters to convey sufficient power in a small diameter central core, therefore capable of inducing multiphoton effects. The BB acted like an optical syringe which carried an elongated focus over long axial distances. In order to prove the merits of the BB for photoporation, I monitored transfection efficiency of CHO cells using a BB, at different positions of the cell membrane along the direction of the beam propagation. This allowed me to ascertain the "useful" axial range over which transfection can be successfully obtained. These results were compared to the corresponding transfection efficiency results obtained using the Gaussian beam as shown in chapter 3. Assuming 20% to be the threshold for successful transfection efficiency, the axial range over which successful transfection is obtained using the given BB was over twenty times greater compared to the Gaussian beam. This proves that the use of a "non-spreading" beam for photoporation liberates us from the rigorous requirements of precisely locating the cell membrane. Therefore photoporation can be performed easily, without the need for excessive alignment. Such an approach paves the way for automating the photoporation technique and one can

easily envisage some sort of computer controlled, point and click solution to provide complete freedom from focus and alignment adjustments. Indeed, this was achieved and described in the last part of chapter four. The step towards automating the BB photoporation process, involved using an axicon generated BB and with the aid of an SLM the far field ring of the beam was phase modulated. This arrangement provided accurate positioning of the BB in the axial and lateral direction with respect to the cell sample. The SLM was LabView driven and interfaced with the computer mouse. This enabled us, with a click of the mouse, to appoint at will the BB on each cell and deliver the laser doses. This capability opens new prospects for performing photoporation in conjunction with other optical techniques combined in one microscope-based instrument. This system would form a Biophotonics workstation, where life scientists will be able to combine a number of optical techniques and with minimal alignment requirements would be able to perform elaborate biological studies.

In chapter five, I introduced a different approach for performing photoporation to the currently employed free-space techniques. This approach entailed the fabrication and use of a specialist type of optical fibre, the axicon tipped fibre. This fibre was fabricated by means of chemical etching which resulted in a conical (axicon like) shaped core tip. By adjusting the cone angle of the axicon tip, the achievable “working” distance between the irradiated cell and the fibre tip was selected. This way, by appropriately choosing the cone angle of the fibre, the “working” distance can be also adjusted to suit the requirements of a given application. However, there is a trade off between the desirable “working” distance and the available power at that particular distance, therefore a middle ground normally needs to be found. The relative ease in fabrication and accommodation

of the fibre on any commercially available microscope shows promise in terms of the commercial potential of this approach. One could envisage the development of an off-the-self module for photoporation that could be hosted in any microscope for photoporation with sole requirements for operation the presence of a microscope and a laser source.

My ongoing work, described in chapter six, involves photoporation studies using dispersion compensated sub-20 fs laser pulses. An SLM based, state of the art pulse shaper based on MIIPS is employed to simultaneously measure and pre-compensate dispersion, imposed on sub-20 fs pulses upon their propagation through the photoporation optics. Preliminary studies on dispersion calculation and dynamic pre-compensation were presented in a Gaussian photoporation optical system and in an axicon tipped optical fibre.

Based on the work reported in this thesis, future work could be directed towards more innovative biological studies that involve a variety of key cell lines such as stem cells, neuronal cells but also lines from a number of pathologies, tumor lines, or even tissues. Alignment-free BB transfection could be employed for delivering a variety of genes into cancerous lines and other lines from various pathologies, in order to monitor protein expression or gene silencing. This could provide a valuable insight into the factors affecting and altering the genetic profile of a diseased cell and building upon this information, may provide a route towards disease treatment. As part of stem cell research, the ability to optically address stem cells and transfect them with new genes would be of great advantage. Initial studies towards stem cell optical transfection using the Gata 4/

Gata 6 gene have already started. This gene is of particular interest as it provides control over the differentiation of a stem cell [1]. The combination of this innovative gene with advanced optical routes such as the ones described herein, offers the potential for significant advances in stem cell biomedical research. In addition to this work, laser-assisted investigation of neuronal activity is of great interest. By means of SLMs and novel beam shaping, photo-stimulation studies for monitoring the neuronal behavior and signaling may lead to fascinating findings, particularly in conjunction with the transfection of a selected number of neurons within a neuronal circuit. As a final point, a very attractive concept would be to create a directory of all the optically transfected cell lines with a variety of genes along with the corresponding laser parameters for photoporation, in the form of a database that will be at the disposal of the biomedical community as a reference point for novel biological studies.

References

[1] J. Fujikura, et al., "*Differentiation of embryonic stem cells is induced by GATA factors,"* Genes & Development **16**(7), p. 784, 2002.

Publications

Journal Publications

1) D. Stevenson, B. Agate, X. Tsampoula, P. Fischer, C.T.A. Brown, W. Sibbett, A. Riches, F. Gunn-Moore, K. Dholakia, ***"Femtosecond optical transfection of cells: viability and efficiency"***, Optics Express **14** (16), 7125-7133, 2006.

2) X. Tsampoula, V. Garces-Chavez, M. Comrie, D. Stevenson, B. Agate, C.T.A. Brown, F. Gunn-Moore, K. Dholakia, ***"Femtosecond cellular transfection using a non-diffraction light beam"***, Applied Physics letters **91** (5), 053902, 2007.
Also featured in **Virtual journal of Biological Physics Research** (2007) and in **Virtual Journal of Ultrafast Science** (2007).

3) T. Cizmar, V. Kollarova, X. Tsampoula, F. Gunn-Moore, W. Sibbett, Z. Bouchal, K. Dholakia, ***"Generation of multiple Bessel beams for a Biophotonics workstation"***, Optics Express **16** (18), 14024-14035, 2008.

4) X. Tsampoula, K. Taguchi, T. Cizmar, V. Garces-Chavez, N. Ma, S. Mohanty, K. Mohanty, F. Gunn-Moore, K. Dholakia, ***"Fibre based cellular transfection"***, Optics Express **16** (21), 17007-17013, 2008.

5) C.T.A. Brown, D.J. Stevenson, X. Tsampoula, C. McDougall, A.A. Lagatsky, W. Sibbett, F. Gunn-Moore, K. Dholakia, ***"Enhanced operation of femtosecond lasers and applications in cell transfection"***, Journal of Biophotonics **1** (3), 183-199, 2008.

Conference publications

1) X. Tsampoula, P. Fischer, K. Dholakia, "***Bessel beam photoporation studies"***, Summer school "The live cells from nano to micro: Mind the gap", Corsica, France (poster presentation 2006).

2) X. Tsampoula, V. Garces-Chavez, M. Comrie, D. Stevenson, B. Agate, C.T.A. Brown, F. Gunn-Moore, K. Dholakia, ***"Cellular photoporation using a femtosecond Bessel beam"***, 2nd Annual Biophotonics: Technology and Applications meeting, Institute of Physics (IOP), London (Oral presentation 2007).

3) X. Tsampoula, V. Garces-Chavez, M. Comrie, D. Stevenson, B. Agate, C.T.A. Brown, F. Gunn-Moore, K. Dholakia, ***"Femtosecond cellular transfection using a non-diffracting light beam"***, Proceedings of SPIE **6853,** L8541-L8541, Photonics West conference (intern.), San Hose, USA (poster presentation 2008).

4) X. Tsampoula, K. Taguchi, T. Cizmar, P. Prentice, P. Campbell, F. Gunn-Moore, K. Dholakia, ***"Femtosecond cellular transfection using novel laser beam geometries"***, Biomedical Optics meeting (BIOMED, intern.), Florida, USA, (poster presentation 2008).

5) X. Tsampoula, K. Taguchi, T. Cizmar, P. Prentice, N. Ma, P. Campbell, C.T.A. Brown, F. Gunn-Moore, K. Dholakia, ***"Optical transfection of cells using novel laser beam geometries",*** Photon '08 Optics and Photonics conference (intern.), Edinburgh, UK (oral presentation 2008).

6) X. Tsampoula, K. Taguchi, T. Cizmar, P. Prentice, N. Ma, P. Campbell, F. Gunn-Moore, K. Dholakia, ***"Optical transfection of cells using novel laser beam geometries"***, ALT '08 Advanced Laser Technologies conference, Lake Balaton, Hungary
(Invited oral presentation 2008).

7) C.T.A. Brown, X. Tsampoula, D. J. Stevenson, C. McDougall, F. Gunn-Moore, Dholakia K, ***"Enhanced optical micromanipulation and transfection of cells using femtosecond lasers"***, In Digest of the IEEE/LEOS summer topical meetings, 75-76, Acapulco, Mexico.

8) T. Cizmar, V. Kollarova, X. Tsampoula, F. Gunn-Moore, Z. Bouchal, K. Dholakia, ***"Generation and control of multiple Bessel beams for optical micromanipulation",*** Proceedings of SPIE **7038,** Q380-Q380, San Diego, USA.

Distinctions

Arthur Maitland Prize

Awarded by the University of St Andrews to the postgraduate student in Physics who has made the most outstanding, original contribution to research in that academic discipline (2007).

Prize for Best Poster Presentation

Biomedical Optics meeting (BIOMED intern.), Florida, USA, 2008.

Publicity

The importance of using a Bessel beam as well as fibre optics for cellular photoporation has gained significant publicity:

1) ***"Optical syringe aids studies of single cells"*** article in the European magazine for photonics professionals, Optics and Laser Europe **171,** 2009.

2) ***"The "light saber" that could help fight cancer. Punch holes where we want them"*** article in Daily Mail newspaper.

3) BBC Radio 4 interview as part of the "Discovery: Light fantastic" program, where I talked about our work on cellular photoporation.